Imaging with Second-Harmonic Generation Nanoparticles

Thesis by

Chia-Lung Hsieh

In Partial Fulfillment of the Requirements

for the Degree of

Doctor of Philosophy

California Institute of Technology

Pasadena, California

2011

(Defended March 16, 2011)

Publications contained within this thesis:

1. C. L. Hsieh, R. Grange, Y. Pu, and D. Psaltis, "Three-dimensional harmonic holographic microcopy using nanoparticles as probes for cell imaging," Opt. Express **17**, 2880–2891 (2009).
2. C. L. Hsieh, R. Grange, Y. Pu, and D. Psaltis, "Bioconjugation of barium titanate nanocrystals with immunoglobulin G antibody for second harmonic radiation imaging probes," Biomaterials **31**, 2272–2277 (2010).
3. C. L. Hsieh, Y. Pu, R. Grange, and D. Psaltis, "Second harmonic generation from nanocrystals under linearly and circularly polarized excitations," Opt. Express **18**, 11917–11932 (2010).
4. C. L. Hsieh, Y. Pu, R. Grange, and D. Psaltis, "Digital phase conjugation of second harmonic radiation emitted by nanoparticles in turbid media," Opt. Express **18**, 12283–12290 (2010).
5. C. L. Hsieh, Y. Pu, R. Grange, G. Laporte, and D. Psaltis, "Imaging through turbid layers by scanning the phase conjugated second harmonic radiation from a nanoparticle," Opt. Express **18**, 20723–20731 (2010).

Acknowledgements

During my five-year Ph.D. studies, I have thought a lot about science and life, but I have never thought of the moment of writing the acknowledgements of my thesis. At this moment, after finishing writing six chapters of my thesis, I realize the acknowledgment is probably one of the most difficult parts for me to complete. I have got support and help from so many people, and it is hard to put all my gratitude into words. This thesis cannot be accomplished without them.

I would like to thank my advisor Professor Demetri Psaltis, who gave me the opportunity to experience this challenging and rewarding journey. He has taught and guided me during my studies with enormous trust and encouragements. He offered me the chance of being on detached duty for four years working with him at EPFL in the beautiful city of Lausanne in Switzerland, which makes my Ph.D. life extraordinary. In these years, his vision and creativity have been the crucial input of my accomplishments.

In my Ph.D. studies, I have been dedicated to the “SHRIMP” project in which I worked closely with my colleagues and also collaborators Ye Pu and Rachel Grange. Working in the “SHRIMP team” is a unique and wonderful experience. The close cooperation within the team makes my research life delightful. Ye is an expert both in optics and chemistry who always comes up with the ideas and suggestions. His rich experience has helped me do the right thing in the right way. Rachel is a great person to work with in the lab. She is a careful and patient experimentalist who is also full of energy and passion. She has helped me save great amount of time in the experiment. I would also like to thank the two young members of the SHRIMP team, Thomas Lanvin and Xin Yang, who have brought the fresh inputs of the project. Pursuing the

SHRIMP project has been bumpy and challenging, and I cannot accomplish this far without them.

I have been greatly benefited from the discussion and collaboration with scientists and professionals in nanotechnology and biology when pursuing the SHRIMP project. For their help and supports, I would like to thank Paul Bowen in Powder Technology Lab at EPFL for kindly providing high-quality nanocrystals; Marc Chambon, Nathalie Ballanfat and Sylviane Reymond in Biomolecular Screening Facility at EPFL for preparing biological cells; Arne Seitz, Thierry Laroche and Artacho José in Bioimaging and Optics Platform at EPFL for helping setup the confocal microscope; Keith Harshman, Johann Weber, Floriane Consales, Marie-Agnes Doucey, John Wang and Pei-Jiun Chen in Protein and DNA Array Facility at University of Lausanne for the advices and support of antibody conjugation, Ulrike Haessler, Miriella Pasquier, Witold Kilarski, Melody Swartz in Lymphatic and Cancer Bioengineering Lab at EPFL for live animal experiments.

I would also like to thank my colleagues, Andreas Vasdekis, Jae-Woo Choi, Alexandre Goy, Wuzhou Song, Julien Cuennet, Ioannis Papadopoulos, Grégoire Laporte, and Jianhang Yang, who have provided me a friendly and supportive working environment. Especial thanks to Carole Berthet and Lucinda Acosta for the administrative support.

Finally, I want to thank my dear family, and also my dearest girlfriend, Ping-Hui Lin, for their endless love and support, which has reminded me that I am never alone in my Ph.D. journey.

Abstract

Second-harmonic generation (SHG) nanoparticles show promise as imaging probes due to their coherent and stable signals with a broad flexibility in the choice of excitation wavelength. In this thesis, barium titanate ($BaTiO_3$) nanoparticles are developed as “Second Harmonic Radiation IMaging Probes (SHRIMPs).” The thesis presents the fundamental study on the SHG from the nanoparticles, biochemical functionalization of the nanoparticles, and also novel imaging systems using the SHG nanoparticles as imaging probes, including scan-free 3D imaging and imaging through scattering medium.

We study the absolute SHG efficiency of single $BaTiO_3$ nanoparticles both theoretically and experimentally. The polarization-dependent SHG responses of individual nanoparticles are studied in detail. From the measured polar response of a nanoparticle, we are able to find the orientation of the nanoparticle. We also examine the SHG response of the nanoparticles under different excitation polarizations, including linearly and circularly polarized excitations.

Motivated by the stable SHG signal of the nanoparticle with high contrast in biological cellular environment, we develop $BaTiO_3$ nanoparticles as long-term cell imaging probes. The $BaTiO_3$ nanoparticles are surface functionalized with primary amine groups for stable colloidal dispersion and also for further bio-molecule conjugation. We observe no toxicity of the functionalized nanoparticles to biological cells. To achieve specific labeling of proteins of interest, we couple antibodies covalently onto the nanoparticles. Specific labeling of cell membrane proteins with SHG nanoparticles for SHG live cell imaging is achieved.

The coherent SHG signal radiated from the nanoparticles offers opportunities for new imaging techniques. Using interferometric detection, namely harmonic holography (H^2), both amplitude and phase of the SHG field at a two-dimensional (2D) digital camera can be captured. Through digital beam propagation, three-dimensional (3D) SHG field distribution, reflecting 3D distribution of nanoparticles, can be reconstructed. Therefore, a 3D imaging of nanoparticles can be achieved without scanning. We demonstrate the scan-free 3D imaging of nanoparticles in biological cells by the H^2 microscope with sub-micron spatial resolution.

Moreover, we exploit the coherent SHG signal for imaging through scattering media by performing optical phase conjugation (OPC) of the SHG signal. We demonstrate an all-digital OPC of the SHG signal originated from a nanoparticle by combining H^2 and dynamic computer-generated holography using a spatial light modulator. The phase-conjugated SHG scattered field retraces the scattering trajectory and allows us to create a clean focus on the nanoparticle placed inside a scattering medium. The nanoparticle acts as a beacon of light; it helps us find the tailored wavefront for concentrating light at the nanoparticle inside the scattering medium. When the scattering medium is thin, imaging through scattering media can be achieved by raster-scanning the phase-conjugated focus in the vicinity of the nanoparticle without losing the locality of the focus. We build a phase conjugate scanning microscope to demonstrate imaging through a thin diffusive screen by using SHG beacon nanoparticles, in which a clear image of a target placed behind a ground glass diffuser is obtained.

Table of contents

Acknowledgements **iv**

Abstract **vi**

Table of contents **viii**

List of figures **x**

Chapter 1 Introduction.....1

1.1 Second-harmonic generation (SHG) imaging.....3

1.2 SHG scattering from nanoparticles 6

1.3 Outline of the thesis.....8

Chapter 2 Material and optical characterization of SHG nanoparticles 11

2.1 Barium titanate ($BaTiO_3$) nanoparticles 11

2.2 Optical characterization of SHG signal from individual $BaTiO_3$ nanoparticles 14

2.3 Polarization-dependent SHG response from $BaTiO_3$ nanoparticles 20

2.3.1 Theory for plane-wave excitation.....20

2.3.2 Theory for tightly focused excitation.....25

2.3.3 Measurements of SHG polar response of the nanoparticles 30

2.4 Linearly and circularly polarized excitations.....36

Chapter 3 Cellular imaging with SHG nanoparticles 46

3.1 Cytocompatibility of $BaTiO_3$ nanoparticles.....46

3.2 Nonspecific cell labeling by endocytosis 49

3.3 Surface functionalization and antibody conjugation of the nanoparticles .52

3.3.1 Materials 52

3.3.2 Protocol of antibody conjugation 53

3.4 Specific labeling in an antibody microarray 56

3.5 Specific cell membrane protein labeling via immunostaining 60

Chapter 4 3D imaging of SHG nanoparticles 63

4.1 SHG 3D scanning microscopy 63

4.1.1 *In vitro* cell imaging 64

4.1.2 *In vivo* mouse imaging 66

4.2 Scan-free 3D holographic microscopy 69

4.3 Off-axis and on-axis digital holography 72

4.4 Harmonic holographic (H^2) microscopy 76

4.4.1 Experimental setup 76

4.4.2 Point spread function of the H^2 microscope 78

4.4.3 Scan-free 3D imaging of SHG nanoparticles 80

Chapter 5 Imaging through scattering media by digital phase conjugation 85

5.1 Overview of imaging through scattering media 85

5.2 Concentrating light on nanoparticles behind scattering layers 90

5.2.1 Sample preparation and experimental setup 91

5.2.2 Results and discussion 95

5.3 Imaging through scattering layers by using SHG beacon nanoparticles 100

5.3.1 Concepts 100

5.3.2 Experimental details 102

5.3.3 Results and discussion 106

Chapter 6 Conclusions and future extensions 114

Bibliography 119

List of figures

Fig. 1-1 Schematic diagram of SHG (scattering) from a spherical nanoparticle 7
Fig. 2-1 Bright-field TEM image of $BaTiO_3$ nanoparticles 12
Fig. 2-2 SEM image of $BaTiO_3$ nanoparticles 12
Fig. 2-3 (a) Zeta potential of $BaTiO_3$ nanoparticles colloidal suspension as a function of the pH of the solution. (b) Size distribution of the $BaTiO_3$ nanoparticles colloidal suspension measured by dynamic light scattering 13
Fig. 2-4 Schematic diagram of the SHG wide-field microscope for SHG signal characterization. λ/2: half-wave plate, L1: 5 cm lens, OBJ: microscope objective, L2: 20 cm lens. The red beam shows the excitation at 800 nm, while the blue illustrate the SHG signal radiated from the nanoparticles under excitation. 15
Fig. 2-5 (a) SEM image of $BaTiO_3$ nanoparticles. (b) Wide-field SHG microscopic image of the corresponding $BaTiO_3$ nanoparticles. One-to-one correspondence can be seen between (a) and (b). The scale bars are 500 nm. 16
Fig. 2-6 Power dependence of the SHG signal from $BaTiO_3$ nanoparticles in double logarithmic scale. The squares are measured results and the solid line is the linear fit with the slope of 2.2. The inset shows the SHG optical spectrum centered at 400.6 nm with a full-width half-maximum of 5 nm. 16
Fig. 2-7 Long-term imaging with SHG nanoparticles. (a) Wide-field SHG image of an isolated $BaTiO_3$ nanoparticle. The size of the image is 15×15 μm^2. (b) The time-lapse SHG signal of the nanoparticle under 5 hour continuous excitation. The dots represent experimental measurements and the line shows the average of the signal. The signal intensity remains unchanged after the emission of $> 10^9$ photons. 18
Fig. 2-8 Schematic diagram of a $BaTiO_3$ nanoparticle oriented at an arbitrary direction under a LP plane-wave excitation. The SHG signal is collected by a microscope objective. 21

Fig. 2-9 Theoretical calculation of polarization-dependent SHG response of a $BaTiO_3$ nanoparticle under a plane-wave excitation. (a) The polarization dependency of the total SHG response of a $BaTiO_3$ nanoparticle. (b)(c) The polarization dependency of the SHG response of a $BaTiO_3$ nanoparticle where the SHG signal is collected by a (b) NA 1.2 water-immersion objective and (c) NA 0.3 water-immersion objective 23

Fig. 2-10 Schematic diagram of a tightly focused excitation by using a microscopic objective.....26

Fig. 2-11 Theoretical calculation of the tightly focused LP (X-polarized) excitation. The magnitude (a)–(c) and the phase (d)–(f) of the electric field of X-, Y-, Z-polarizations at the focused beam waist (Z = 0). The incidence is an X-polarized plane-wave of 812 nm wavelength which is focused by a NA 1.2 water-immersion objective in an index-matching environment. The size of the images are $6 \times 6\ \mu m^2$.....27

Fig. 2-12 Theoretical calculation of the polarization-dependent SHG response of a $BaTiO_3$ nanoparticle in a scanning image with a tightly focused excitation (NA 1.2 water-immersion objective). (a) The polarization dependency of the total SHG response of a $BaTiO_3$ nanoparticle. (b) (c) The polarization dependency of the SHG response of a $BaTiO_3$ nanoparticle where the SHG signal is collected by a (b) NA 1.2 water-immersion objective and (c) NA 0.3 water-immersion objective 29

Fig. 2-13 SEM image of isolated $BaTiO_3$ nanoparticles randomly deposited on an ITO coated glass substrate for SHG polarization measurement.....30

Fig. 2-14 Scanning confocal SHG image of $BaTiO_3$ nanoparticles on an ITO coated glass substrate. The size of the image is $30 \times 30\ \mu m^2$.....31

Fig. 2-15 Scanning confocal SHG images of $BaTiO_3$ nanoparticles under different LP excitation orientations. From (a)–(d), the excitation polarizations were 20, 40, 60, and 80 degrees, respectively, as indicated in the individual figures. The size of the images is $3 \times 3\ \mu m^2$.....32

Fig. 2-16 Theoretical calculations of the polarization-dependent SHG response of $BaTiO_3$ nanoparticle at various orientation angles of θ_0, measured by a

scanning confocal microscope. The orientation of the nanoparticle in the calculation is at ϕ_0 = 0 degrees. 33

Fig. 2-17 (a)–(c) Polarization-dependent SHG response of three representative $BaTiO_3$ nanoparticles measured by a scanning confocal microscope. The experimental data are shown as black dots and the theoretical fits are shown as red curves. The three nanoparticles were found oriented at (θ_0 = 70 ± 5 degrees, ϕ_0 = 35 ± 5 degrees), (θ_0 = 50 ± 5 degrees, ϕ_0 = 115 ± 5 degrees), and (θ_0 = 10 ± 5 degrees, ϕ_0 = 50 ± 5 degrees), respectively. The 10 degree resolution of the fitting is due to the accuracy of the measurement. 35

Fig. 2-18 Theoretical calculation of the normalized SHG response of a $BaTiO_3$ nanoparticle as a function of nanoparticle orientation under a CP plane-wave excitation. Different detection schemes are considered: total SHG response (black solid curve), collected by an NA 1.2 water-immersion objective (red dash curve), and collected by an NA 0.3 water-immersion objective (blue dash-dot curve).....37

Fig. 2-19 Theoretical calculation of the normalized SHG response of a $BaTiO_3$ nanoparticle as a function of nanoparticle orientation under a rotating LP plane-wave excitation. Different detection schemes are considered: total SHG response (black solid curve), collected by an NA 1.2 water-immersion objective (red dash curve), and collected by an NA 0.3 water-immersion objective (blue dash-dot curve).....39

Fig. 2-20 Theoretical calculation of the normalized SHG response of a $BaTiO_3$ nanoparticle as a function of nanoparticle orientation under a CP tightly focused excitation. Different detection schemes are considered: total SHG response (black solid curve), collected by an NA 1.2 water-immersion objective (red dash curve), and collected by an NA 0.3 water-immersion objective (blue dash-dot curve).....40

Fig. 2-21 Theoretical calculation of the normalized SHG response of a $BaTiO_3$ nanoparticle as a function of nanoparticle orientation under a tightly focused rotating LP excitation. Different detection schemes are considered: total SHG response (black solid curve), collected by an NA

1.2 water-immersion objective (red dash curve), and collected by an NA 0.3 water-immersion objective (blue dash-dot curve). 41

Fig. 2-22 Relative SHG response of 39 $BaTiO_3$ nanoparticles under tightly focused CP and rotating LP excitations correlated to the nanoparticle orientations. The red solid curve is the theoretical calculation considering a tightly focused excitation, while the blue dots are the experimental results.....44

Fig. 2-23 Evaluation of the ellipticity effect in the excitation polarization on the relative SHG response of $BaTiO_3$ nanoparticles under CP and LP tightly focused excitations correlated to the nanoparticle orientations. The black/red curve is the theoretical calculation considering with/without ellipticity in the excitation introduced by the system, while the blue dots are the experimental results.....45

Fig. 3-1 Surface functionalization of $BaTiO_3$ nanoparticles with amino-silanes for stable water-soluble colloidal suspension.....48

Fig. 3-2 Cell viability measurement after incubating the HeLa cells with different concentrations of the $BaTiO_3$ nanoparticles for 24 hours. The results have been normalized to the control experiment. 49

Fig. 3-3 Scanning confocal section images of the $BaTiO_3$ nanoparticles inside the myeloid cells via endocytosis. (a) Transmission channel. (b) SHG channel. (c) Merge image of (a) and (b). The size of the images is 130 $\times$ 130 μm^2.....51

Fig. 3-4 Scheme of covalent bioconjugation of IgG antibody onto the surface of $BaTiO_3$ nanoparticle for specific labeling imaging application 55

Fig. 3-5 The fluorescent microscopic image of the primary-antibody microarray labeled by the secondary antibody-Cy5 57

Fig. 3-6 SHG microscopic image of the primary-antibody microarray labeled by the 2nd-Ab-SHRIMPs. The dashed circles show the locations where the target primary antibody, two other primary antibodies for negative control, and the buffer solution were printed. Each of the samples was printed four times in a row in the field of view of this figure. The printing spot size is 90 μm in diameter and the period between the adjacent spots is 200 μm. A high concentration of SHRIMPs can be

observed at the locations of the target primary antibodies, showing a highly specific labeling of the 2nd-Ab-SHRIMPs. 59

Fig. 3-7 Quantitative analysis of Fig. 3-6. The ratio of the number of SHRIMPs presenting at the four samples was 1: 0.03: 0.03: 0.05 (Mouse IgG: Goat IgG: Rabbit IgG: Buffer Solution), measured from the integrated SHG intensity. The error bar shows the standard deviation of the four spots of each sample. 59

Fig. 3-8 Confocal section images of HeLa cells labeled with the 2nd-Ab-SHRIMPs. (a)–(d) The cells were first labeled with the primary antibody specific to the HLA class I molecules present on the cell membrane and then labeled with the 2nd-Ab-SHRIMPs; (e)–(h) The control sample where the cells were not labeled with primary antibody but under otherwise identical conditions; SHG images are shown in green in (a) and (e); two-photon fluorescence images are shown in red in (b) and (f); transmission images are shown in (c) and (g); and the merged images of SHG images and fluorescence images are shown in (d) and (h). The size of the images is 105×105 μm^2. 62

Fig. 4-1 Confocal section series of a calcein-stained HeLa cell (in red) with SHG nanoparticles (in green) inside it at successive depths (indicated below the images), from the top to the bottom of the cell. The size of the images is 30×30 μm^2. 65

Fig. 4-2 Confocal section images of a calcein-stained HeLa cell (in red) with SHG nanoparticles (in green) inside it. 3D localization of the nanoparticles inside the cell is clearly observed. The scale bar is 5 μm. 66

Fig. 4-3 *In vivo* SHG imaging of the nanoparticles in a living mouse tail. (a) The photograph of the experimental scenario. (b) The SHG section image (XY plane) at 100 μm deep in the mouse tail where two isolated nanoparticles can be seen. (c) The SHG cross-section image (XZ plane) of the sample along the dashed line in (b), in which both the endogenous SHG from the muscles on the surface of the tail and also the two nanoparticles inside the tail are clearly observed 68

Fig. 4-4 Off-axis holographic imaging system 72

Fig. 4-5 On-axis holographic imaging system 75

Fig. 4-6 H^2 microscope experimental setup. BS1 and BS2, beam splitters; M, mirror; L1 and L2, lens; S, sample; OBJ, microscope objective; BE, beam expander; F, band-pass filter centered at 400 nm. BS1 splits the laser into signal and reference beams. In the signal arm, L1 slightly focuses the excitation beam into the sample with nanoparticles. OBJ and L2 form a 4F imaging system to collect and optically magnify the SHG image. The EMCCD is placed away from the 4F imaging plane. Bandpass filters are placed in front of the EMCCD to remove the excitation from the SHG signal. The reference beam goes through a motorized delay stage and a BBO crystal so that the coherent reference SHG laser pulses are generated and can be temporally and spatially overlapped with the signal on the EMCCD. The signal and reference beams are combined collinearly by BS2 and therefore an on-axis digital hologram is recorded on the EMCCD. 77

Fig. 4-7 Section and cross-section SHG images of two isolated $BaTiO_3$ nanoparticles, reconstructed from a single on-axis digital hologram. Sub-micron 3D localization of the SHG nanoparticle is achieved. The bar in the image is 1 μm. 78

Fig. 4-8 Optical successive section images of an isolated $BaTiO_3$ nanoparticle at different depths (indicated in the figures), reconstructed from a single on-axis digital hologram. The size of the images is 1.5×1.5 μm^2. 79

Fig. 4-9 Images of SHG nanoparticles embedded in PDMS. (a)–(d): SHG images of the nanoparticles on four different planes, focusing by moving the optics with a conventional microscope. (e)–(h): Holographic reconstructed images of the corresponding nanoparticles, focusing by digital reconstruction. The relative depths of these four planes are 0, 9.4, 17.2, and 20.3 μm, respectively. Scale bars are 2 μm. 81

Fig. 4-10 Images of nanoparticles non-specifically labeling HeLa cells. (a) Superposition of the bright field transmission image of a HeLa cell (in red) and the SHG image of nanoparticles (in green) taken by a conventional microscope. Six groups of nanoparticles assigned with numbers were under analysis. Some of them cannot be seen clearly because they are out of focus. (b)–(d) H^2 reconstructed images at three

different planes with relative depths of 0 μm, 3.12 μm, and 6.24 μm, respectively. The white arrows show the nanoparticles that are in focus, while the gray arrows show the nanoparticles that are out of focus. The group labeled with number 4 is a big cluster so that it is bright both in (b) and (c). (e) Normalized intensity line profiles of the six nanoparticles when they are on focus through digital reconstruction. The scale bars are 5 μm. 84

Fig. 5-1 Schematic diagram of projecting an image through a scattering medium by wavefront optimization 87

Fig. 5-2 Schematic diagram of projecting an image through a scattering medium by phase conjugation 89

Fig. 5-3 The schematic diagram of the sample structure 92

Fig. 5-4 Digital phase conjugation experimental setup. λ/2, half wave plate; PBS, polarization beam splitter; M, mirror; DI, dichroic mirror; L1–L4, lens; OBJ1 and OBJ2, microscope objectives; S, sample; BS1–BS3, non-polarizing beam splitters; BF, band-pass filter centered at 400 nm. The laser power for excitation and phase conjugation can be controlled by the λ/2 and the PBS. A translation stage was used to overlap the signal and the reference pulses temporally for the H^2 microscopy. Band-pass filters are placed in front of the CCD cameras to remove the excitation from the SHG signal. 94

Fig. 5-5 Digital phase conjugation through a clear medium. (a) The epi-SHG image of the nanoparticle under excitation. (b) The conjugated phase pattern of the recorded SHG field emitted from the nanoparticle, showing a Fresnel zone plate. (c) The phase-conjugated focus formed at the sample by using the Fresnel zone plate shown in (b). The FWHM of the bright spots in (a) and (c) is 1.95 μm. The scale bars in the figures are 5 μm. 96

Fig. 5-6 Digital phase conjugation through a turbid medium. (a) The conjugated phase pattern of the scattered SHG field. (b) The normalized intensity image of the phase-conjugated focus through a turbid medium by using the phase pattern shown in (a). The FWHM of the spot is 2.3 μm. (c) The normalized intensity image of the distorted focus without phase

conjugation. No focus is observed. Note that (b) and (c) are measured with the same power of the phase-conjugated beams and they are normalized by the same factor in the image processing. The scale bars in the figures are 5 μm. 97

Fig. 5-7 Comparison of the measured diffraction limited focus and the phase-conjugated focus. Black: the normalized intensity profile of the diffraction limited focus; red: the normalized intensity profile of the phase-conjugated focus. The FWHMs of the diffraction limited focus and the phase-conjugated focus are 1.95 μm and 2.3 μm, respectively. 97

Fig. 5-8 Two steps of imaging through turbid media in a phase conjugate scanning microscopy. (a) Recording the scattered SHG field radiated from a nanoparticle by digital holography. (b) Scanning the phase-conjugated focus on the imaging plane by illuminating the same region of the turbid medium (shown as the red circular region) with the phase-conjugated beam at different angles 101

Fig. 5-9 (a) The experimental setup of the harmonic holographic microscopy for recording the complex scattered SHG field. Inset: The illustrative diagram of the sample structure. (b) The experimental setup of the phase conjugate scanning microscope. Note that (a) and (b) show the same setup with different light illuminations for different steps of the experiment. The light not in use is blocked in the experiment and is not shown in the figures. DI, dichroic mirror; L1–L4, lens; OBJ1 and OBJ2, microscope objectives; S, sample; BS1–BS3, non-polarizing beam splitters; BF, band-pass filter centered at 400 nm; M, mirror 103

Fig. 5-10 Illustration of the tilt of the phase-conjugated beam as the SLM tilts. (a) The optical diagram of the SLM projection through the 4F imaging system consisting of L2 and OBJ2. Note that the SLM is not placed at the imaging plane of the 4F system, and therefore the SLM image is between the focal plane and OBJ2. Here f1 and f2 are the focal length of the OBJ2 and L2; d is the distance between the focal plane and the SLM image plane. (b) The illustrative diagram showing how the phase-conjugated beam tilts while the SLM tilts. Details of the coordination

between the tilt and the shift of the SLM for the scanning are in the main text. 105

Fig. 5-11 Focusing through the turbid medium without and with phase conjugation. (a) The speckle pattern on the image plane when focusing directly through the turbid medium by the objective without phase conjugation. (b) The conjugated phase pattern projected on the SLM for phase conjugation. The grayscale from black to white represents the phase modulation from 0 to 2π. (c) The phase-conjugated focus on the image plane. The inset shows the magnified image of the focus. The scale bar in the inset is 5 μm. The size of the images in (a) and (c) is 195 ×195 μm^2.....107

Fig. 5-12 Angular response of the tilted phase-conjugated focus. Note that the tilt angle in this figure is the tilt angle at the sample position. The experimental data is shown as black dots and the fitting based on the theory of optical memory effect is shown as the red line.....108

Fig. 5-13 (a) The wide-field transmission image of the target. The target is a 130 nm thick gold pattern on a glass substrate prepared by photolithography. The bright region in this figure indicates the transparent area while the dark region indicates the gold film. (b) The corresponding phase conjugate scanning image of the target. The target is clearly resolved. The intensity profile along the dashed line is plotted in Fig. 5-14. (c) The scanning image of the same target without phase conjugation. Since the focus is severely distorted by the turbid medium, the image is completely blurry. The size of the images are 140 × 140 μm^2. 111

Fig. 5-14 The normalized intensity profile along the dashed line in the phase conjugate scanning image shown in Fig. 5-13. (b) The experimental data points are shown as blue dots. 112

Chapter 1 Introduction

Light has been an important tool in studying science. Through light-matter interactions, such as scattering, reflection, refraction, absorption, and photoemission, the propagating light field carries the information of the object under study, which allows us to observe it at a distance. Light introduces minimal perturbation during the observation and it readily propagates in free space. Therefore, light is extremely useful and convenient for sensitive detections. Technological advances in light sources, optical filters, computer hardware, and photon-counting detectors have been extensively employed in optical imaging systems. Extremely sensitive imaging systems have been demonstrated [1–5], which allows us to quantitatively analyze the chemical reactions on the single-molecule level [1, 2].

Every imaging system needs a contrast mechanism. One of the most efficient methods of creating a contrast in an imaging system is to change the color of the signal away from the color of illumination. By using optical filters, one can efficiently reject the illuminating wavelength and allow only signal wavelength to arrive at the detector. Photoluminescence is the most widely used mechanism for wavelength conversion in imaging. In particular, fluorescent imaging probes are especially popular in the study of biology due to their satisfactory brightness, biocompatibility, and small physical size [1–7]. Fluorescent proteins can be encoded into genes and introduced into living cells, and the cells will produce these fluorescent proteins when expressing the gene, which is convenient in biological studies [1, 5, 8]. Besides fluorescent proteins, organic dyes [3] and quantum dots [6, 7] are also popular fluorescent probes. The excitation can be done by absorbing the energy from two

photons simultaneously, resulting in the two-photon fluorescence [7, 9, 10]. Besides fluorescence, phosphorescence and upconversion have also been demonstrated as wavelength conversion mechanism for imaging [11–14].

Photobleaching may be the major problem of fluorescent probes [15, 16]. Photobleaching is an irreversible photochemical degradation of a fluorescent probe, leading to the permanent loss of the fluorescent signal. This is especially problematic in long-term time-lapse measurement. Besides photobleaching, fluorescent intermittency or “blinking” is another potential problem of fluorescent probes, which is due to the stochastic switching between bright and dark states of the probe [17, 18]. Many efforts have been made to develop more robust and more stable fluorescent probes. Semiconductor quantum dots have been shown to be much more resistant to photobleaching and also less prone to blinking [19, 20]. Fluorescent diamond nanocrystals with nitrogen-vacancy defects also show a stable signal resistant to photobleaching [21, 22].

The challenges of imaging with photoluminescent signal can be solved by nonlinear optical (NLO) processes which are also known for wavelength conversion. In NLO processes, the light-induced polarization of the material responds nonlinearly to the electric field of the excitation light, leading to radiations at harmonic optical frequencies [23]. Since the NLO processes do not involve any real-state transition, so the problems of photobleaching and blinking are circumvented [23]. Among all the NLO processes, second-order nonlinearity, such as second-harmonic generation (SHG), is particularly interesting because it is only efficient in noncentrosymmetric environments [23]. Therefore, SHG provide high contrast in unstructured and isotropic environments.

1.1 Second-harmonic generation (SHG) imaging

SHG microscopy has been developed as a standard nonlinear microscopy since the 1970s [24, 25]. The excitation wavelength is usually in NIR and the SHG signal is at exactly half the excitation wavelength, which is in the visible spectrum. Such a SHG scanning microscope is compatible with two-photon fluorescence scanning microscopy [26, 27]. The quadratic dependency of the signal to the excitation power provides the optical sectioning capability in the axial direction, which is appealing to three-dimensional (3D) scanning imaging [28, 29]. The multi-photon microscopy is also ideal for deep tissue imaging because the scattering of the sample is less severe at longer excitation wavelengths [28, 29]. SHG scanning microscopy has been used for examining endogenous structures in label-free biological samples [26, 30–32]. Ordered and highly polarizable biological structures, such as collagen [32], muscle [33], and microtubules [30] are efficient in SHG, and therefore they show high contrast in a mostly isotropic environment in SHG images. In biological samples, the molecular structures and orientations determine the nonlinear susceptibility. As a result, the polarization-dependent measurement of the SHG signal can be used to study the molecular structures of biological samples [32–35].

While the endogenous SHG signal is attractive for label-free non-invasive imaging, exogenous SHG markers are also desirable due to the flexibility of having the SHG contrast from any target of interest. The development of SHG contrast agents began from organic dipolar molecular systems where the optical nonlinearity arises from the intramolecular charge transfer [36–38], referring to the SHG dyes. These SHG dyes have been demonstrated effective for biological membrane SHG imaging. The asymmetric styryl dyes label only the outer leaflet of the lipid bilayer of

the biological membrane, which satisfies the non-inversion symmetry requirement for an efficient SHG process [39]. Interestingly, the SHG signal intensity of the dye molecule is sensitive to the local electric potential [31, 40], and it has been shown as a novel approach for high-resolution detection for dynamic electrical activity of neurons [41].

In addition to SHG-active molecules, SHG studies of nanomaterials have become a very active field very recently. Thanks to the advancement in nanotechnology and molecular chemistry, SHG has been observed from various types of nanomaterials, including metals [42–45], semiconductors [46–51], dielectric [52–57], and organic nanomaterials [58–60]. Since SHG only takes place in a non-centrosymmetric environment under electric dipole approximation [23], nanomaterials of non-centrosymmetric crystal structures are efficient in SHG. Nanomaterials of non-centrosymmetric crystal structures include $BaTiO_3$ [56, 61–63], ZnO [48–51], $KTiOPO_4$ (KTP) [52, 54, 64], $Fe(IO_3)_3$ [55, 65], $KNbO_3$ [57], etc. The size of these nanomaterials ranges from 10–100 nm. As the SHG conversion efficiency of these nanomaterials is sufficiently high, these SHG nanomaterials have shown promise as alternative imaging probes due to their non-bleaching and non-blinking signal [50, 61, 65, 66].

We refer to these SHG nanomaterials as “Second Harmonic Radiation IMaging Probes (SHRIMPs).” It should be emphasized that, due to their unique optical properties, these SHG nanoprobes offer opportunities that are not available with photoluminescent probes. We list and discuss these properties of SHRIMPs as follows:

1. Stable: SHG does not involve any real-state transition, so the problems of photobleaching and blinking are circumvented [23]. Such stable signal is ideal for dynamic and long-term imaging.
2. Tunable: SHG wavelength is exactly half of the excitation wavelength. Therefore, SHG wavelength tuning can be done by tuning the excitation wavelength [57]. Moreover, SHG at nano-scale is a nonresonant process (without phase-matching requirement), providing a broad flexibility of choosing the best excitation wavelength or the emission SHG wavelength.
3. Coherent: The virtual-state transitions of SHG processes lead to the coherence between the signal and the excitation. As a result, SHG nanoprobes act as subwavelength coherent photon sources [57, 67, 68]. This is a great advantage, allowing us to detect the complex SHG signal of the SHRIMPs by interferometric approaches [61, 64, 69, 70]. For example, the complex field information of the SHG signal offers opportunities for new imaging techniques, such as scan-free 3D imaging [61, 69, 70] and imaging through turbid media by optical phase conjugation [67, 68].
4. Fast: As the excitation lifetime of common fluorescent probes is on the order of nanoseconds [71, 72], SHG response time is only limited by the bond electron response time, which is less than femtoseconds [23]. This means the SHG emission is almost instantaneous to the excitation, allowing for ultrafast modulation and coherent control of the SHG signal.
5. Polarization sensitive: SHG signal from crystalline structure is generally dependent on the excitation polarization [23]. As a result, a polar measurement from the far field gives information about the crystalline orientation at nano-scale,

offering a new degree of freedom for controlling and detecting the SHG signal [32–35, 47, 52, 55, 56].

Motivated by the advantages of SHG imaging probes listed above, many efforts have been made toward developing SHG nanoparticles as bio-imaging probes recently. By exploiting the flexibility in the selection of the excitation wavelength, SHG nanoparticles have also been demonstrated as deep tissue imaging probes [65]. Through surface functionalization and bioconjugation, specific labeling of the nanoparticles has been demonstrated [50, 62]. It has also been shown that SHG nanoparticles can be used for *in vivo* imaging [66].

1.2 SHG scattering from nanoparticles

The effective phenomena of SHG from nanoparticles can be seen as hyper-Rayleigh scattering (HRS). HRS was first studied with molecules where the nonlinear optical signal comes from the optical hyperpolarizability of the molecules [73, 74]. SHG from nanoparticles is therefore very different from SHG in bulk materials where the SHG is usually governed by phase matching condition [23]. The SHG scattering from a spherical nanoparticle is described schematically in Fig. 1-1. The excitation is a plane wave at fundamental frequency ω and the induced SHG fields scatter in all directions. The SHG scattering from nanoparticles can be studied from calculating the linear scattering of the excitation field at fundamental frequency within and around the nanoparticles. The excitation field then induces microscopic SHG sources (dipoles and multipoles) at the locations where the second-order susceptibility is nonzero. The SHG sources of the nanoparticles can be classified into surface and bulk contributions, shown as $\chi^{(2)}{}_{\text{surface}}$ and $\chi^{(2)}{}_{\text{bulk}}$ in Fig. 1-1, and their strengths are dependent on the

materials of the nanoparticle and the surrounding environment. The overall SHG radiation of the nanoparticle is the coherent addition of the SHG fields radiated by each individual microscopic SHG dipole and multipole [75, 76].

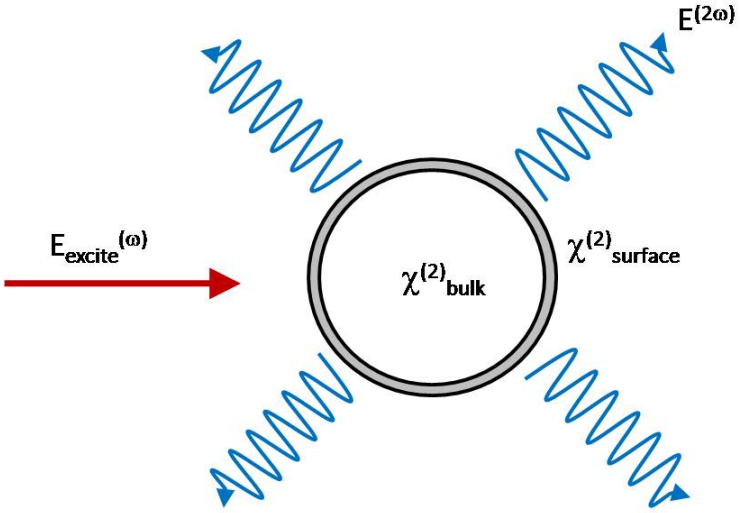

Fig. 1-1 Schematic diagram of SHG (scattering) from a spherical nanoparticle

As was pointed out in the previous section, nanoparticles comprised of non-centrosymmetric and highly polarizable crystal structures are capable of efficient SHG. This is due to the strong second-order susceptibility within the volume of the nanoparticles inducing strong SHG dipole sources within the nanoparticles. Such bulk contribution is referred to as the locally excited electric dipole contribution. For nanoparticles of non-centrosymmetric crystal structure, such bulk nonlinearity usually dominates the SHG response [47, 48, 52, 55, 56, 59–61, 75]. For the application of imaging probes, nanoparticles of strong bulk nonlinearity are certainly desirable as it leads to strong SHG conversion efficiency.

For nanoparticles of centrosymmetric material, the bulk contribution disappears and other SHG sources are responsible for the nonlinearity. Surfaces are known for SHG by producing locally excited SHG dipole moments because the inversion symmetry is broken at the interfaces. Due to this surface specific SHG response, SHG

has been exploited to the study of interfaces properties between two centrosymmetric materials [77–80]. Interestingly, this surface contribution vanishes when the shape of the nanoparticle is centrosymmetric, such as a perfect sphere. This is because the SHG sources at different parts of the surface of a sphere interfere with each other, and the overall SHG radiation vanishes due to the symmetry of the problem. It is worth noting that any deviation in shape from centrosymmetry leads to a nonvanishing SHG response [45, 81].

Following the above discussion, for a nanoparticle of centrosymmetric material and of perfect spherical shape, such as a gold spherical nanoparticle, the SHG sources are from neither the bulk nor the surface under locally excited electric dipole approximation. Therefore, the SHG from such nanoparticles is weak. The SHG response from those nanoparticles can be explained under multipole expansion [42, 43]. The leading-order SHG contributions are a nonlocal excited electric dipole moment and a local excited electric quadrupole moment. The former is treated as surface contribution because it requires a nonlocal excitation mechanism where the phase variation of the excitation across the surface of the nanoparticle is considered. The later is treated as bulk contribution through a local excitation mechanism.

1.3 Outline of the thesis

This thesis presents the development of $BaTiO_3$ nanoparticles as SHG biological imaging probes for novel imaging applications. It includes fundamental studies on SHG from nanoparticles, chemical treatments of nanoparticles for biological applications, and also novel imaging systems taking advantages of the coherent SHG signal of the nanoparticles.

Chapter 2 addresses the fundamental study of SHG in $BaTiO_3$ nanoparticles. It starts with material studies and SHG characterization of $BaTiO_3$ nanoparticles. The polarization-dependent SHG response of $BaTiO_3$ nanoparticles are investigated both experimentally and theoretically. From the SHG polar response of the nanoparticle, we are able to retrieve the crystal orientation of the nanoparticle. The absolute SHG conversion efficiency of the $BaTiO_3$ nanoparticle is also studied on single-nanoparticle level. We also explore the possible excitation geometries and polarizations for superior SHG response from the nanoparticles, including plane wave and tightly focused excitations of linear and circular polarizations.

Chapter 3 presents the biochemical development of $BaTiO_3$ nanoparticles as bio-imaging probes. Cytocompatibility of the nanoparticles is examined with biological cells. Stable aqueous colloidal suspension of nanoparticles is prepared through surface functionalization with amine groups. We also demonstrate a bioconjugation scheme for covalently attaching antibodies onto the nanoparticles. The antibody nanoparticle conjugates are able to label target proteins specifically. We demonstrate specific labeling in a protein microarray and also in cell membrane proteins.

Chapter 4 demonstrates 3D imaging capability of SHG nanoparticles, including the conventional scanning SHG microscope and the novel microscope system named “harmonic holographic microscopy.” *In vitro* 3D cell imaging and *in vivo* 3D animal imaging with SHG nanoparticles is demonstrated with a scanning microscope. Then, the advantages of holography in 3D imaging are discussed. Holographic imaging mechanisms used in our laboratory for 3D imaging are described. We experimentally demonstrate 3D imaging of nanoparticles by on-axis digital holography. Sub-micron spatial resolution in 3D is achieved. 3D distribution of nanoparticles in biological cells is recorded in a single digital hologram without scanning.

Chapter 5 shows the use of SHG nanoparticles as beacons of light for focusing and imaging through turbid media. This work aims to solve the challenges of imaging and light delivery in biological tissue due to scattering. We demonstrate an all-digital optical phase conjugation system. By performing phase conjugation of the SHG field originated from the nanoparticles, we show that light can be delivered through a scattering medium and focus onto the nanoparticles. We also demonstrate imaging through a thin diffusive medium by scanning the phase-conjugated focus in the vicinity of the nanoparticle.

Chapter 6 summarizes the thesis and discusses the future extension of SHG nanoparticles for imaging.

Chapter 2 Material and optical characterization of SHG nanoparticles

It is essential to understand the SHG mechanism in nanoparticles in order to use them as imaging probes. In this chapter, the SHG from $BaTiO_3$ nanoparticles will be discussed in detail. It includes the theoretical calculations and also experimental characterizations. The chapter starts with the material studies on $BaTiO_3$ nanoparticles. Sample preparation and basic optical characterization on SHG signal will then be presented. After that, the polarization-dependent SHG response from nanoparticles under various excitations will be studied. Overall, the scope of this chapter is to understand explicitly the SHG from nanoparticles for using them as imaging probes in microscopy.

2.1 Barium titanate ($BaTiO_3$) nanoparticles

$BaTiO_3$ nanoparticles in dry powder were commercially available from TechPowder (TechPowder S.A. Lausanne, Switzerland) and NanoAmor (Nanostructured & Amorphous Materials, Inc. Houston, TX, USA). X-ray diffraction data from the supplier confirms that the crystal structure is tetragonal, which is non-centrosymmetric, allowing for efficient SHG without any further treatment. A bright-field transmission electron microscope (TEM) image of $BaTiO_3$ nanoparticles is shown in Fig. 2-1, and a scanning electron microscope (SEM) image of the nanoparticles is shown in Fig. 2-2. The nanoparticles are nearly spherical in shape and between 60 nm and 110 nm in diameter.

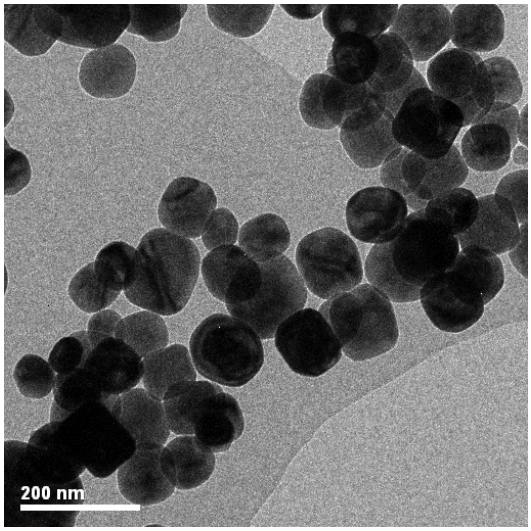

Fig. 2-1 Bright-field TEM image of $BaTiO_3$ nanoparticles

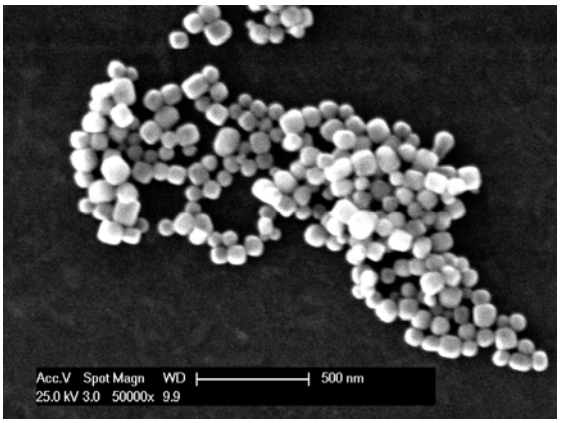

Fig. 2-2 SEM image of $BaTiO_3$ nanoparticles

For the use of nanoparticles in imaging applications, stable colloidal suspension of the nanoparticles is often preferred in order to avoid cluster aggregation. To stabilize the $BaTiO_3$ nanoparticles in colloidal suspension, we dispersed the dry powder in 1.25 mM aminomethylphosphonic acid with the particle concentration of 10^{10} particles/mL. We treated the colloidal suspension with ultrasound (Branson digital sonifier 450) for 10 minutes to break the clusters into individual particles. The suspension was then stirred for 24 hours. The phosphonic acid was adsorbed on the particle surface and results in an amine group coated particle surface [82]. The suspension was stabilized

by electrostatic force from the ionization of the amine group in solution. Finally, we filtered out the big clusters from the suspension by flowing it through a membrane with pore size of 0.22 μm (Millipore Express PLUS). The surface charge of the stabilized particle was determined by the degree of ionization of the amine groups on the particle, which can be tuned by changing the pH of the solution. The zeta potential (i.e., the electrokinetic potential difference between the dispersion medium and the stationary layer of fluid attached to the dispersed nanoparticle) of the monodispersed colloidal suspension was obtained by light scattering measurement (Brookhaven Instruments Corp. ZetaPALS). We observed that the zeta potential decreases from 10 mV to -40 mV when the pH of the solution increases from 2 to 9, as shown in Fig. 2-3 (a). The pH tuning was done by adding HNO_3 and KOH. We also measured the nanoparticle size distribution in suspension by dynamic light scattering (Brookhaven Instruments Corp. 90Plus) showing that most of the particles were well dispersed, while less than 10% of the particles were clusters of double the size (Fig. 2-3 (b)). With the stable colloidal suspension, it was now possible to prepare samples of individual nanoparticles for optical characterization.

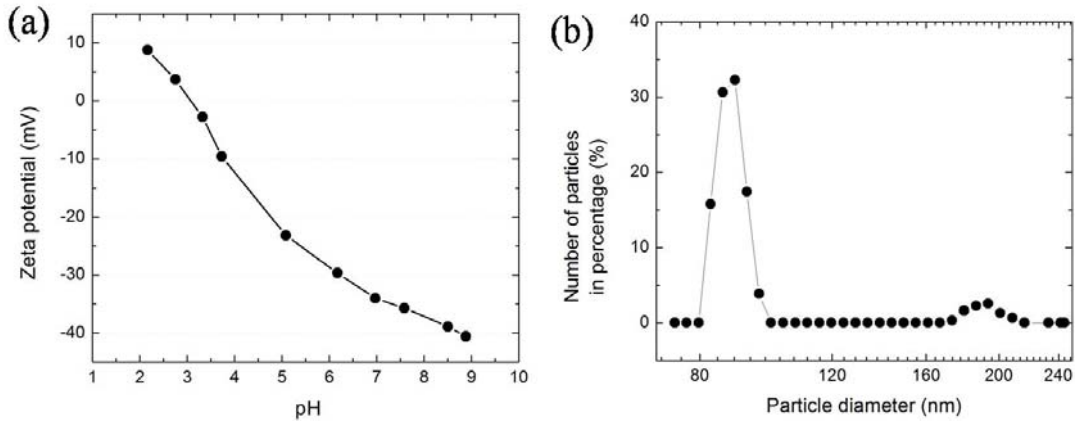

Fig. 2-3 (a) Zeta potential of $BaTiO_3$ nanoparticles colloidal suspension as a function of the pH of the solution. (b) Size distribution of the $BaTiO_3$ nanoparticles colloidal suspension measured by dynamic light scattering

2.2 Optical characterization of SHG signal from individual $BaTiO_3$ nanoparticles

We prepared isolated individual nanoparticles on an indium-tin-oxide (ITO) coated glass substrate for SHG characterization. The ITO-coated glass substrate is conductive which allowed us to image the nanoparticles by electron microscope. The ITO-coated glass substrate is also transparent, and therefore it is available for transmission optical measurement. We first imaged the sample by a SEM. With the help of the marks on the substrate, we imaged the same area with a SHG wide-field microscope shown in Fig. 2-4. For optical characterizations, the nanoparticles were embedded into index-matching oil, sandwiched between the ITO-coated glass and a cover glass. The excitation was a linearly polarized Ti:sapphire oscillator (150 fs pulse duration centered at 800 nm wavelength with a 76 MHz repetition rate). The excitation polarization can be controlled by a half-wave plate ($\lambda/2$ in Fig. 2-4). The laser beam was slightly focused by a lens of 5 cm focal length (L1 in Fig. 2-4) to reach the peak intensity of 1 GW/cm^2 on the sample. The SHG signal was collected by a 100X 1.4 numerical aperture (NA) oil-immersion objective (UPLSAPO 100XO, Olympus) in the forward direction and imaged directly on an electron multiplying charge coupled device (EMCCD, Andor iXonEM+ 885) with a lens of 20 cm focal length (L2 in Fig. 2-4). The excitation was removed by using narrow band-pass filters centered at 400 nm.

The SEM image of $BaTiO_3$ nanoparticles randomly deposited on ITO-coated glass is shown in Fig. 2-5 (a). The nanoparticles are well isolated and good for optical characterization. Fig. 2-5 (b) is the SHG microscopic image of the same nanoparticles as those shown in Fig. 2-5 (a). One-to-one correspondence can be seen between Fig.

2-5 (a) and (b). The spatial resolution in Fig. 2-5 (b) is limited by the diffraction of light at the SHG wavelength. The average SHG photon flux generated from a 90 nm $BaTiO_3$ nanoparticle is on the order of 10^5 photons/second under the peak excitation intensity of 1 GW/cm^2 (150 fs pulse width, 76 MHz repetition rate), which is sufficient for imaging applications. The SHG intensity of individual nanoparticles is different due to the varying sizes and nanoparticle orientations. The polarization-dependent SHG response will be discussed in the next section. To confirm the signal observed on the EMCCD was indeed SHG, we measured the power dependency and optical spectrum of the signal. In the power dependency measurement, we changed the excitation (pump) peak intensity from 0.1 to 4 GW/cm^2, and we captured one SHG image for each excitation condition. The SHG signal was calculated from image, and the relationship between the excitation intensity and the SHG signal is plotted in Fig. 2-6. The measured quadratic dependency indicates the signal is generated from a second-order process. We further measured the optical spectrum of the signal, which showed a clean signal at SHG wavelength at 400 nm (as shown in the inset of Fig. 2-6).

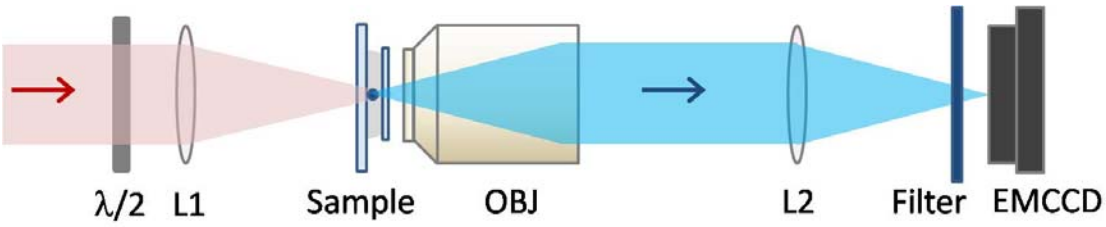

Fig. 2-4 Schematic diagram of the SHG wide-field microscope for SHG signal characterization. λ/2: half-wave plate, L1: 5 cm lens, OBJ: microscope objective, L2: 20 cm lens. The red beam shows the excitation at 800 nm, while the blue illustrate the SHG signal radiated from the nanoparticles under excitation.

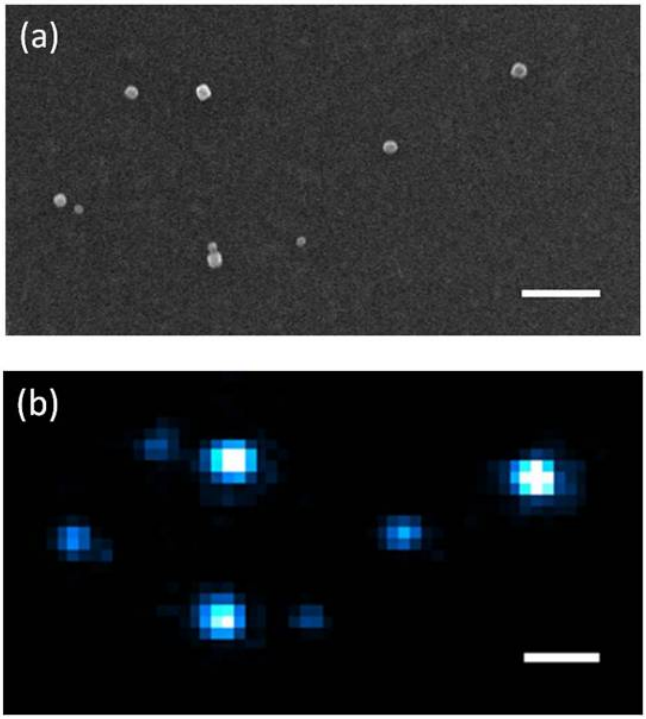

Fig. 2-5 (a) SEM image of $BaTiO_3$ nanoparticles. (b) Wide-field SHG microscopic image of the corresponding $BaTiO_3$ nanoparticles. One-to-one correspondence can be seen between (a) and (b). The scale bars are 500 nm.

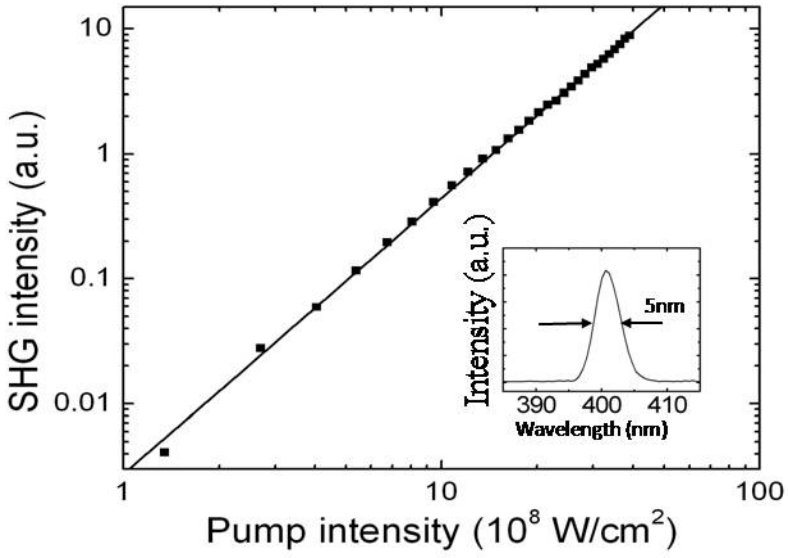

Fig. 2-6 Power dependence of the SHG signal from $BaTiO_3$ nanoparticles in double logarithmic scale. The squares are measured results and the solid line is the linear fit with the slope of 2.2. The inset shows the SHG optical spectrum centered at 400.6 nm with a full-width half-maximum of 5 nm.

Next, we verified the stability of the SHG signal radiated from $BaTiO_3$ nanoparticles. The SHG process is lack of real-state transition, so a stable SHG signal is expected. Such stable signal makes SHG nanoparticles promising as long-term imaging probes. We used a similar SHG wide-field microscope as shown in Fig. 2-4 for stability measurement. The excitation laser beam of 258 mW average power was slightly focused by a lens down to an excitation area of 100 μm in diameter. The peak excitation intensity was 6.85×10^7 W/cm^2. The SHG signal was collected by a 20X 0.42 NA long working distance objective (Edmund Optics, NT46-145) in the forward direction and imaged directly on the EMCCD with a lens of 30 cm focal length. The excitation was removed by using narrow band-pass filters centered at 400 nm. Fig. 2-7 (a) shows the wide-field SHG images of an isolated 300 nm diameter $BaTiO_3$ nanoparticle. The acquisition time of the EMCCD was set to be 0.1 second with gain of 30, and the SHG signal is sufficient for imaging. The total number of SHG photons arrived on the EMCCD was measured as 5.7×10^4 photons/second. The stability measurement was performed by taking one SHG image of the nanoparticle every one minute for 5 hours under continuous excitation. The SHG signal was extracted from each image after background subtraction. The total collected SHG strength was measured by integrating the SHG signal within the bright spot in the image. We plotted the SHG signal as a function of time in Fig. 2-7 (b) where the signal intensity remains unchanged after 5 hour continuous excitation. The total emission SHG photon is estimated to be more than 10^9, showing that the SHG signal from the nanoparticle is extremely stable. The relative standard deviation of the signal is 5.23% which is expected to be due to the laser noise and the detector noise.

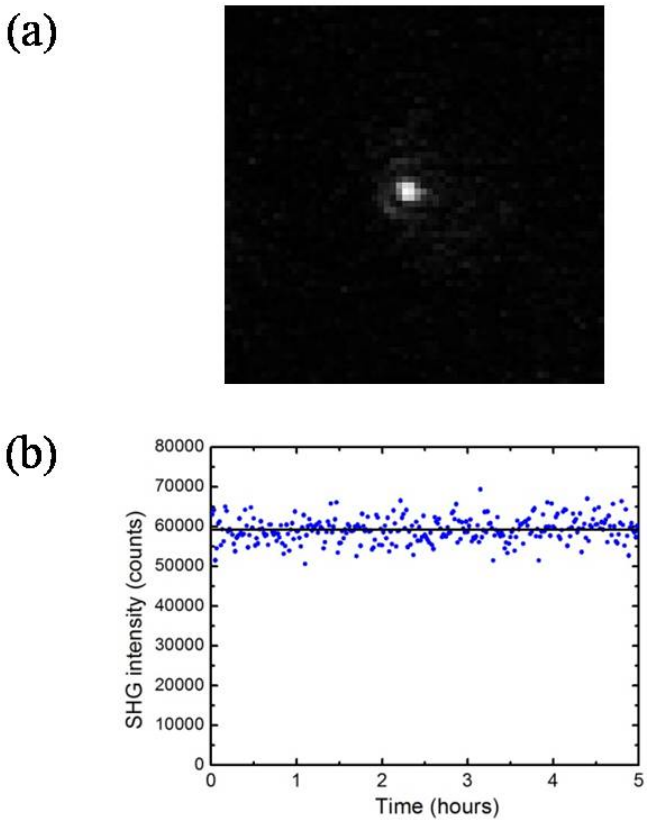

Fig. 2-7 Long-term imaging with SHG nanoparticles. (a) Wide-field SHG image of an isolated $BaTiO_3$ nanoparticle. The size of the image is 15 × 15 μm^2. (b) The time-lapse SHG signal of the nanoparticle under 5 hour continuous excitation. The dots represent experimental measurements and the line shows the average of the signal. The signal intensity remains unchanged after the emission of > 10^9 photons.

To describe the brightness of $BaTiO_3$ nanoparticles more quantitatively, we define the SHG cross section σ_{SHG} as follows:

$$W_0 = \sigma_{SHG} {I_0}^2. \tag{2-1}$$

where W_0 is the total SHG radiated power from a nanoparticle, $I_0 = \left|\boldsymbol{E}_m{}^{(\omega)}\right|^2/2Z_m$ is the excitation intensity, and Z_m is the wave impedance of the medium. The concept of SHG cross section is very similar to the two-photon fluorescent cross section, which has been widely used to describe the brightness of two-photon fluorescent markers. However, it is worth noting that the mechanisms of the two processes are very different. SHG is a process without a real state transition. Therefore, σ_{SHG} of a SHG

nanoparticle simply describes how efficient a nanoparticle can scatter at the SHG frequency under excitation at the fundamental frequency. On the other hand, two-photon fluorescence involves a two-photon absorption followed by a fluorescence emission. As a result, the two-photon (action) cross section σ_{2P} of two-photon fluorescent markers is the product of the two-photon absorption cross section and the fluorescent quantum efficiency. Despite the differences in the two mechanisms, it is very helpful to compare the SHG cross section σ_{SHG} with two-photon fluorescent cross section σ_{2P}, especially when using SHG nanoparticles as imaging probes of nonlinear microscopy. The unit of σ_{SHG} and σ_{2P} is Goeppert-Mayer (1 GM = 10^{-50} cm^4 sec $photon^{-1}$).

Based on equation (2-1), σ_{SHG} can be measured experimentally since both the SHG radiation power W_0 and the excitation intensity I_0 are measurable. We have measured the σ_{SHG} of a single 100 nm $BaTiO_3$ nanoparticle to be on the order of 10^3 GM [63]. This experimental observation agrees well with our theory which will be discussed shortly in the next section. Notice that σ_{SHG} has a sixth-order scaling rule on the diameter of the nanoparticle, so the size effect on SHG efficiency is significant [46]. As a reference, the σ_{2P} of the commonly used fluorescent bio-markers are listed: ~ 10^4 GM for 5 nm quantum dots [7]; ~ 10^2 GM for fluorescent proteins [83] and organic dyes [84]. In general, the two-photon fluorescent efficiency depends strongly on the excitation wavelength due to the resonant absorption. In our laboratory, it has been demonstrated the SHG efficiency can be enhanced by 500 times by creating a plasmonic resonant nanoshell around the nanoparticle, and an enhancement of 3500 is theoretically possible [63].

2.3 Polarization-dependent SHG response from $BaTiO_3$ nanoparticles

In this section, the polarization-dependent SHG response from nanoparticles of noncentrosymmetric materials will be discussed in detail. It includes theoretical calculations of SHG signal from nanoparticles under plane wave and tightly focused excitation. The plane wave excitation is for SHG wide-field microscopy, while the tightly focused excitation is for SHG scanning microscopy. We use $BaTiO_3$ nanoparticles as the example of our calculations, but the theory is valid for any nanoparticle of known bulk second-order nonlinearity. The section ends with experimental observations which match well with the theoretical calculations.

2.3.1 Theory for plane-wave excitation

We start the study with a nanoparticle under a uniform linearly polarized (LP) excitation using $BaTiO_3$ nanoparticles. The crystal structure of the $BaTiO_3$ nanoparticle is tetragonal, which is uniaxial and belongs to symmetry class 4 [23]. Due to the crystal symmetry, the SHG response is determined only by the orientation of the c-axis of the nanoparticle, and the rotation of the nanoparticle around the c-axis has no influence on the SHG response. The orientation of an object in a three-dimensional (3D) space can be defined by three Euler angles in an Euler coordinate. To define the orientation of the c-axis in space, the degree of freedom is reduced to two angles which can be described in a spherical coordinate. The orientation of the c-axis of the nanoparticle can be uniquely defined by the angles θ_0 and ϕ_0 in the spherical coordinate, as shown in Fig. 2-8. The incident excitation propagates along the Z axis and the excitation polarization angle γ can be rotated in the XY plane by a half-wave plate.

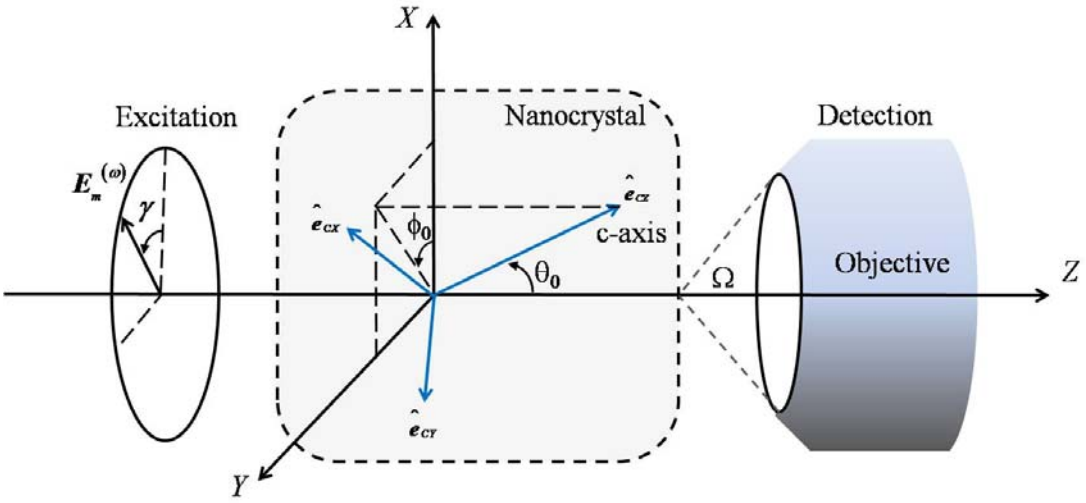

Fig. 2-8 Schematic diagram of a $BaTiO_3$ nanoparticle oriented at an arbitrary direction under a LP plane-wave excitation. The SHG signal is collected by a microscope objective.

Assuming the shape of the nanoparticle is spherical and the size is small compared with the wavelength of excitation, the nanoparticle can be considered as a Rayleigh particle [85]. By further ignoring the material birefringence, the electric field inside the nanoparticle $\boldsymbol{E}_p{}^{(\omega)}$ can be found to be in-phase and uniform as $\boldsymbol{E}_p{}^{(\omega)} = \left[3\varepsilon_m/\left(\varepsilon_p + 2\varepsilon_m\right)\right]\boldsymbol{E}_m{}^{(\omega)}$ [85] $\boldsymbol{E_1}(\omega) = \frac{3\varepsilon_2}{\varepsilon_1+2\varepsilon_2}\boldsymbol{E_2}(\omega)$, where $\boldsymbol{E}_m{}^{(\omega)}$ is the incident electric field in the surrounding medium in the absence of the particle, and ε_p and ε_m are the linear permittivities of the particle and the surrounding medium, respectively. The electric field $\boldsymbol{E}_p{}^{(\omega)}$ at the fundamental frequency ω is then decomposed into three orthogonal components along the three axes in the crystal frame, i.e., $\boldsymbol{E}_p{}^{(\omega)} = E_{CX}\hat{\boldsymbol{e}}_{CX} + E_{CY}\hat{\boldsymbol{e}}_{CY} + E_{CZ}\hat{\boldsymbol{e}}_{CZ}$ where $\hat{\boldsymbol{e}}_{CX}$, $\hat{\boldsymbol{e}}_{CX}$, and $\hat{\boldsymbol{e}}_{CZ}$ are unit vectors in the crystal frame as shown in Fig. 2-8. The SHG polarizations along the three crystal axes are related to $\boldsymbol{E}_p{}^{(\omega)}$ by [23]

$$\boldsymbol{P}^{(2\omega)} = \overline{\overline{\boldsymbol{d}}} \cdot \boldsymbol{E}_p{}^{(\omega)} \cdot \boldsymbol{E}_p{}^{(\omega)} = \begin{bmatrix} 0 & 0 & 0 & 0 & d_{15} & 0 \\ 0 & 0 & 0 & d_{15} & 0 & 0 \\ d_{31} & d_{31} & d_{33} & 0 & 0 & 0 \end{bmatrix} \begin{bmatrix} E_{CX}{}^2 \\ E_{CY}{}^2 \\ E_{CZ}{}^2 \\ 2E_{CY}E_{CZ} \\ 2E_{CX}E_{CZ} \\ 2E_{CX}E_{CY} \end{bmatrix}, \quad (2\text{-}2)$$

where $\overline{\overline{\boldsymbol{d}}}$ is the second-order susceptibility tensor of the bulk $BaTiO_3$ crystal. The values we used in the simulation are d_{15} = -41×10^{-9} esu, d_{31} = -43×10^{-9} esu, and d_{33} = -16×10^{-9} esu [23].

Because of the subwavelength particle size, the electrostatic approximation holds, and the induced SHG polarizations are uniform inside the particle. By assuming also that the size of the particle is much smaller than the SHG wavelength, the SHG polarizations within the particle can be regarded as three orthogonal SHG dipoles with the amplitudes proportional to the strengths of the polarizations. These three orthogonal SHG dipole moments radiate like antennas at the SHG frequency. The total SHG radiation power W_0 can be found as [86]

$$W_0 = \frac{ck^4V^2}{12\pi\varepsilon_0}\left|\boldsymbol{P}^{(2\omega)}\right|^2, \quad (2\text{-}3)$$

where c is the speed of light, k is the wave number at the SHG frequency, V is the volume of the nanoparticle, and ε_0 is the vacuum permittivity. Following equations (2-2) and (2-3), one can find that the total SHG power radiated from these three orthogonal dipoles is dependent on the orientation of the nanoparticle and the excitation polarization. Without losing generality, we assume that the c-axis of the nanoparticle is oriented at ϕ_0= 0 degrees in the following theoretical calculation. In Fig. 2-9 (a), we calculate and plot the total SHG power radiated by these three orthogonal dipoles as a function of excitation polarization γ (with respect to the X

axis as shown in Fig. 2-8) when the nanoparticle is orientated at θ_0= 10, 50, and 90 degrees.

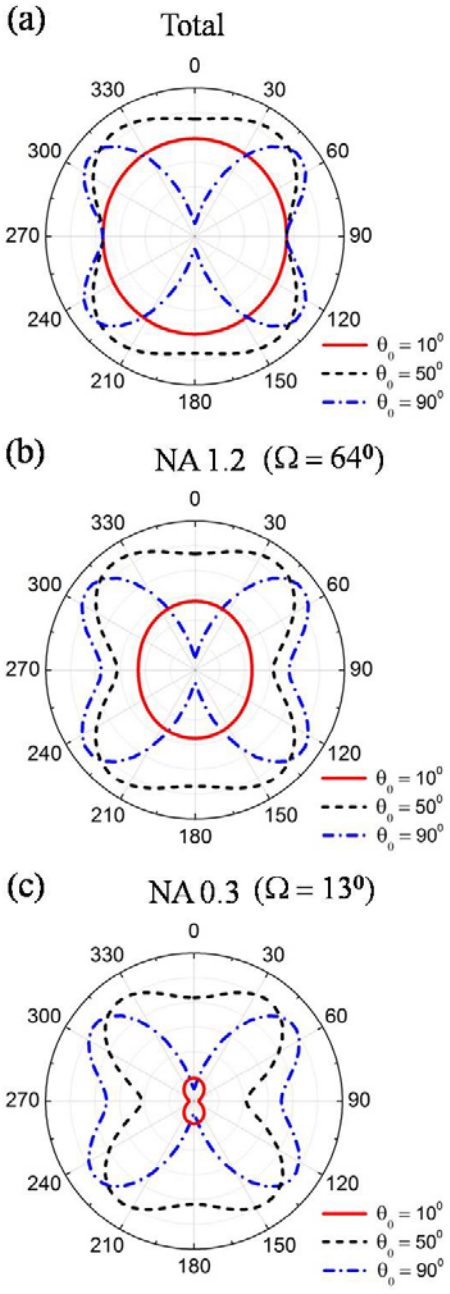

Fig. 2-9 Theoretical calculation of polarization-dependent SHG response of a $BaTiO_3$ nanoparticle under a plane-wave excitation. (a) The polarization dependency of the total SHG response of a $BaTiO_3$ nanoparticle. (b)(c) The polarization dependency of the SHG response of a $BaTiO_3$ nanoparticle where the SHG signal is collected by a (b) NA 1.2 water-immersion objective and (c) NA 0.3 water-immersion objective

In nonlinear microscopy, the SHG signal is usually collected by a microscope objective. Since the SHG radiation is generally not a simple spherical wave, we further consider the collection efficiency provided by the objective to obtain an accurate estimation of the polarization-dependent SHG response of a nanoparticle. The collection efficiency is determined by the overall far-field SHG intensity radiation pattern of the three orthogonal dipoles within the cone angle introduced by the objective. To calculate the collection efficiency, the three orthogonal dipoles are first projected back into the XYZ lab frame, namely $\boldsymbol{P}^{(2\omega)} = P_X\hat{\boldsymbol{e}}_X + P_Y\hat{\boldsymbol{e}}_Y + P_Z\hat{\boldsymbol{e}}_Z$, where $\hat{\boldsymbol{e}}_X$, $\hat{\boldsymbol{e}}_Y$, and $\hat{\boldsymbol{e}}_Z$ are unit vectors in the lab frame. Each of the three new defined SHG dipoles radiates SHG field in the form of dipole radiation pattern [86]. Therefore, the SHG electric field radiation pattern in spherical coordinates can be related to $\boldsymbol{P}^{(2\omega)}$ as:

$$\boldsymbol{E}^{(2\omega)}(\boldsymbol{R}) \propto \begin{bmatrix} 0 & 0 & 0 \\ \cos\theta\cos\phi & \cos\theta\sin\phi & -\sin\phi \\ -\sin\phi & \cos\phi & 0 \end{bmatrix} \begin{bmatrix} P_X \\ P_Y \\ P_Z \end{bmatrix} \begin{matrix} \hat{\boldsymbol{e}}_R \\ \hat{\boldsymbol{e}}_\Theta, \\ \hat{\boldsymbol{e}}_\Phi \end{matrix} \tag{2-4}$$

where $\hat{\boldsymbol{e}}_R$, $\hat{\boldsymbol{e}}_\Theta$, and $\hat{\boldsymbol{e}}_\Phi$ are the unit vectors in the spherical coordinate of the lab frame. The collection efficiency η can be easily found as the ratio of the SHG field intensity within the cone angle of the objective ($0 < \theta < \Omega$, $0 < \phi < 2\pi$) over the total SHG field intensity:

$$\eta = \frac{\int_0^{\Omega}\int_0^{2\pi}\left|\boldsymbol{E}^{(2\omega)}(\boldsymbol{R})\right|^2 \sin\theta\, d\phi\, d\theta}{\int_0^{\pi}\int_0^{2\pi}\left|\boldsymbol{E}^{(2\omega)}(\boldsymbol{R})\right|^2 \sin\theta\, d\phi\, d\theta}. \tag{2-5}$$

It is worth noting that η is a function of the cone angle Ω, the nanoparticle orientation, and the excitation polarization. We consider two cases where the SHG signal is collected by a high NA microscope objective (NA 1.2 water-immersion, Ω = 64.46 degrees) and a low NA microscope objective (NA 0.3 water-immersion, Ω = 13.04 degrees). Taking into account η for the collected SHG power, we plot the

detected polarization-dependent SHG responses for these two cases in Fig. 2-9 (b) and (c), respectively. In Fig. 2-9, it is obvious that higher NA detection gives a response closer to the total SHG signal. A substantial difference between Fig. 2-9 (a)–(c) takes place when θ_0 is small. This is because a stronger axial dipole component (P_Z) appears when θ_0 is small and the objective has a lower collection efficiency of the axial dipole than the transverse dipoles (P_X and P_Y).

2.3.2 Theory for tightly focused excitation

Laser scanning microscopy, such as scanning confocal microscopy, is the most popular SHG microscopy where a high NA objective tightly focuses the excitation beam to reach a high local intensity for efficient nonlinear phenomena to take place. The focus is scanned across the sample to form an image [31, 87]. The tightly focused excitation generates transverse and axial field components, which is known as the depolarization effect [88]. The depolarized excitation polarizations at the focus then participate in the SHG and can significantly modify the overall polarization-dependent SHG response [89, 90]. For the detection, the SHG signal is either collected by the same objective in epi-geometry or by another objective in the transmission geometry. A similar depolarization effect should also be considered in the detection for an accurate estimation.

We simulate the SHG response of a nanoparticle in a scenario of a scanning microscope, such as a scanning confocal microscope. It is convenient to introduce spherical polar coordinates as shown in Fig. 2-10. An LP (X-polarized for example) plane-wave excitation propagating in the Z direction of 812 nm wavelength is tightly focused by a NA 1.2 water-immersion objective and the beam waist is at $Z = 0$.

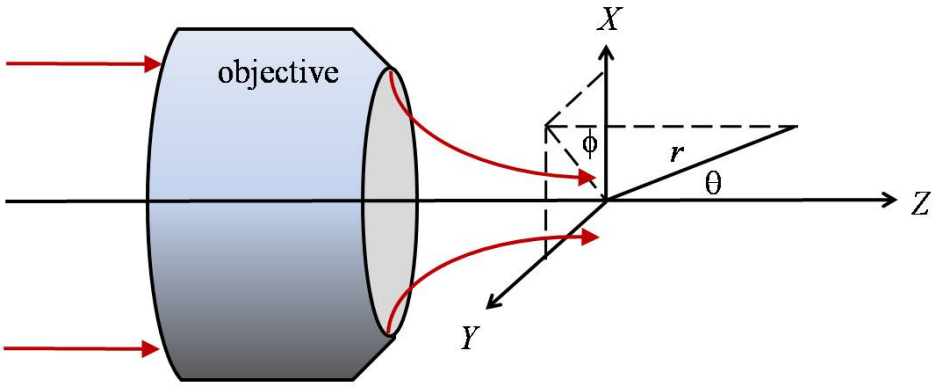

Fig. 2-10 Schematic diagram of a tightly focused excitation by using a microscopic objective.

The focused field at the beam waist can be written as [88]:

$$\begin{aligned} \mathrm{E_X}(\mathrm{r},\phi) &= -\mathrm{i}[\mathrm{f_0}(\mathrm{r}) + \mathrm{f_2}(\mathrm{r})\cos(2\phi)] \\ \mathrm{E_Y}(\mathrm{r},\phi) &= -\mathrm{if_2}(\mathrm{r})\sin(2\phi) \\ E_Z(r,\phi) &= -2f_1(r)\sin(\phi), \end{aligned} \tag{2-6}$$

where

$$\begin{aligned} f_0(r) &= \int_0^{\Omega} \sqrt{\cos\theta}\,\sin\theta\,(1+\cos\theta)J_0(kr\sin\theta)d\theta \\ f_1(r) &= \int_0^{\Omega} \sqrt{\cos\theta}\,\sin^2\theta\,J_1(kr\sin\theta)d\theta \\ f_2(r) &= \int_0^{\Omega} \sqrt{\cos\theta}\,\sin\theta\,(1-\cos\theta)J_2(kr\sin\theta)d\theta, \end{aligned} \tag{2-7}$$

and $r = \sqrt{X^2+Y^2} > 0$, $0 \le \phi < 2\pi$, and $J_n(\cdot)$ is the Bessel function of the first kind and order n.

The magnitudes and the phases of the three perpendicularly polarized fields at the beam waist $E_i|_{Z=0}$, $i = X, Y, Z$, are plotted in Fig. 2-11 (a)–(c) and (d)–(f), respectively. Besides the field at the original polarization (i.e., $E_X|_{Z=0}$), a considerable amount of axial component $E_Z|_{Z=0}$ appears which will participate in the SHG process.

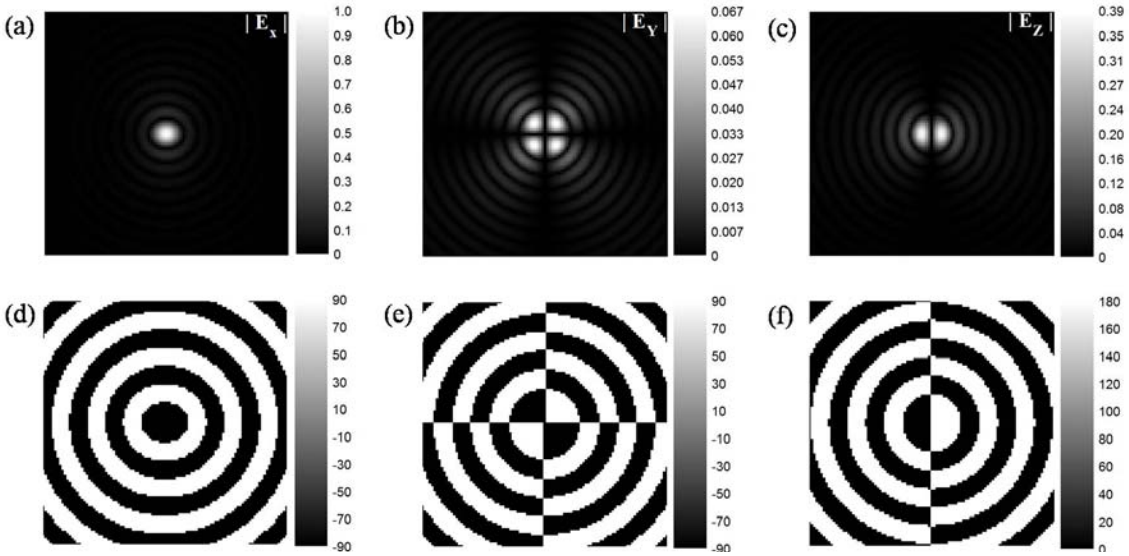

Fig. 2-11 Theoretical calculation of the tightly focused LP (X-polarized) excitation. The magnitude (a)–(c) and the phase (d)–(f) of the electric field of X-, Y-, Z-polarizations at the focused beam waist (Z = 0). The incidence is an X-polarized plane-wave of 812 nm wavelength which is focused by a NA 1.2 water-immersion objective in an index-matching environment. The size of the images are 6×6 μm^2.

In a scanning microscope, the calculated complex excitation patterns shown in Fig. 2-11 are scanned across a nanoparticle and a scanning image of a nanoparticle is formed. The pixel size in Fig. 2-11 is 60×60 nm^2, corresponding to a scanning step size of 60 nm. Assuming the nanoparticle is much smaller than the focused spot of the excitation, while the excitation patterns are scanned across, it will pick up the local excitation fields calculated at each pixel as a plane-wave excitation and emit SHG signal as described in the previous section. Under this assumption, the theoretical SHG scanning image can be obtained by calculating the SHG signal from the nanoparticle pixel-by-pixel based on the excitation patterns. The finite size of the nanoparticle in reality would make the measured SHG response deviate from this theoretical estimation. We integrate the SHG intensity over the whole scanning image to represent the SHG response of a nanoparticle at certain orientation and under a specific excitation polarization using a scanning microscope.

The theoretical polarization-dependent SHG response of a nanoparticle under a tightly focused excitation (NA 1.2 water-immersion objective) is plotted in Fig. 2-12 where the nanoparticles orientated at θ_0 = 10, 50, and 90 degrees are considered. Similar to the analysis of plane-wave excitation, we calculate the total SHG signal and also the signal collected by NA 1.2 and NA 0.3 water-immersion objectives, as shown in Fig. 2-12 (a), (b), and (c), respectively. We find Fig. 2-12 (a)–(c) to have a similar behavior as Fig. 2-9 (a)–(c), i.e., the decrease of the collected SHG signal when the NA decreases at small θ_0, which is due to the collection efficiency of the objective. We also find that a tightly focused beam results in a slightly different SHG polar response from a uniform excitation: where the uniform excitation gives a weak SHG signal, such as θ_0= 90 degrees and γ = 0 degrees, the tightly focused excitation gives a stronger SHG signal due to the depolarization effect. In other words, the depolarization effect induces new excitation polarizations, which results in an averaging effect in the SHG polar response.

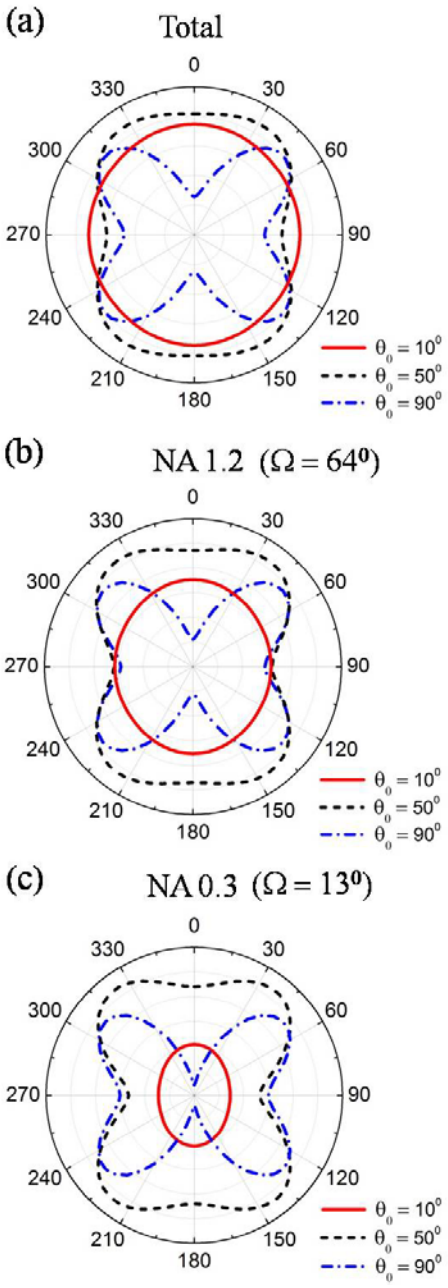

Fig. 2-12 Theoretical calculation of the polarization-dependent SHG response of a $BaTiO_3$ nanoparticle in a scanning image with a tightly focused excitation (NA 1.2 water-immersion objective). (a) The polarization dependency of the total SHG response of a $BaTiO_3$ nanoparticle. (b) (c) The polarization dependency of the SHG response of a $BaTiO_3$ nanoparticle where the SHG signal is collected by a (b) NA 1.2 water-immersion objective and (c) NA 0.3 water-immersion objective

2.3.3 Measurements of SHG polar response of the nanoparticles

We used a standard scanning confocal microscope (Leica SP5) to excite and to detect SHG signal from individual $BaTiO_3$ nanoparticles randomly deposited on an ITO-coated glass substrate. The nanoparticles were immersed in water for the confocal microscope measurement with a water-immersion objective. Fig. 2-13 is a typical SEM image of the nanoparticles prepared on an ITO coated glass slide. It shows that most of the nanoparticles on the glass slide are isolated single nanoparticles. The excitation light source was a Ti:sapphire oscillator (Chameleon Ultra II, Coherent) generating 140 fs laser pulses at 812 nm wavelength and 80 MHz repetition rate. The average excitation power is approximately 15 mW. The excitation was tightly focused by a 63X NA 1.2 water-immersion objective and the SHG signal was collected by the same objective in an epi-geometry. The SHG signal was detected by a photomultiplier (R6357, Hamamatsu) and the ambient light was rejected by a narrow bandpass optical filter centered at 406 nm with 15 nm bandwidth. The excitation polarization is controlled by a half-wave plate or a quarter-wave plate placed in the excitation beam before it enters the confocal microscope.

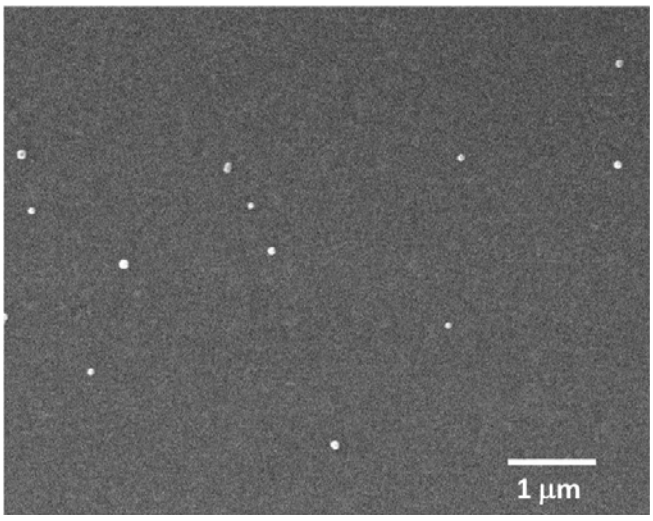

Fig. 2-13 SEM image of isolated $BaTiO_3$ nanoparticles randomly deposited on an ITO coated glass substrate for SHG polarization measurement

Fig. 2-14 shows a typical SHG confocal image of the nanoparticles under an LP excitation, where the sample was prepared in a similar way as for the SEM measurement. The SHG signal from individual nanoparticles shows great contrast. The background SHG from the ITO/water interface is relatively weak. The pixel size in Fig. 2-14 is 60×60 nm^2. The full-width at half-maximum (FWHM) of the SHG imaging spot size of the $BaTiO_3$ nanoparticle is about 300 nm, which matches well with the diffraction-limited spot size at the SHG wavelength based on a tightly focused excitation beam described in the previous section. The SHG intensity of individual nanoparticles varies due to the size-dependent and also the polarization-dependent SHG signal. Based on the SHG efficiency of $BaTiO_3$ nanoparticles described by equation (2-3), we estimate the average power of the SHG signal from the $BaTiO_3$ nanoparticles in our measurement is approximately 10–100 pW.

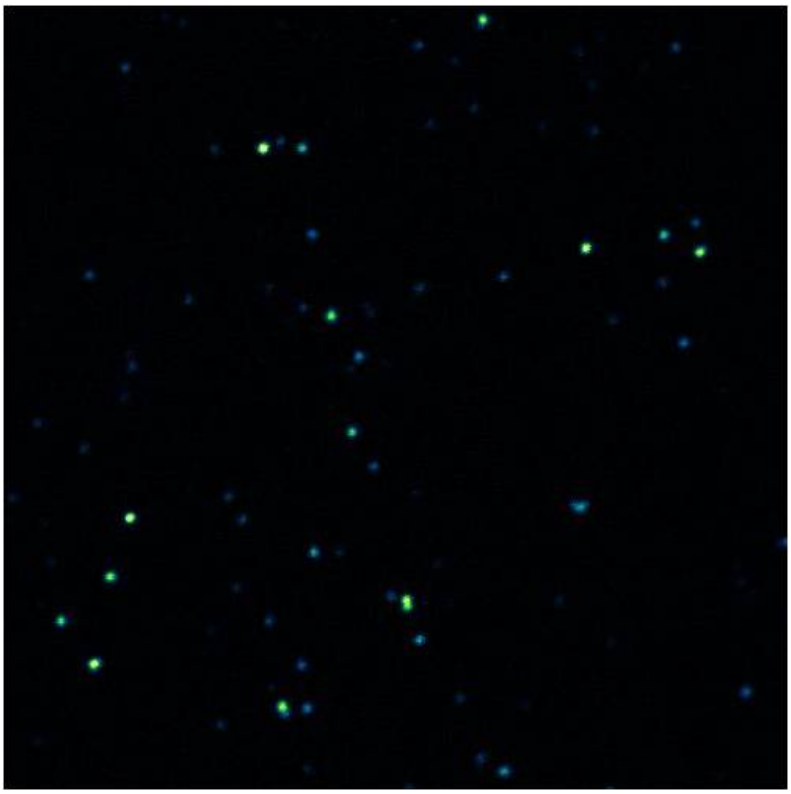

Fig. 2-14 Scanning confocal SHG image of $BaTiO_3$ nanoparticles on an ITO coated glass substrate. The size of the image is 30×30 μm^2.

We measured the polarization-dependent SHG response from individual nanoparticles by rotating LP excitation with a half-wave plate. One SHG confocal image was captured for each excitation polarization direction. The excitation polarization was rotated from 0 to 180 degrees with a 10 degree angular step size. We calibrated the excitation power at the sample position as it varies about 5% when the excitation polarization changes due to the polarization-dependent response of the confocal microscope. Fig. 2-15 shows the images of three isolated nanoparticles under LP excitations of different polarization orientations. The polarization-dependent SHG signal is clearly observed.

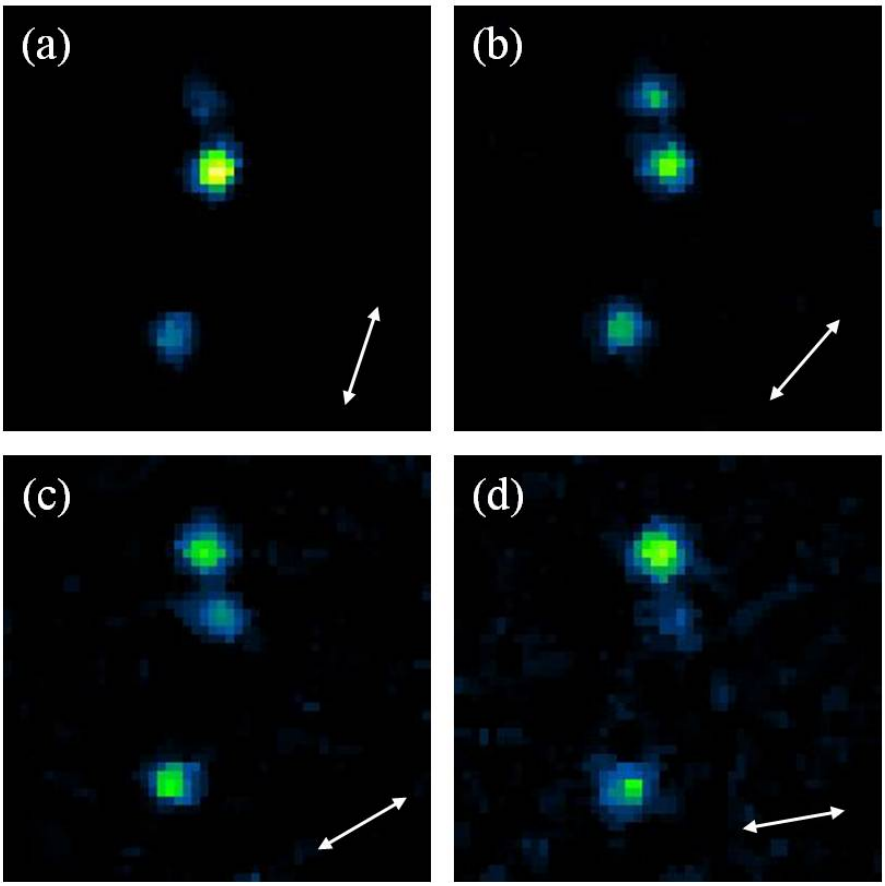

Fig. 2-15 Scanning confocal SHG images of $BaTiO_3$ nanoparticles under different LP excitation orientations. From (a)–(d), the excitation polarizations were 20, 40, 60, and 80 degrees, respectively, as indicated in the individual figures. The size of the images is $3 \times 3\ \mu m^2$.

The SHG response of individual nanoparticles was found by integrating the SHG signal within the bright spot in the confocal image, while the background SHG from the ITO/water interface was subtracted. From the measured responses, we can retrieve the orientations of the nanoparticles by fitting with theoretical calculation. The theoretical calculations for the fitting are plotted in Fig. 2-16 where ϕ_0 = 0 degrees and θ_0= 0, 10… 90 degrees. As can be seen in Fig. 2-16, the fitting of the orientation of the nanoparticle is unique because each (θ_0, ϕ_0) pair gives a different polar response except the ambiguity between ϕ_0 and ϕ_0 + 180 degrees.

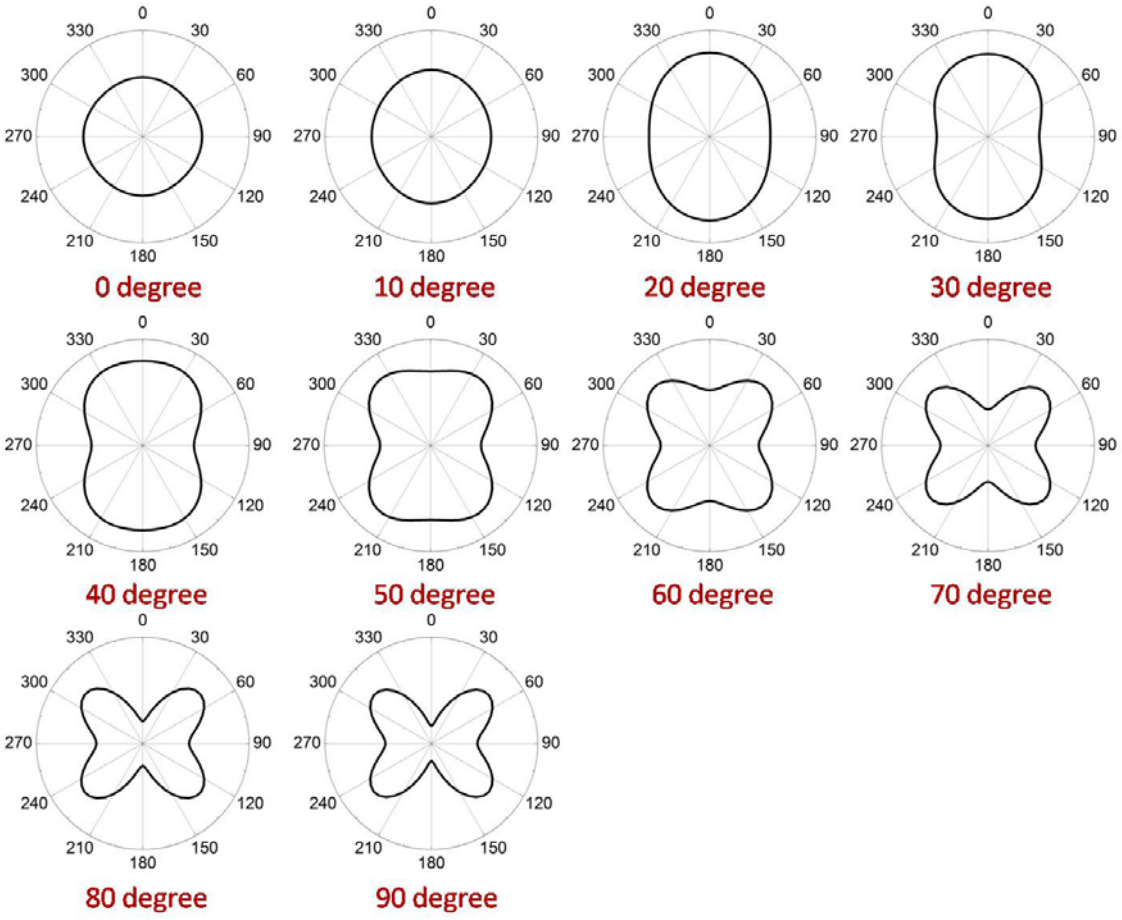

Fig. 2-16 Theoretical calculations of the polarization-dependent SHG response of $BaTiO_3$ nanoparticle at various orientation angles of θ_0, measured by a scanning confocal microscope. The orientation of the nanoparticle in the calculation is at ϕ_0 = 0 degrees.

Fig. 2-17 shows three representative polar diagrams of the SHG response of $BaTiO_3$ nanoparticle as a function of the excitation polarization. The measured responses agree well with the theoretical calculation. In the theoretical calculation, we assume the size of the nanoparticle is much smaller than the focused spot. In the experiment, the size of the nanoparticles was around 90 nm in diameter. The tightly focused spot size using an NA 1.2 water-immersion objective at 812 nm wavelength is about 480 nm FWHM transversely, which is more than 5 times greater than the particle size. In the axial direction, the depth of focus of the excitation is about 1 μm FWHM which is more than 10 times greater than the particle size. The good match between the measured and calculated polarization-dependent SHG responses shows the theoretical calculation is able to provide reasonable estimation. It also suggests our simple theoretical model in which the local excitation field of the nanoparticle is assumed to be a plane-wave, is valid in our experiment. Furthermore, it has been reported that for the particle size smaller than 150–200 nm in diameter under a tightly focused excitation at 945 nm wavelength, it is reasonable to use the single dipole approximation for the SHG emission [75]. Therefore, we believe the single dipole approximation is also valid for 90-nm-diameter particle under the 812 nm wavelength excitation, as in our scenario. In cases where we need to find a more accurate solution (i.e., for larger particles), one would need to calculate the excitation field inside the nanoparticle under a tightly focused excitation.

It is also interesting to consider the SHG response due to the abrupt 180 degree phase change in the tightly focused excitation pattern at the beam waist as shown in Fig. 2-11 (d)–(f). During the scanning, when the nanoparticle is at the boundary of the abrupt phase change, we will have an out-of-phase excitation on its two sides. The plane-wave excitation approximation will not hold in this situation. However, the

magnitude of the excitation field is always weak at these boundaries of abrupt phase change. Therefore, the abrupt phase change in the excitation pattern should have little effect on the overall SHG response. Furthermore, the Gouy phase shift of the focusing in the axial direction should also have little effect on the SHG response because the nanoparticle is small compared with the depth of focus of the excitation.

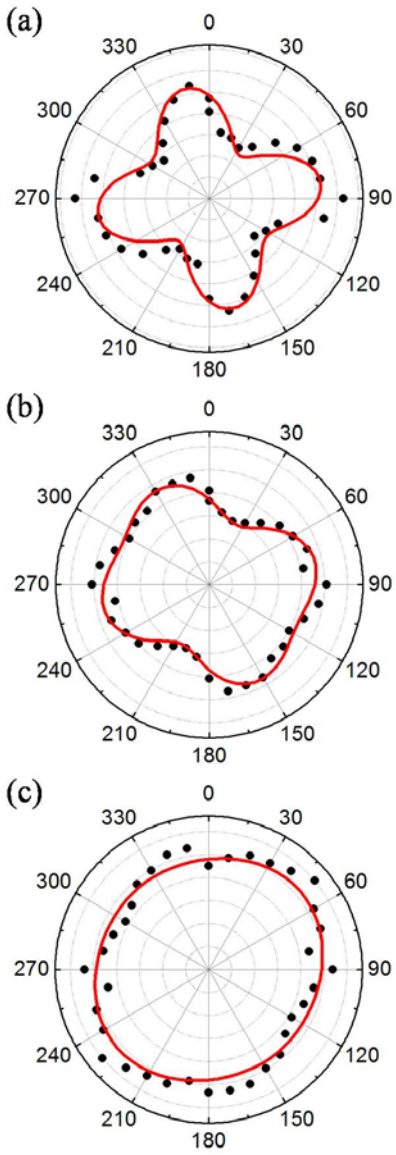

Fig. 2-17 (a)–(c) Polarization-dependent SHG response of three representative $BaTiO_3$ nanoparticles measured by a scanning confocal microscope. The experimental data are shown as black dots and the theoretical fits are shown as red curves. The three nanoparticles were found oriented at (θ_0 = 70 ± 5 degrees, ϕ_0 = 35 ± 5 degrees), (θ_0 = 50 ± 5 degrees, ϕ_0 = 115 ± 5 degrees), and (θ_0 = 10 ± 5 degrees, ϕ_0 = 50 ± 5 degrees), respectively. The 10 degree resolution of the fitting is due to the accuracy of the measurement.

2.4 Linearly and circularly polarized excitations

The polarization-sensitive SHG response provides the opportunity of detecting molecular structures much smaller than the optical diffraction limit. As demonstrated in the previous section, the orientation of nanoparticles can be measured by SHG polar response. Despite the merits offered by the polarization-sensitive SHG response, it may complicate a spatial distribution measurement of the SHG active targets of different orientations. As a result, circularly polarized (CP) excitation has been frequently adopted as an alternative excitation [91–93]. It is important to examine the SHG response under LP and CP excitations in SHG nonlinear microscopy. In this section, the SHG response of $BaTiO_3$ nanoparticles under a CP excitation will be studied both theoretically and experimentally. We show that the SHG response under a CP excitation is generally inferior to the average of the SHG responses under LP excitation over all orientations.

A CP excitation can be resolved into two perpendicular LP excitations, of equal amplitude, and in phase quadrature. Therefore, we can calculate the SHG response of a nanoparticle under a CP excitation based on the model established previously for the LP excitation. The SHG response of a $BaTiO_3$ nanoparticle under a CP excitation is plotted as a function of the nanoparticle orientation in Fig. 2-18. Due to the symmetry of the crystal structure, the SHG response from a $BaTiO_3$ nanoparticle is not sensitive to the handedness of CP excitations. In Fig. 2-18, we find that SHG signal monotonically decreases to zero when θ_0 decreases from 90 degrees to 0 degrees. This is the result of the interference effect between the two perpendicular LP excitations in quadrature resolved from the CP excitation and also the change of the effective nonlinear tensor due to the crystal orientations. Since the total SHG signal

from the nanoparticle oriented at small θ_0 under a LP excitation is considerable, as shown in Fig. 2-9 (a), the vanishing SHG signal of the nanoparticle oriented at small θ_0 under a CP excitation is therefore mostly due to the interference effect.

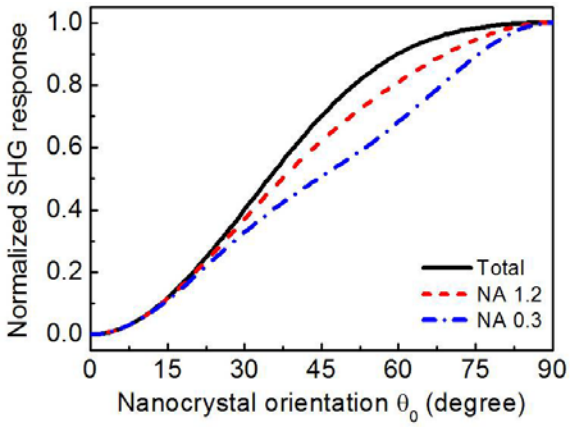

Fig. 2-18 Theoretical calculation of the normalized SHG response of a $BaTiO_3$ nanoparticle as a function of nanoparticle orientation under a CP plane-wave excitation. Different detection schemes are considered: total SHG response (black solid curve), collected by an NA 1.2 water-immersion objective (red dash curve), and collected by an NA 0.3 water-immersion objective (blue dash-dot curve).

The orientation of a $BaTiO_3$ nanoparticle at the time of measurement under excitation can be assumed to be random and equally likely to be in any orientation. With this assumption of a uniform probability density function we can readily calculate the mean and the standard deviation of the measured SHG signal. The relative standard deviation (i.e., the standard deviation divided by the mean) of the measured SHG signal under a CP plane-wave excitation is found to be 62.5±2 % for the cases ranging from the total SHG signal detection to low NA detection (NA 0.3 water-immersion objective). It is interesting to notice the small variation (±2 %) in the relative standard deviation when the NA of the collection objective changes. This implies that, under a CP excitation, the SHG radiation pattern does not vary a lot as the nanoparticle orientation changes. In fact, the radiation pattern is always dominated by the transverse dipoles (P_X and P_Y), which are less sensitive to the NA of detection.

To compare the SHG signal under LP and CP excitations, we calculate the relative standard deviation of the measured SHG signal under a LP plane-wave excitation. It is found to be: 20.9 % for the case of the total SHG signal detection, 31.2 % for the case of NA 1.2 water-immersion objective detection, and 58.5 % for the case of NA 0.3 water-immersion objective detection. The relative standard deviation of the signal increases significantly when the NA of the collection objective decreases. The effect of NA on the relative standard deviation of the SHG signal reflects the sensitivity of the collected SHG signal to the detection geometry, which is caused by the change in the SHG radiation pattern due to the combination of the nanoparticle orientation and the polarization-dependent SHG response.

The relative standard deviation of the SHG signal under a LP excitation can be greatly reduced if the excitation polarization can be rotated in the excitation plane (XY plane) within the time of measurement. When the excitation polarization rotates at an angular frequency much smaller than the optical frequency, it will excite the nanoparticle in all polarization directions (still limited in the XY plane) and the polarization-dependent SHG intensity due to the orientation variance in ϕ_0 will be averaged out. It should be emphasized that such “rotating LP excitation” is not CP excitation since the rotation frequency is much lower than optical frequency. To illustrate the differences between the two excitations, we plot the normalized SHG response of a $BaTiO_3$ nanoparticle under the rotating LP excitation as a function of the nanoparticle orientation θ_0 in Fig. 2-19. It is clear to see the difference between Fig. 2-18 and Fig. 2-19. We calculate the relative standard deviation of the measured SHG signal under this rotating LP plane-wave excitation. We found the reduced relative standard deviation to be: 9.5 % for total SHG signal detection, 19.4 % for NA 1.2 water-immersion objective detection, and 45.2 % for NA 0.3 water-immersion

objective detection. It is worth noting that the relative standard deviation of the SHG signal under CP excitation is much greater than that under the rotating LP excitation.

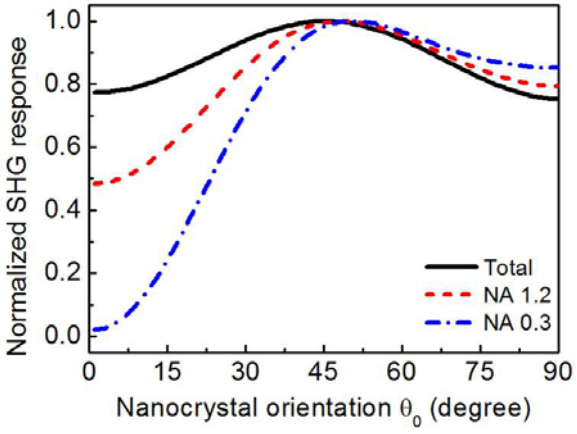

Fig. 2-19 Theoretical calculation of the normalized SHG response of a $BaTiO_3$ nanoparticle as a function of nanoparticle orientation under a rotating LP plane-wave excitation. Different detection schemes are considered: total SHG response (black solid curve), collected by an NA 1.2 water-immersion objective (red dash curve), and collected by an NA 0.3 water-immersion objective (blue dash-dot curve).

We further calculate the SHG response of a nanoparticle under a tightly focused CP excitation. Analogous to the plane-wave excitation, the CP excitation is first resolved into two perpendicular LP excitations of equal amplitude and in phase quadrature, and then depolarized through tightly focusing, respectively. The excitation field patterns of a tightly focused CP can be found, and therefore the SHG response can be calculated. The normalized SHG response is plotted as a function of the nanoparticle orientation in Fig. 2-20. Significant difference can be seen between Fig. 2-18 and Fig. 2-20. While the normalized SHG response drops from 0.3 to 0 as θ_0 decreases from 30 degrees to 0 degrees for the plane-wave excitation (in Fig. 2-18), it remains at around 0.3 for the tightly focused excitation (in Fig. 2-20). This is because the SHG polarization induced by the tightly focused CP excitation does not cancel out completely due to the depolarization effect.

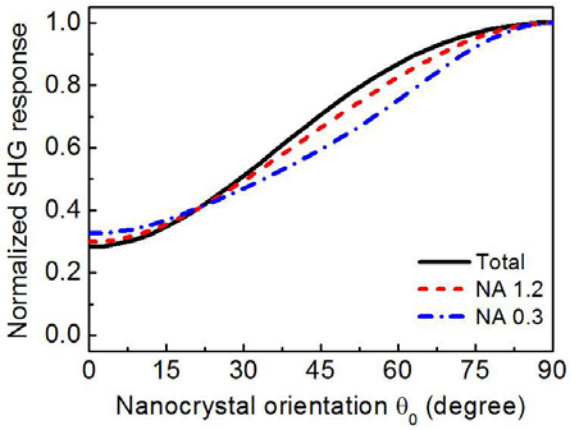

Fig. 2-20 Theoretical calculation of the normalized SHG response of a $BaTiO_3$ nanoparticle as a function of nanoparticle orientation under a CP tightly focused excitation. Different detection schemes are considered: total SHG response (black solid curve), collected by an NA 1.2 water-immersion objective (red dash curve), and collected by an NA 0.3 water-immersion objective (blue dash-dot curve).

We also calculate the relative standard deviation of the SHG signal under a tightly focused CP excitation. The relative standard deviation is calculated as 37.5±1 % for the cases ranging from the total SHG signal detection to low NA detection (NA 0.3 water-immersion objective). The much smaller relative standard deviation compared with the CP plane-wave excitation (62.5±2 %) again shows that a tightly focused excitation can reduce the variance of the polarization dependent SHG signal. The small range (±1%) of the relative standard deviation is also consistent to the case of CP plane-wave excitation.

To complete our comparison, we calculate the relative standard deviations of the SHG signal under tightly focused LP and rotating LP excitations. For tightly focused LP, the relative standard deviation is calculated to be: 17.0 % for the case of the total SHG signal detection, 22.8 % for the case of NA 1.2 water-immersion objective detection, and 40.9 % for the case of NA 0.3 water-immersion objective detection. The smaller relative standard deviation shows that a tightly focused excitation can reduce the variance of the polarization-dependent SHG signal. We also calculate the

relative standard deviation of the SHG signal with tightly focused rotating LP excitation, which is calculated to be: 9.8 % for total SHG signal detection, 13.2 % for NA 1.2 water-immersion objective detection, and 29.2 % for NA 0.3 water-immersion objective detection. The averaging effect due to the rotating LP excitation is again obvious. We plot the normalized SHG response of a $BaTiO_3$ nanoparticle under the tightly focused rotating LP excitation as a function of the nanoparticle orientation θ_0 in Fig. 2-21.

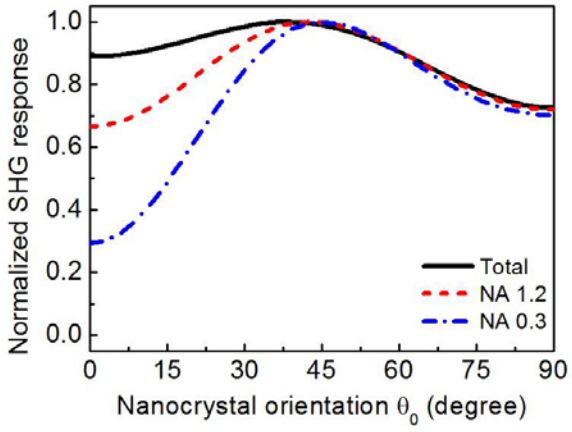

Fig. 2-21 Theoretical calculation of the normalized SHG response of a $BaTiO_3$ nanoparticle as a function of nanoparticle orientation under a tightly focused rotating LP excitation. Different detection schemes are considered: total SHG response (black solid curve), collected by an NA 1.2 water-immersion objective (red dash curve), and collected by an NA 0.3 water-immersion objective (blue dash-dot curve).

We summarize the relative standard deviation of the SHG signal from a $BaTiO_3$ nanoparticle under different excitation geometry (plane-wave and tightly focused excitations) of different polarizations (LP, rotating LP and CP) and also for different NA of the detection in Table 2-1. It is clear to see that the focused excitation and the high NA of the detection can reduce the effect of the polarization-dependent SHG signal. The difference between the rotating LP excitation and CP excitation is significant. As a result, we suggest using a rotating LP excitation for SHG microscopy for the least-polarization-dependent SHG signal. The rotating LP excitation can be

obtained by mechanically rotating a half-wave plate in the excitation. In the case of CP excitation, both for the plane-wave and focused excitations, the relative standard deviation of the SHG signal is not sensitive to the NA of detection. However, the relative standard deviation of the SHG signal is usually greater under CP excitation than under LP excitation. The CP excitation only provides lower relative standard deviation in the signal when the NA of detection is low.

Table 2-1. Relative standard deviation of the SHG signal

		Total	NA 1.2 detection	NA 0.3 detection
Plane-wave excitation	LP	20.9 %	31.2 %	58.5 %
	Rotating LP	9.5 %	19.4 %	45.2 %
	CP	60.5 %	61.5 %	64.3 %
Focused excitation (NA 1.2)	LP	17.0 %	22.8 %	40.9 %
	Rotating LP	9.8 %	13.2 %	29.2 %
	CP	38.4 %	37.6 %	36.8 %

We verify our theoretical study by measuring the SHG response of 39 nanoparticles under both LP and CP excitations. For LP excitation, one SHG confocal image was captured for each LP excitation orientation. The excitation polarization orientation was rotated from 0 to 180 degrees with a 10-degree angular step size. Notice that the averaged SHG signal between these images can be treated as the SHG signal under a rotating LP excitation. For CP excitation, the intensity was kept the same as the LP excitation, and one SHG confocal image was recorded. We then compared the measured SHG response of a nanoparticle under a CP excitation with that under the rotating LP excitations.

A parameter $\rho_{CP/LP}$ is defined as the ratio of the SHG response under a CP excitation to that under a rotating LP excitation of the same excitation intensity:

$$\rho_{CP/LP}(\theta_0) = \frac{W_{CP}(\theta_0)}{\int_0^{2\pi} W_{LP}(\theta_0,\gamma)d\gamma/2\pi}, \quad (2\text{-}8)$$

where $W_{CP}(\theta_0)$ is the SHG power from a nanoparticle oriented at θ_0 under a CP excitation, and $W_{LP}(\theta_0, \gamma)$ is the SHG power from a nanoparticle oriented at θ_0 under a LP excitation at excitation polarization angle γ. Thus, the denominator is equivalent to the average SHG power of a nanoparticle under a rotating LP excitation.

From the measured SHG responses of the nanoparticles under CP and LP excitations, we obtained the ratio $\rho_{CP/LP}$ for each of the measured 39 nanoparticles. The values of the ratio $\rho_{CP/LP}$ are plotted with the corresponding fitted nanoparticle orientations θ_0 for all 39 nanoparticles shown in Fig. 2-22 as blue dots. We also plot the theoretical calculation of $\rho_{CP/LP}$ in Fig. 2-22, which is based on the model described previously, considering the tightly focused excitation and the collection efficiency provided by the objective. We found the experimental data agrees very well with the theoretical calculation. In Fig. 2-22, it is clear that the SHG response of a nanoparticle under CP excitation is not simply an average of the SHG responses under LP excitations over the excitation polarizations (otherwise the curve should be a flat line at value of 1).

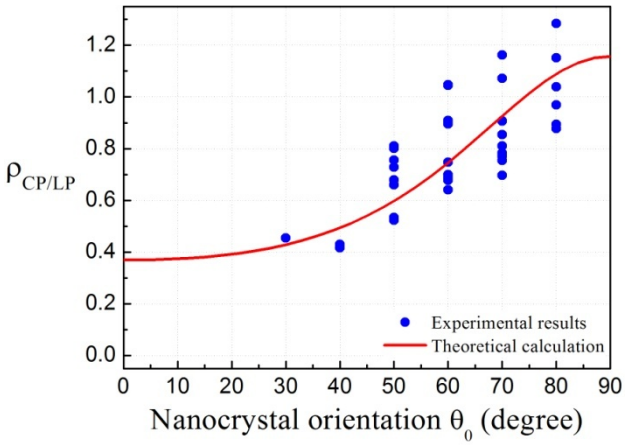

Fig. 2-22 Relative SHG response of 39 $BaTiO_3$ nanoparticles under tightly focused CP and rotating LP excitations correlated to the nanoparticle orientations. The red solid curve is the theoretical calculation considering a tightly focused excitation, while the blue dots are the experimental results.

We note that it has been reported that an extra ellipticity in the excitation polarization may be introduced from the scanning system and the dichroic mirror due to their polarization-sensitive reflective properties [35, 94, 95], which may influence the measured results of CP excitation. However we have not observed a substantial ellipticity polarization introduced to the excitation in our imaging system. The degree of polarization (DOP) is measured to be between 0.92–0.98 for all the LP excitations. The theoretical calculation shown in Fig. 2-22 is made under the assumption that DOP is equal to 1. We roughly estimate the overall ellipticity effect in our system with the averaged value of DOP as 0.95 by using a corresponding elliptical polarization as the excitation in the calculation. By taking into account the ellipticity in the excitation, we plot the theoretical ratio $\rho_{CP/LP}$ as a function of nanoparticle orientation θ_0 in Fig. 2-23, along with the experimental data. The two theoretical calculations for DOP as 0.95 and 1 show similar behaviors, and they reasonably agree with the experimental data. Slightly more derivation is observed at small θ_0 which may be due to the

imperfect measurement. Therefore, we believe the ellipticity effect in the excitation polarization in our system is not significant.

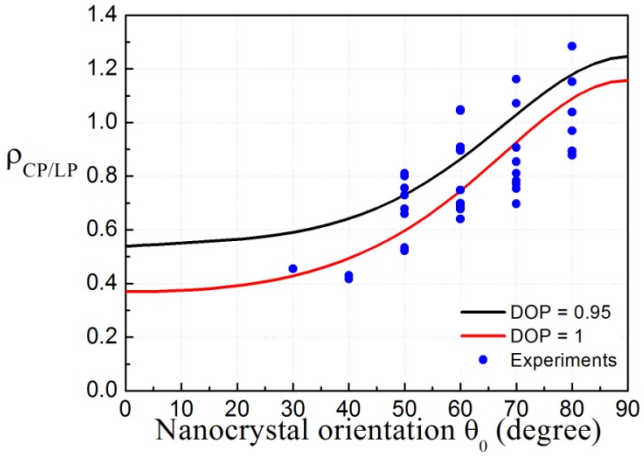

Fig. 2-23 Evaluation of the ellipticity effect in the excitation polarization on the relative SHG response of $BaTiO_3$ nanoparticles under CP and LP tightly focused excitations correlated to the nanoparticle orientations. The black/red curve is the theoretical calculation considering with/without ellipticity in the excitation introduced by the system, while the blue dots are the experimental results.

Chapter 3 Cellular imaging with SHG nanoparticles

Detecting and tracing specific molecules of interest are important for studying the function and the behavior of biological systems. Biomarkers have been developed to achieve this goal by creating a contrast between signal and background. SHG nanoparticles have shown promise as imaging probes for biological imaging due to the stable and coherent signal. For biological applications, it is critical for the markers to be non-toxic and also to be capable of labeling specific biological components for imaging. In this chapter, the progresses on developing $BaTiO_3$ nanoparticles as "Second Harmonic Radiation IMaging Probes (SHRIMPs)" for cellular imaging will be presented. The biocompatibility test of $BaTiO_3$ nanoparticles will be studied. Also, approaches for both non-specific and specific labeling of biological cells with the nanoparticles will be demonstrated. The non-specific labeling is through endocytosis of the cells and the specific labeling is through antibody conjugation. This chapter shows the critical developments of SHG nanoparticles as cellular imaging markers.

3.1 Cytocompatibility of $BaTiO_3$ nanoparticles

Cytotoxicity of nanoparticles has been a major issue in applying them for biological experiments, especially for *in vivo* experiments. For example, quantum dots have shown toxicity with inappropriate surface coating [96, 97]. In the development of $BaTiO_3$ nanoparticles as biological imaging probes, it is essential to verify the possible cytotoxicity of the nanoparticles to biological samples. It has been reported that $BaTiO_3$ nanoparticles are non-toxic to biological cells even at high concentration of the nanoparticles (100 μg/mL) [98, 99]. In this section, a standard procedure of

preparing stable water-soluble $BaTiO_3$ nanoparticles colloidal suspension in our laboratory will be presented. We then perform a cytotoxicity test on the colloidal suspension with an immortalized cell line.

We started with $BaTiO_3$ nanoparticles in dry powder form. The bare $BaTiO_3$ nanoparticle colloidal suspension is not stable in water and therefore proper surface modification for stable dispersion is required. The nanoparticles were placed in 1 M of nitric acid for 10 minutes to remove the surface barium ions. It has been reported that the barium ion leaches from the surface of the $BaTiO_3$ nanoparticle into the solution especially in an acid environment [100]. Therefore, after the treatment, we have a "TiO_2-like" particle surface. We then placed the treated particles in 10 μM of 3-aminopropyltriethoxysilane (APTES, Sigma-Aldrich) in ethanol-water-ammonia solution 75/23.5/1.5 v/v/v % at 70 ^{o}C for 8 hours. The organofunctional silanes act as a bridge between organic and inorganic phases by forming a covalent attachment of organic monolayers [101-103]. As a result, we have accessible primary amine groups immobilized on the surface of $BaTiO_3$ nanoparticles, referred to as amino-$BaTiO_3$ nanoparticles (as shown in Fig. 3-1). When the surface of the nanoparticles is functionalized by covalently attaching primary amine groups, the colloidal suspension becomes stable without strong agglomerations. The primary amine group attached to the surface of an inorganic material is also a general cross-link to bio-molecules.

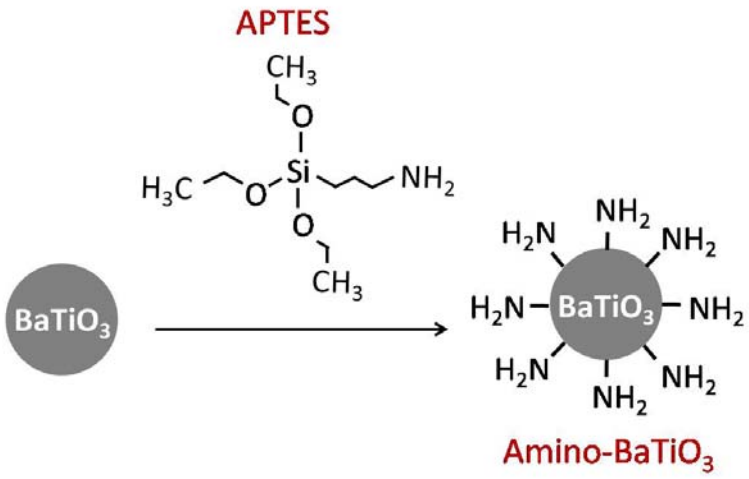

Fig. 3-1 Surface functionalization of $BaTiO_3$ nanoparticles with amino-silanes for stable water-soluble colloidal suspension

We test the cytotoxicity of the amino-$BaTiO_3$ nanoparticles by measuring the cell viability after being incubated with the nanoparticles. HeLa cells were cultured in the growth media at the concentration of ~ 6000 cells/cm^2 in 96-well polystyrene cell culture microplates (Greiner bio-one) for the test. Such cell concentration for the test is considered to be very low (less than 1 cell per 100 × 100 μm^2), and therefore the cytotoxicity measurement becomes very sensitive. Three different concentrations of the nanoparticles were added to the cell medium, which results in the overall concentrations of 10^8, 10^9, and 10^{10} nanoparticles/cm^3 in the cell medium. A control group without adding nanoparticles was also prepared. The cells were incubated with the nanoparticles at 37 °C in a humidified atmosphere of 5% CO_2 for 24 hours.

The cytotoxicity test was performed by using Alamar Blue (AbD Serotec). Alamar Blue is popular as a sensitive and versatile indicator for measuring cell proliferation and cytotoxicity [104, 105]. The oxidized, blue, nonfluorescent Alamar Blue is reduced to a pink fluorescent dye in the medium by cell activity (likely to be by oxygen consumption through metabolism). In the experiments, after the cell incubation with nanoparticles, we added 10% of commercial available Alamar Blue

into the cell medium and incubated for 4 hours. After the incubation, the fluorescent intensity of the cell medium, which reflects the cell viability, was measured by a monochromator microplate reader (Tecan, Safire2). The result is shown in Fig. 3-2. The equal fluorescent intensities between all the samples indicate that the presence of the nanoparticles does not change the cell metabolism, suggesting that the $BaTiO_3$ nanoparticles show no toxicity to the cells.

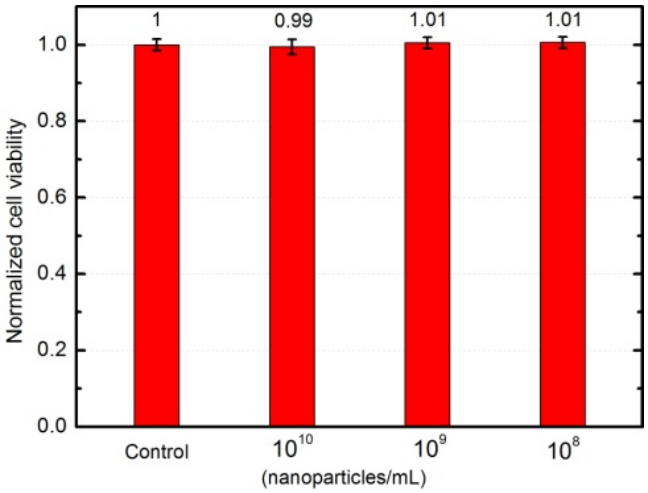

Fig. 3-2 Cell viability measurement after incubating the HeLa cells with different concentrations of the $BaTiO_3$ nanoparticles for 24 hours. The results have been normalized to the control experiment.

3.2 Nonspecific cell labeling by endocytosis

In this section, a simple and efficient way of nonspecific cell labeling with SHRIMPs is demonstrated. The nonspecific labeling of the cells with nanoparticles is performed via endocytosis of the cells. Endocytosis is the process by which cells uptake objects from outside the cells by engulfing them with their cell membrane. We incubated the $BaTiO_3$ nanoparticles with CD11b+ myeloid cells for 12 hours for the endocytosis process. After that, the excess nanoparticles were removed from the labeled cells by centrifugation. The cells were kept alive for another 16 hours before the imaging.

A standard two-photon confocal microscope (Leica, SP5) was used to image the cells labeled by the nanoparticles. The excitation light source consisted of linearly polarized femtosecond laser pulses (Coherent, Chameleon) and the excitation wavelength was centered at 812 nm wavelength. The laser was focused by a 20x 1.0 NA water-immersion microscope objective. The SHG signal was collected in epi-geometry in SHG channel (400–415 nm), and the transmission signal at the fundamental wavelength is also detected as the second channel. The results are shown in Fig. 3-3. In the transmission channel, the contrast of the cells is low (Fig. 3-3 (a)) because the cells are almost transparent. In the SHG channel, we observed a large number of nanoparticles randomly distributed inside the cells with high contrast (Fig. 3-3 (b)). We did not observe the nanoparticles internalize into the cell nucleus.

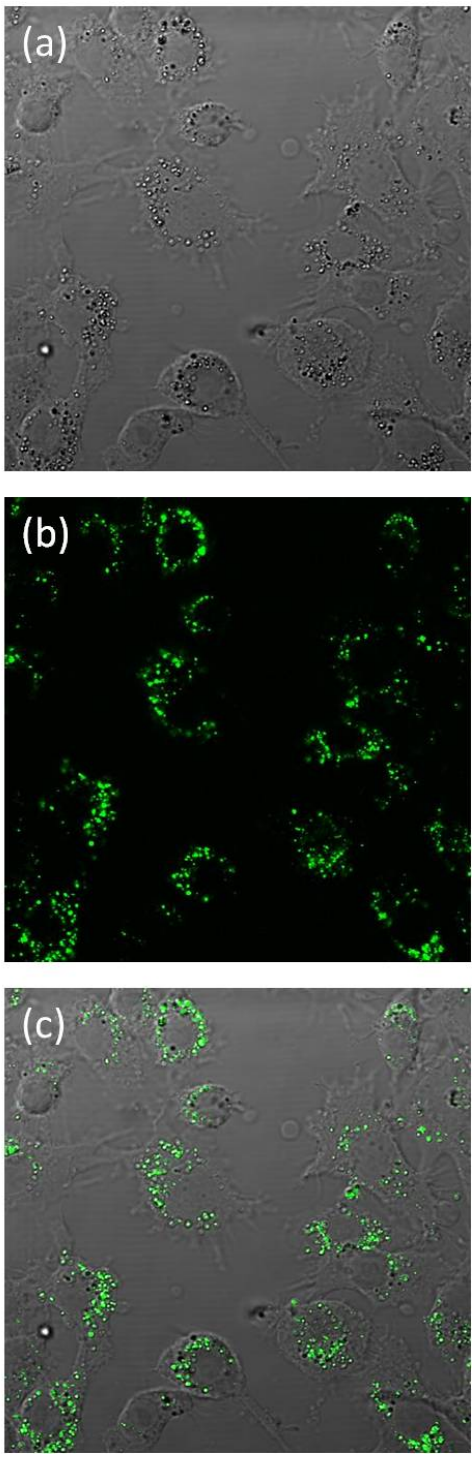

Fig. 3-3 Scanning confocal section images of the $BaTiO_3$ nanoparticles inside the myeloid cells via endocytosis. (a) Transmission channel. (b) SHG channel. (c) Merge image of (a) and (b). The size of the images is $130 \times 130\ \mu m^2$.

3.3 Surface functionalization and antibody conjugation of the nanoparticles

For most studies of biology, it is necessary for the imaging markers to be able to label the target of interest specifically. We developed a scheme for specific labeling of bio-molecules by $BaTiO_3$ nanoparticles via immunostaining. The specific labeling is achieved through an indirect staining process: the target bio-molecule is first labeled with a primary antibody which is then recognized by a secondary-antibody-nanoparticle conjugate. Such indirect staining is very convenient and flexible; one would only need to conjugate one type of secondary antibody onto the nanoparticle and be able to achieve specific labeling of various kinds of target molecules by properly choosing the primary antibody which corresponds to the secondary antibody.

Fig. 3-4 shows the processes of functionalization and antibody conjugation of $BaTiO_3$ nanoparticles. The first step towards functionalizing the SHRIMPs is to attach amine groups on the surface of the $BaTiO_3$ nanoparticles, which was presented in Section 3.1. We refer to the amine group coated $BaTiO_3$ nanoparticles as amino-$BaTiO_3$. The secondary antibody that we conjugated onto the amino-$BaTiO_3$ is a Donkey anti-Mouse IgG antibody with Cy5 fluorophores on it. The conjugation of the secondary IgG antibodies onto the amino-$BaTiO_3$ is based on the crosslinking reactions between amine and sulfhydryl groups catalyzed by maleimide. These chemical reactions have been reported for the bioconjugation of quantum dots [106].

3.3.1 Materials

$BaTiO_3$ nanoparticles in dry powder were commercially available from TechPowder (TechPowder S.A. Lausanne, Switzerland). The secondary antibody was a Donkey anti-Mouse IgG antibody-Cy5 (Jackson ImmunoResearch). Sulfosuccinimidyl 4-[N-

maleimidomethyl]cyclohexane-1-carboxylate (sulfo-SMCC) was obtained from Thermo Scientific. Ethylenediaminetetraacetic acid (EDTA, > 99.99%), 2-mercaptoethanol (> 98%), DL-dithiothreitol (DTT, 1M), bovine serum albumin (BSA, > 98%), and Tween 20 were purchased from Sigma-Aldrich. 2-(N-morpholino)ethanesulfonic acid (MES, 0.5 M) was purchased from Biochemika Ultra. The exchange buffer was composed of 50 mM of MES and 2 mM of EDTA in distilled water pH 7. Phosphate-buffered saline solution (PBS pH 7.4) was obtained from Invitrogen.

3.3.2 Protocol of antibody conjugation

The protocol of conjugating secondary antibody onto amino-$BaTiO_3$ was as follows: First, we mixed 300 μL of the amino-$BaTiO_3$ solution (5×10^{11} particles/mL in pH 8 NaOH in distilled water) with 200 μL of 22.9 mM sulfo-SMCC at room temperature for 1 hour. The amine groups on the SHRIMPs reacted with the sulfo-SMCC to yield maleimide-activated SHRIMPs. Meanwhile, 300 μL of the secondary IgG antibody at 1 mg/mL was mixed with 6 μL of 1M DTT at room temperature for 30 minutes. The hinge disulfide bonds on the IgG antibodies were reduced by DTT to yield free sulfhydryl groups. The maleimide-activated SHRIMPs and the reduced antibodies were buffer exchanged by flowing through the desalting columns (NAP-5, GE Healthcare) pre-equilibrated with the exchange buffer (see previous Materials section for the solvent composition).

The maleimide-activated SHRIMPs and the reduced antibodies were then mixed together at room temperature for 1 hour. The secondary-antibody-SHRIMP conjugates (2nd-Ab-SHRIMPs) formed when the reduced antibodies covalently coupled to the SHRIMPs through the reaction between the maleimide groups and the

free sulfhydryl groups. The conjugation process was then quenched by adding 10 μL of 10 mM 2-mercaptoethanol at room temperature for 30 minutes. Finally the 2nd-Ab-SHRIMPs were separated from the unconjugated reduced secondary antibodies by using a separation column (Superdex 200, GE Healthcare). The 2nd-Ab-SHRIMPs were stabilized in phosphate-buffered salines (PBS, pH 7.4) with 10 mg/ml BSA and 0.1% v/v Tween 20.

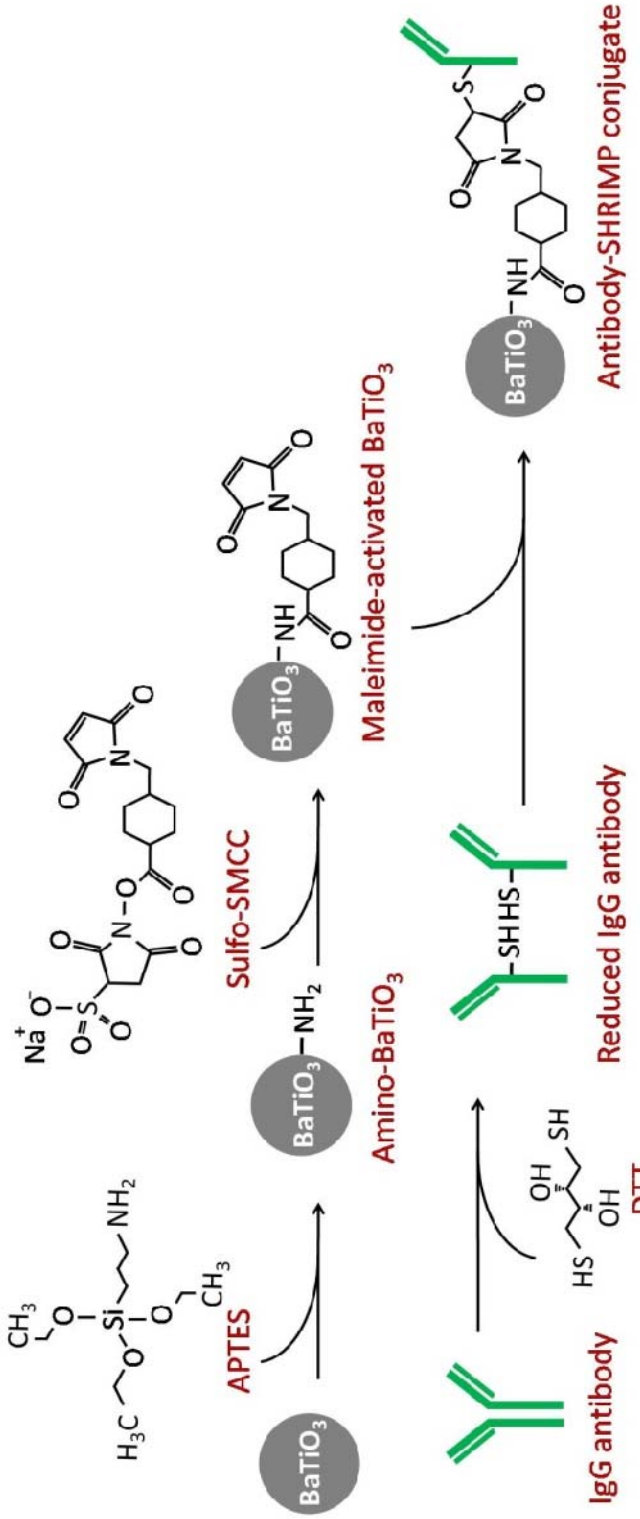

Fig. 3-4 Scheme of covalent bioconjugation of IgG antibody onto the surface of $BaTiO_3$ nanoparticle for specific labeling imaging application

3.4 Specific labeling in an antibody microarray

We verified the effectiveness of specific labeling of the 2nd-Ab-SHRIMPs with a microarray of primary antibodies. Three different types of the primary antibodies and also the buffer solution were printed separately and repeatedly on the slide in the form of a microarray. The three types of the primary antibodies were Mouse anti-Human IgG (CD144, VE-caderin, BD Biosciences), Goat anti-Human IgG (Jackson ImmunoResearch), and Rabbit anti-Human IgG (Jackson ImmunoResearch). The Mouse anti-Human IgG was the target primary antibody because the secondary antibody was an anti-Mouse IgG. The primary antibodies were printed on the aldehydesilane coated slides (Nexterion Slide AL, Schott Nexterion) by a contact-printing robotic microarrayer (OmniGrid 300, Genomic Solutions) equipped with SMP2 pins (TeleChem International) at 22°C with 60% relative humidity. The spotting buffer solution was PBS with 5% glycerol, and the concentration of the primary antibody was 0.2 mg/mL. The size of the printing spot is 90 μm in diameter and the period between two adjacent spots is 200 μm. After printed, the slides were incubated for an hour at 22°C at 75% relative humidity. During the incubation, the proteins cross-linked to the slide. Then the free aldehyde groups on the slides were blocked by 50 mM triethanolamine (titrated to pH 8 with boric acid) for 30 minutes at room temperature. The slide was rinsed by water and then dried by centrifugation.

Before testing the 2nd-Ab-SHRIMPs, the specific labeling of the secondary anti-Mouse IgG antibody itself (Donkey anti-Mouse IgG antibody-Cy5, Jackson ImmunoResearch) to the target primary antibody was verified with the microarray of the primary antibodies. The microarray was first blocked with PBS with 3 % v/v

Gelatin and 0.1 % v/v Tween 20 for 30 minutes at room temperature. Then the microarray was incubated with the secondary antibody-Cy5 at the concentration of 20 ng/mL for 45 minutes at room temperature. Finally the microarray was rinsed with PBS to remove the excess unconjugated secondary antibodies.

The microarray was imaged by a laser-scanning microscope (Agilent DNA microarray scanner, Agilent Technologies) and the single-photon fluorescence signal from the Cy5 on the secondary antibody was detected. Fig. 3-5 is the fluorescent image of the microarray. The locations of the printed primary antibodies and the buffer solution are shown with dashed circles. Each sample was printed four times in the field of view of Fig. 3-5. Four clear spots in a row indicate a high concentration of the secondary antibody were present at the locations where the target primary antibody was printed. All negative controls show very little fluorescent signal. The ratio of the integrated fluorescent intensity between the target antibody and the negative controls is 1: 0.01: 0.03: 0.005 (Mouse IgG: Goat IgG: Rabbit IgG: Buffer Solution). Therefore, the secondary antibody itself was verified to be highly specific to the target primary antibody.

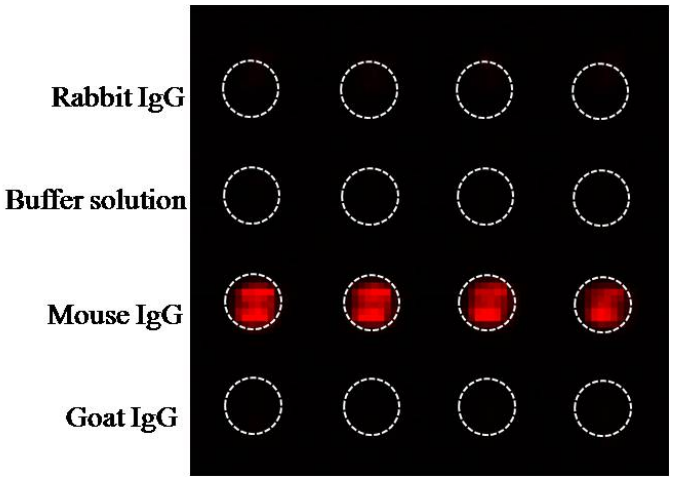

Fig. 3-5 The fluorescent microscopic image of the primary-antibody microarray labeled by the secondary antibody-Cy5

To label the target primary antibodies on the microarray with the 2nd-Ab-SHRIMPs, we first blocked the microarray with PBS with 3% v/v Gelatin and 0.1% v/v Tween 20 for 1 hour at room temperature to reduce the nonspecific labeling. Then the microarray was incubated with the 2nd-Ab-SHRIMPs at the concentration of 10^{10} particles/mL for 2 hours at room temperature. Finally the microarray was rinsed with PBS to remove the excess unbound 2nd-Ab-SHRIMPs. The sample was kept wet for imaging with a scanning confocal microscope (Leica, SP5).

Fig. 3-6 is the microscopic SHG image of the microarray labeled by the 2nd-Ab-SHRIMPs and the corresponding quantitative analysis. The locations of the printed primary antibodies and the buffer solution are shown with dashed circles. Four clear bright spots in a row can be seen in Fig. 3-6, which indicates a high concentration of the 2nd-Ab-SHRIMPs was present at the locations where the target primary antibody (Mouse anti-Human IgG) was printed. All negative controls show very little SHG signal. From Fig. 3-6, the ratio of the integrated SHG intensity, reflecting the ratio of the number of SHRIMPs, between the target antibody and the negative controls is measured as 1: 0.03: 0.03: 0.05 (Mouse IgG: Goat IgG: Rabbit IgG: Buffer Solution). The standard deviation of the four spots of each sample is shown as the error bar plotted in Fig. 3-7. Therefore, the 2nd-Ab-SHRIMPs showed a highly specific labeling on the primary-antibody microarray.

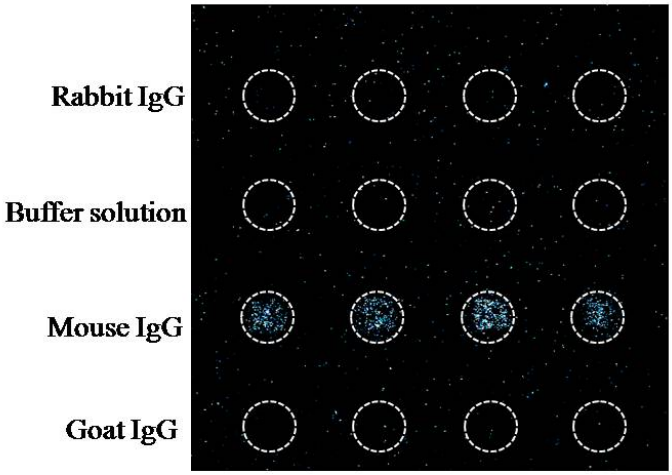

Fig. 3-6 SHG microscopic image of the primary-antibody microarray labeled by the 2nd-Ab-SHRIMPs. The dashed circles show the locations where the target primary antibody, two other primary antibodies for negative control, and the buffer solution were printed. Each of the samples was printed four times in a row in the field of view of this figure. The printing spot size is 90 μm in diameter and the period between the adjacent spots is 200 μm. A high concentration of SHRIMPs can be observed at the locations of the target primary antibodies, showing a highly specific labeling of the 2nd-Ab-SHRIMPs.

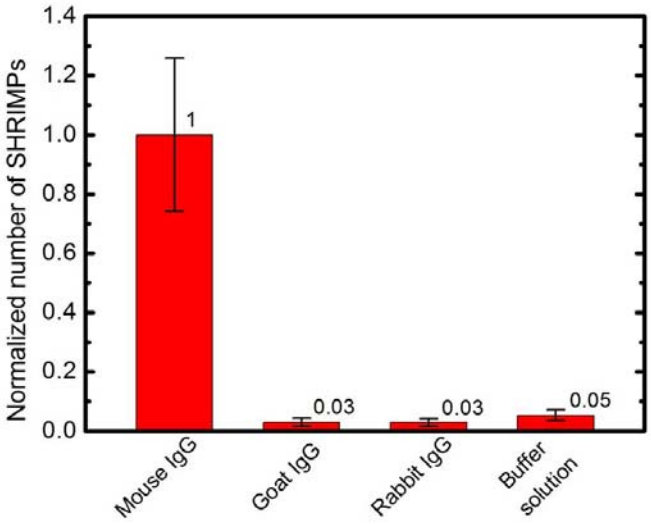

Fig. 3-7 Quantitative analysis of Fig. 3-6. The ratio of the number of SHRIMPs presenting at the four samples was 1: 0.03: 0.03: 0.05 (Mouse IgG: Goat IgG: Rabbit IgG: Buffer Solution), measured from the integrated SHG intensity. The error bar shows the standard deviation of the four spots of each sample.

3.5 Specific cell membrane protein labeling via immunostaining

We further examined the specific labeling of SHRIMPs in a biological cell environment. The human leukocyte antigen (HLA) class I molecule is critical to immune system function in humans because it represents antigenic peptides to T cells. We demonstrated the specific targeting of the HLA class I molecule presented on the HeLa cell surface with $BaTiO_3$ nanoparticles.

The HeLa cells were immunostained in suspension with the primary antibody specific to human HLA class I antigens followed by the labeling of 2nd-Ab-SHRIMPs. HeLa cell line was provided by the Biomolecular Screening Facility at EPFL, Switzerland. The HeLa cells were grown in flasks containing the growth media (DMEM supplemented with 10% heat-inactivated FBS) at 37°C in a humidified atmosphere of 5% CO_2. The HeLa cells were harvested from the flask by applying Trypsin for 4 minutes at 37°C. We counted and prepared 10^6 of cells for each immunostaining. The cells were washed and suspended in 2 mg/mL of BSA in PBS. We blocked the cells with 2 mg/mL of BSA in PBS for 1 hour at room temperature to reduce the nonspecific labeling. The primary antibody (Mouse monoclonal antibody specific to human HLA class I antigens) was introduced at a dilution of 1:100 and incubated with the cells for 1 hour at room temperature. The cells were then washed three times with 2 mg/mL of BSA in PBS by centrifugation to remove the unconjugated primary antibodies. The primary-antibody-labeled cells were then mixed with the secondary-antibody-SHRIMP conjugates at a concentration of about 10^9 nanoparticles/mL at room temperature for 1 hour. The cells were then washed three times with 2 mg/mL of BSA in PBS. Finally the cells were placed in a petri dish

filled with growth media to allow the cell to attach for imaging. The cells were further stained with Calcein AM (Invitrogen) for fluorescent imaging. For comparison, we prepared a control sample where HeLa cells were not stained by the primary antibody under otherwise identical conditions. The cells were prepared in a petri dish and kept alive during the imaging.

The cells were imaged with a scanning confocal microscope (Leica, SP5) under the excitation of femtosecond laser pulses (Coherent, Chameleon) at 812 nm wavelength. Two independent channels, i.e., SHG channel (400–415 nm) and fluorescent channel (500–550 nm) collected the signal in epi-geometry, and a transmission channel collected the fundamental signal in the forward direction. The SHG signal was from the SHRIMPs, and the fluorescent signal was from the Calcein used to stain the cells.

Fig. 3-8 (a)–(d) show the section images of the cells labeled with 2nd-Ab-SHRIMPs. From these images, we observe a great number of 2nd-Ab-SHRIMPs attached on the cell surface. The SHRIMPs have a great contrast in biological cell environment since the endogenous SHG from the cell components is weak. It is worth noting that SHRIMPs emit SHG signal equally in the forward and backward directions, so the epi-geometry is efficient for signal collection. For comparison, Fig. 3-8 (e)–(h) show the section images of the HeLa cells in the control sample where almost no 2nd-Ab-SHRIMP is observed on the cell surface. It indicates that the labeling of 2nd-Ab-SHRIMPs on the cell membrane in Fig. 3-8 (a)–(d) is specific to the primary antibody.

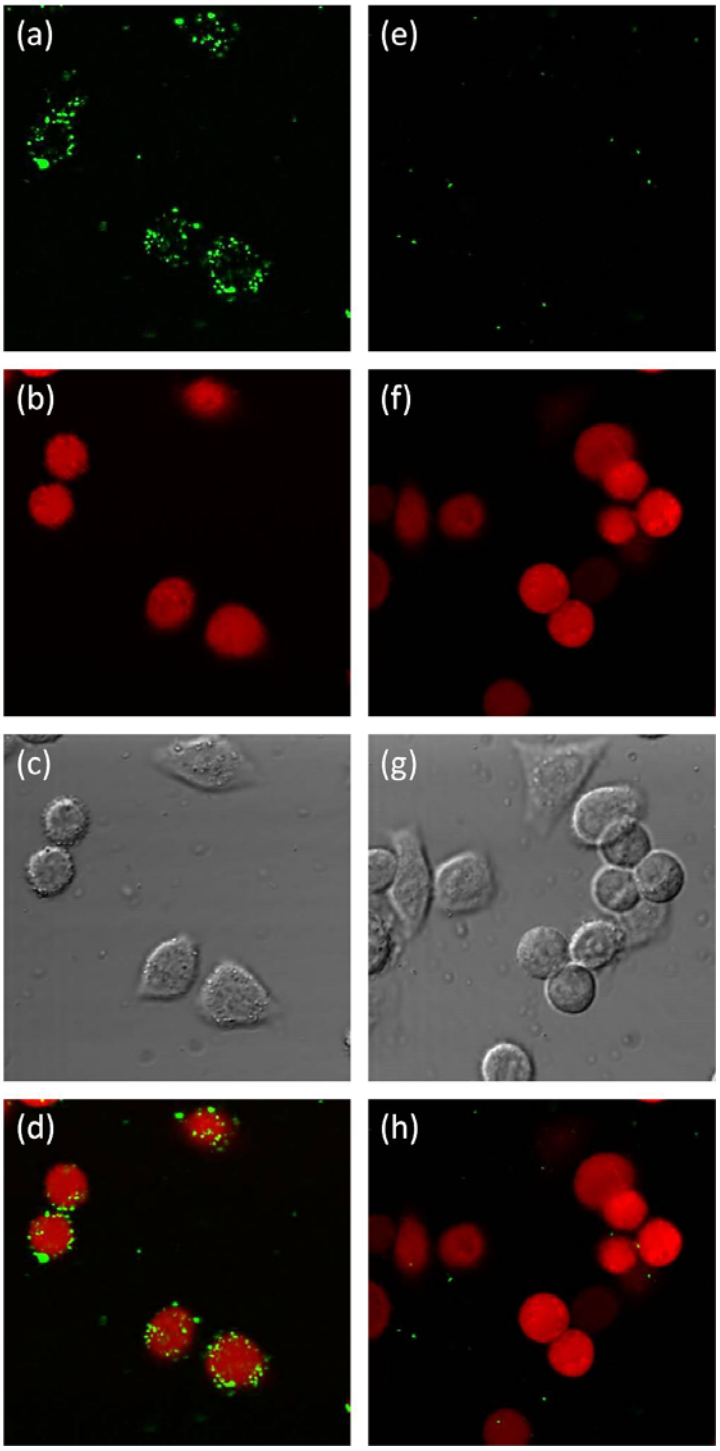

Fig. 3-8 Confocal section images of HeLa cells labeled with the 2nd-Ab-SHRIMPs. (a)–(d) The cells were first labeled with the primary antibody specific to the HLA class I molecules present on the cell membrane and then labeled with the 2nd-Ab-SHRIMPs; (e)–(h) The control sample where the cells were not labeled with primary antibody but under otherwise identical conditions; SHG images are shown in green in (a) and (e); two-photon fluorescence images are shown in red in (b) and (f); transmission images are shown in (c) and (g); and the merged images of SHG images and fluorescence images are shown in (d) and (h). The size of the images is $105\times105\ \mu m^2$.

Chapter 4 3D imaging of SHG nanoparticles

Tracing specific biological components or molecules in a 3D environment is extremely useful and sometimes necessary in the study of biology. Since 3D image sensors do not exist, conventional 3D imaging is done by mechanical scanning, in which a lower dimensional sensor is used to represent a higher dimensional world. For example, confocal scanning microscopes achieve 3D imaging by raster-scanning a tight focus across the 3D sample volume. 3D imaging via scanning is only valid when the specimen is relatively stationary within the time required for scanning. Otherwise, the temporal domain will inevitably interfere with the 3D spatial domain. As many living biological organisms are highly dynamic, 3D imaging via scanning is not capable of capturing distortionless time-lapse 3D images. Therefore, a scan-free 3D imaging technique is desirable. In this chapter, we demonstrate 3D imaging of SHG nanoparticles by two approaches—conventional 3D scanning microscope and a novel scan-free 3D imaging. Scan-free 3D imaging is achieved by exploiting the coherent nature of the SHG signal radiated from the nanoparticles. The complex two-dimensional (2D) SHG signal (amplitude and phase) can be recorded in a digital interferogram without scanning. Then, by digital reconstruction, a 3D distribution of the signal field, reflecting the 3D distribution of the nanoparticles, can be obtained.

4.1 SHG 3D scanning microscopy

In this section, 3D scanning imaging of SHG nanoparticles in biological samples *in vitro* and *in vivo* will be demonstrated by using a commercial confocal microscope (Leica, SP5). The excitation light source is a Ti:sapphire oscillator (Chameleon Ultra

II, Coherent) generating 140 fs laser pulses at 812 nm wavelength and 80 MHz repetition rate. The average excitation power is approximately 15 mW. The excitation is tightly focused by a high-NA water-immersion objective and two-photon fluorescence and SHG signal are generated within the focus. The quadratic dependency of the signal to the excitation power provides the optical sectioning capability in the axial direction [28, 29]. The two-photon fluorescence and SHG signal are collected by the same objective in an epi-geometry, and these two signals are separated by a dichroic mirror and simultaneously detected by two independent photomultipliers (R6357, Hamamatsu). The ambient light was rejected by a narrow bandpass optical filter corresponding to the signal wavelength and bandwidth.

4.1.1 *In vitro* cell imaging

We use the confocal scanning microscope to image HeLa cells with SHG nanoparticles. The microscope objective is a 63X NA1.2 water-immersion objective. HeLa cells were incubated for 24 hours at 37^{o}C with 30 nm $BaTiO_3$ particles that have been stabilized with aminomethylphosphonic acid. During the incubation, the cells uptake nanoparticles through endocytosis [107]. The nanoparticles were engulfed nonspecifically into vesicles and packed as clusters randomly by the cells. A 3D distribution of nanoparticles was formed inside the cells. The cells were further stained with Calcein AM (Invitrogen) for two-photon fluorescent imaging. We washed away the unbound nanoparticles with buffer solution (phosphate buffered saline, PBS) and fixed the cells with 3.7% parafolmaldehyde.

3D imaging is performed by scanning the focus point-by-point within the volume of interest. At each depth of the sample, a 512 × 512 pixel section image is recorded at a raster-scanning speed of 100 Hz. 78 section images are captured with a 0.2-μm-

depth increment to form a 3D data cube. It takes 400 seconds to scan the focus across this volume. In Fig. 4-1, we show 10 successive section images of a HeLa cell with SHG nanoparticles, from the top to the bottom, with a 1 μm axial increment between images. The section capability relies on the quadratic dependency of the signal to the excitation intensity, as the pinhole of the microscope is completely open. The two-photon fluorescence signal collected from the spectral window of 440–700 nm is shown in red, and the SHG signal collected from the spectral window of 390–410 nm is shown in green. The cell is uniformly stained by Calcein dye, so the red shows the shape of the cell. The green dots show the locations of the nanoparticles which have great contrast within the cell. For better visualization of the 3D localization of the nanoparticles inside the cell, the cross-section views of the cell are shown in Fig. 4-2, which also confirms that the nanoparticles entered the cells by endocytosis. The voxel size for the scanning is set as 105 nm in lateral and 200 nm in axial.

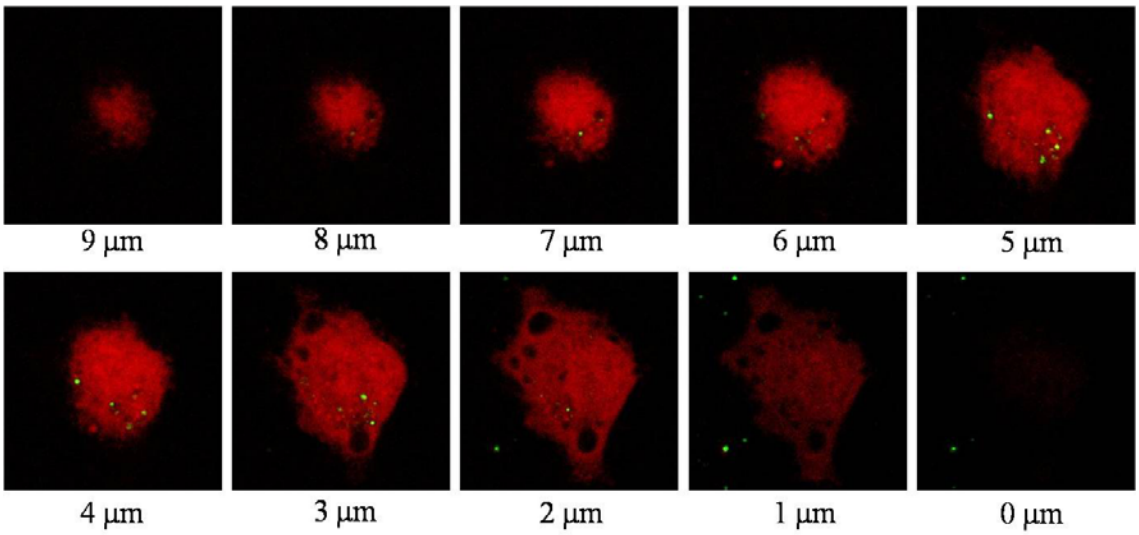

Fig. 4-1 Confocal section series of a calcein-stained HeLa cell (in red) with SHG nanoparticles (in green) inside it at successive depths (indicated below the images), from the top to the bottom of the cell. The size of the images is $30 \times 30\ \mu m^2$.

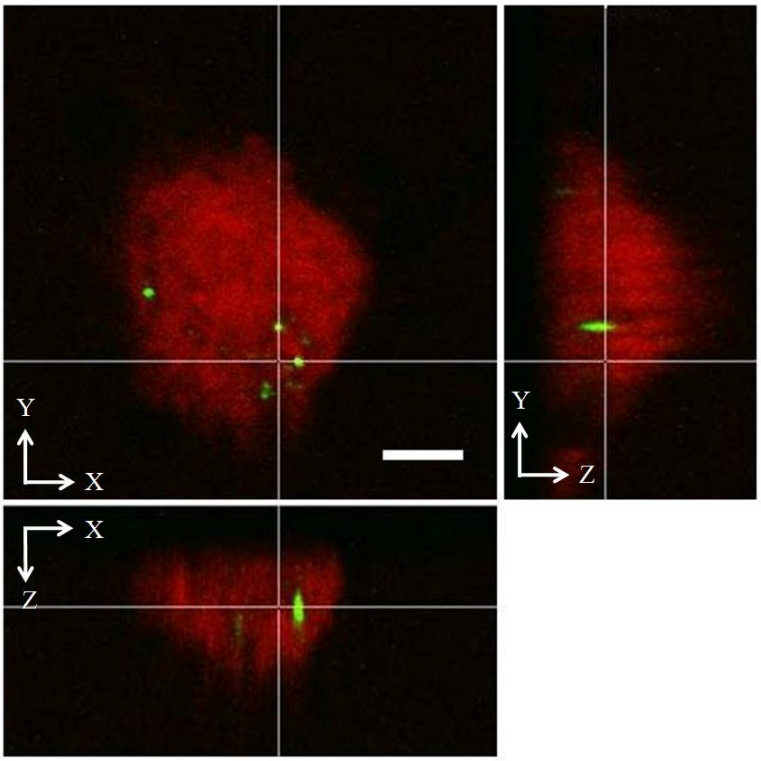

Fig. 4-2 Confocal section images of a calcein-stained HeLa cell (in red) with SHG nanoparticles (in green) inside it. 3D localization of the nanoparticles inside the cell is clearly observed. The scale bar is 5 μm.

4.1.2 *In vivo* mouse imaging

In this sub-section, we show the preliminary results of using SHG nanoparticles as *in vivo* imaging probes. The sample under analysis is SHG nanoparticles injected into the tail of a living mouse. In the *in vivo* experiment, we anesthetized the mouse and injected (5–10 μL) a colloidal suspension of $BaTiO_3$ nanoparticles (15 mg/mL) in distilled water into the tail of the living mouse. The mouse was then placed under the microscope objective with the tail immersed in water for imaging. The microscope objective in the experiment is a 20X 1.0-NA water-immersion microscope objective. A great number of the nanoparticles were observed at the injection site. Interestingly, we also observed isolated nanoparticles around 300 μm away from the injection site at the depth of about 100 μm.

Fig. 4-3 shows a photograph of the experiment and the results. In Fig. 4-3 (b)(c), the SHG section and cross-section images show clearly that two isolated SHG nanoparticles are located in the mouse tail at 100 μm deep. The nanoparticles have great contrast against the environment. The ratio between the SHG intensity of the nanoparticle to the SHG background in the section image is measured to be around 10. The SHG background is from the endogenous SHG of the tissue. In the cross-section image, the endogenous SHG from the muscles at the surface of the tail (~ 50 μm thick) can be clearly observed. Meanwhile, the SHG from the nanoparticles at 100-μm deep is also clearly resolved. Notice that the cross-section images of the two nanoparticles are slightly distorted due to the scattering of the tissue. It is worth noting that the SHG nanoparticles provide sufficient SHG contrast to the endogenous SHG. As the endogenous SHG from muscles and collagens is mostly in the forward direction due to the phase matching of SHG signal, the SHG emission from the nanoparticles is more isotropic due to the small size of the SHRIMPs. As a result, the epi-detection helps us to observe the signal from the nanoparticles along with the signal from the large-sized biological structures.

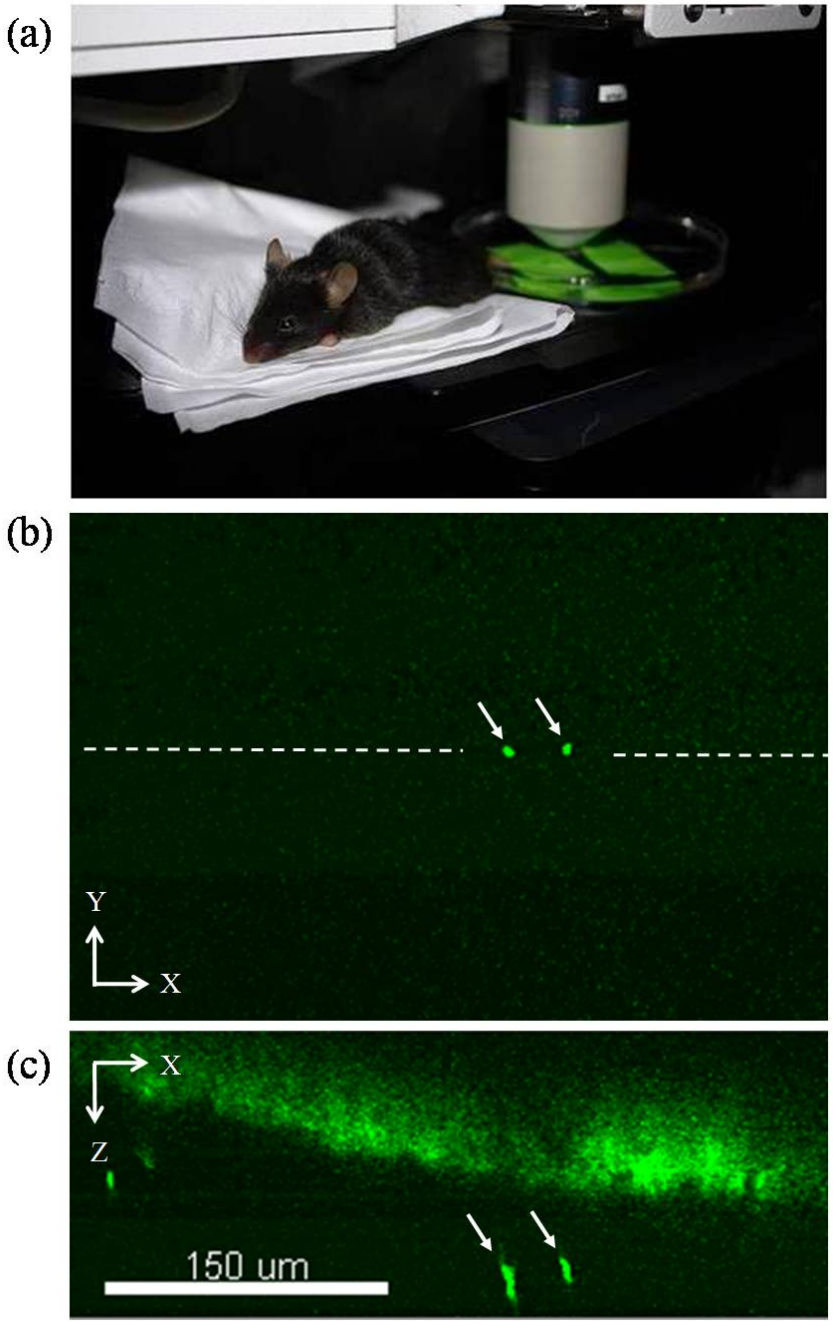

Fig. 4-3 *In vivo* SHG imaging of the nanoparticles in a living mouse tail. (a) The photograph of the experimental scenario. (b) The SHG section image (XY plane) at 100 μm deep in the mouse tail where two isolated nanoparticles can be seen. (c) The SHG cross-section image (XZ plane) of the sample along the dashed line in (b), in which both the endogenous SHG from the muscles on the surface of the tail and also the two nanoparticles inside the tail are clearly observed

4.2 Scan-free 3D holographic microscopy

In this section, we review the state-of-art techniques of linear and nonlinear holographic microscopy where 3D imaging can be achieved without scanning. Holography is a powerful technique that is able to record a complex signal field quantitatively by interferometric means and then reconstruct the signal field later [108–111]. In linear holography, the signal field is usually the scattered light from an object under the illumination of a coherent light source. The signal field is then recorded by using a coherent reference beam where the interference pattern (hologram) between the signal and the reference is captured. Thanks to the advancements in charge-coupled devices (CCD), the hologram can be recorded digitally with a CCD camera, referred to as digital holography [110, 111]. Nowadays, highly sensitive and low noise CCD cameras with gain in the signal are commercially available, which greatly improves the efficiency and quality of holography. In digital holography, the reconstruction can be performed by digital back-propagation [111–113]. Since a 3D field distribution can be reconstructed from a 2D hologram by back-propagation, holography has been recognized as a 3D imaging technique without scanning [112]. Besides the 3D imaging capability, holography also offers better signal-to-noise ratio (SNR) due to the carrier frequency provided by the reference beam [69].

Recently, the concept of nonlinear holography has been proposed and demonstrated [61, 69, 70, 114–118]. In contrast to linear holography, in which the signal field is at the same optical frequency as the illumination, the signal of nonlinear holography undergoes a coherent nonlinear optical process and therefore the optical frequency of the signal is different from the illumination. Such coherent nonlinear

process includes SHG [61, 69, 70, 116–118], sum-frequency generation (SFG), third-harmonic generation (THG), and coherent anti-Stokes Raman scattering (CARS) [114, 115]. Since the nonlinear process is coherent, one can record the nonlinear signal by holography with a coherent reference beam at the same optical frequency.

In our laboratory, we have proposed and demonstrated a harmonic holographic (H^2) microscope using SHG from nanoparticles as the signal [69]. As described in previous chapters, SHG nanoparticles radiate SHG signal efficiently as point sources under excitation. H^2 is able to capture the complex SHG field radiated from the nanoparticles by digital holography. In the reconstruction, 3D field distribution, reflecting 3D nanoparticle distributions can be visualized. H^2 allows fast 3D imaging of SHG nanoparticles due to the high imaging contrast provided by detecting the signal at SHG frequency: the background signal (linear background scattering and photoluminescence) can be efficiently removed.

As the goal is to image the SHG field radiated from the nanoparticles by digital holography, some important technical issues should be addressed. First, since the nanoparticles are small in size compared to the optical wavelength, one should push the resolution of the optical system to the diffraction of light. In digital holography, the signal field is recorded by a digital camera whose pixel pitch is usually a few microns. The digital camera can only capture spatial frequency up to $K_{max} = 2\pi/\Lambda$ in a single hologram where Λ is the pixel pitch. Since Λ is much larger than the wavelength of visible light, lots of signal field of high spatial frequency will be lost during the holographic recording. To recover the high spatial frequency, we use a 4F imaging system, consisting of a high NA microscope objective and a 20 cm lens, to optically magnify the signal field before the holographic recording. The spatial

frequency of the optical field becomes lower after the magnification and therefore it can be captured by the camera.

Furthermore, to record the SHG signal field, a coherent reference beam at SHG frequency is required. We use a separate frequency doubling crystal in the reference beam to generate a coherent linearly polarized SHG reference beam. Therefore, in our holographic recording, only the signal field at the same SHG polarization as the reference beam will be captured. This is generally not a problem in imaging SHG nanoparticles because the SHG field radiated from nanoparticles has all polarizations based on the second-order nonlinearity tensor [56]. As a result, the linearly polarized reference beam always records sufficient signal field for 3D holographic imaging of nanoparticles.

4.3 Off-axis and on-axis digital holography

Two types of H^2 have been performed in our laboratory: off-axis and on-axis holography, distinguished by the angle between the reference beam and the signal beam. In this section, the theory of holographic recording and reconstruction will be described. Let's start with off-axis holography. As discussed above, we magnify the SHG signal field by a 4F imaging system to lower the spatial frequency. After the magnification, the SHG signal field that arrives on the CCD camera satisfies the paraxial approximation. Therefore, it is valid to denote the magnified SHG signal field at the 4F imaging plane as $S(x,y)e^{ikz}$ at $z = 0$ as shown in Fig. 4-4, where $k = 2\pi/\lambda$, λ is the optical wavelength. The signal field propagates for a distance of z_0 and it arrives at the CCD camera. The field at $z = z_0$ can be written as

$$[S(x,y) \otimes h_{z_0}(x,y)]e^{ikz_0}\ , \tag{4-1}$$

where $h_{z_0}(x,y)$ is the Fresnel convolution kernel as

$$h_{z_0}(x,y) = \frac{\exp(ikz_0)}{i\lambda z_0} \exp\left[\frac{ik}{2z_0}(x^2+y^2)\right]. \tag{4-2}$$

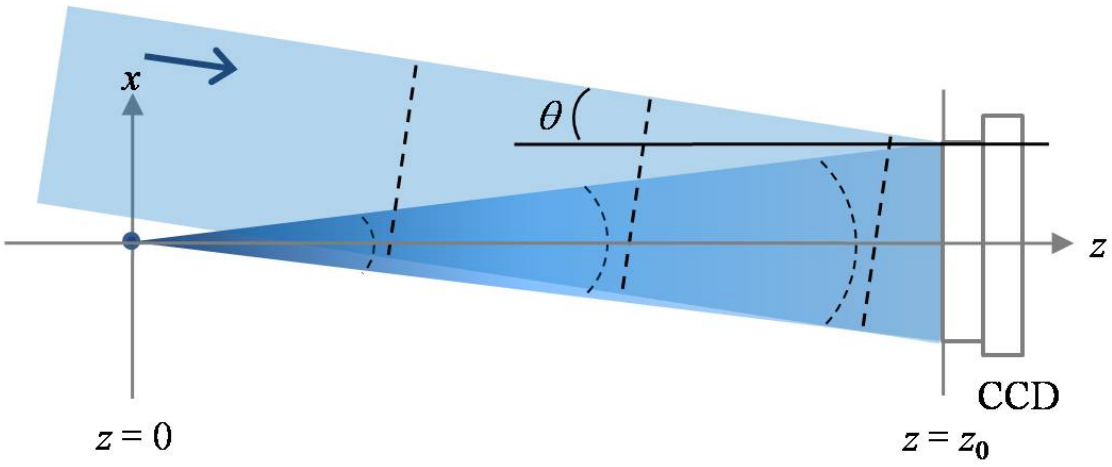

Fig. 4-4 Off-axis holographic imaging system

In off-axis holography, the reference beam is a plane-wave incident in a small angle θ with respect to the optical axis of the system as shown in Fig. 4-4. We denote the reference beam at $z = z_0$ as

$$R(x,y) = R_0 e^{-ik_{x0}x} e^{ik_{z0}z_0}, \tag{4-3}$$

where R_0 is a real value representing the field amplitude, and $k_{x0} = ksin\theta$, $k_{z0} = kcos\theta$. The intensity detected on the CCD camera is the hologram $H(x,y)$ which is the interference between the signal and the reference, and it can be written as

$$H(x,y) = \left|[S(x,y) \otimes h_{z_0}(x,y)]e^{ikz_0} + R_0 e^{-ik_{x0}x} \cdot e^{ik_{z0}z_0}\right|^2 \tag{4-4}$$

which can be further expanded as

$$\begin{aligned} H(x,y) = & \\ & \left|S(x,y) \otimes h_{z_0}(x,y)\right|^2 + {R_0}^2 + R_0 e^{ik_{x0}x}[S(x,y) \otimes h_{z_0}(x,y)]e^{i(k-k_{z0})z_0} + \\ & R_0 e^{-ik_{x0}x}[S(x,y) \otimes h_{z_0}(x,y)]^* e^{-i(k-k_{z0})z_0}. \end{aligned} \tag{4-5}$$

The first two terms in equation (4-5) are the non-interferometric background and the third and the fourth terms are the interference between the signal and the reference. It should be noticed that in H^2, a femtosecond laser is used for excitation of the nanoparticles and also for generating the coherent reference beam. Therefore, both the signal and the reference consist of femtosecond laser pulses. To obtain the interference between the two on the CCD camera, the two pulses need to be overlapped temporally. This can be done by using a motorized delay stage in the reference beam. In the measurement, we take advantage of the short coherent length (45 μm for 150 fs laser pulses) to remove the non-interferometric background.

Specifically, we take a background image by mismatching the two pulses temporally on the CCD camera before recording the hologram. The background image only contains the first two terms in equation (4-5) where the fluctuation is usually dominated by the imperfectness of the reference beam. Then, we overlap the two pulses and a hologram is recorded. By subtracting the background image from the recorded hologram, a processed hologram $H_p(x,y)$ containing only the interference terms (i.e., the third and the fourth terms in equation (4-5)) can be obtained. The processed hologram also allows us to use the available spatial bandwidth more efficiently as the non-interferometric terms at low spatial frequency are removed.

To reconstruct the signal field $S(x,y)$ from $H_p(x,y)$, we perform a 2D discrete Fourier transform to $H_p(x,y)$, obtaining $FT\{H_p(x,y)\}$ which can be expressed as

$$FT\{H_p(x,y)\} = S_F(k_x - k_{x0}, k_y) + {S_F}^*(-k_x + k_{x0}, -k_y), \tag{4-6}$$

where $S_F(k_x, k_y)$ is the 2D Fourier transform of $R_0[S(x,y) \otimes h_{z_0}(x,y)]e^{i(k-k_{z0})z_0}$. As shown in equation (4-6), the spectra of the two terms are separated by $2k_{x0}$ in spatial frequency domain, which allows us to handle them individually when there is no overlap between the two spectra. Therefore, we can readily obtain $S_F(k_x, k_y)$ which allows us to reconstruct the complex signal field. The reconstructed signal field $S_{R,off-axis}(x,y)$ can be found by inverse Fourier transform and back-propagation as

$$S_{R,off-axis}(x,y) \propto FT^{-1}\{S_F(k_x, k_y)\} \otimes h_{-z_0}(x,y). \tag{4-7}$$

On-axis holography is a special case of off-axis holography in which the reference beam is incident at an angle $\theta = 0$ as shown in Fig. 4-5. Therefore, the two spectra in equation (4-6) are overlapped since $k_{x0} = 0$. We perform the reconstruction from the processed hologram $H_p(x,y)$ which is now written as

$$H_p(x,y)\big|_{k_{x0}=0} = R_0[S(x,y)\otimes h_{z_0}(x,y)]e^{i(k-k_{z0})z_0} + c.c. \qquad (4\text{-}8)$$

where $c.c.$ means the complex conjugate. It can be further simplified by assigning a complex value $A = R_0 e^{i(k-k_{z0})z_0}$. We have

$$H_p(x,y)\big|_{k_{x0}=0} = A[S(x,y)\otimes h_{z_0}(x,y)] + c.c. \qquad (4\text{-}9)$$

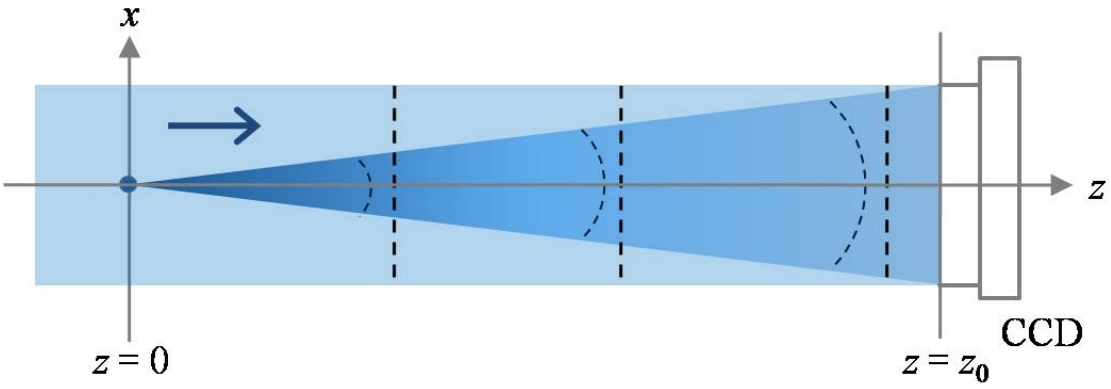

Fig. 4-5 On-axis holographic imaging system

In the reconstruction, we perform back-propagation directly to $H_p(x,y)$. The reconstructed signal field becomes,

$$S_{R,on-axis}(x,y) = H_p(x,y)\big|_{k_{x0}=0} \otimes h_{-z_0}(x,y)$$

$$= AS(x,y) + A^*S^*(x,y)\otimes h_{-2z_0}(x,y). \qquad (4\text{-}10)$$

In equation (4-10), the first term is the reconstructed signal field while the second term is its twin image at a distance of $2z_0$. There have been studies on removing the twin image by iterative algorithms. The inherent twin image will have little effect on the reconstructed field when z_0 is large. In the demonstration shown later in this chapter, the z_0 is 20 cm and the effect of the twin image is negligible.

4.4 Harmonic holographic (H^2) microscopy

We built a H^2 microscope for scan-free 3D imaging of SHG nanoparticles. In this section, the experimental setup of a H^2 microscope will be presented. The point spread function showing the spatial resolution of the imaging system will be examined by imaging a single SHG nanoparticle. We demonstrate the 3D imaging capability of the H^2 microscope with randomly distributed SHG nanoparticles in an artificial sample and also a biological cell.

4.4.1 Experimental setup

The experimental setup of a H^2 microscope is shown in Fig. 4-6. The excitation laser is a linearly polarized Ti:sapphire oscillator (150 fs pulse duration centered at 800 nm wavelength with a 76 MHz repetition rate). The peak intensity of the excitation is 1.5 GW/cm^2, which is 100 times less than the cell damage threshold [119]. As was explained in the previous sections, the H^2 microscope can be understood as a 4F imaging system followed by a holographic recording system. The SHG signal from nanoparticles is collected and optically magnified by a 4F system consisting of a microscope objective and a lens of 20 cm focal length. Two microscope objectives have been used in our experiments; one is 1.4-NA oil-immersion objective, and the other is 0.9-NA air objective, providing optical magnifications of 140 and 80, respectively. An EMCCD (Andor iXonEM+ 885) is used as the detector. Narrow bandpass filters centered at SHG wavelength are used to remove the excitation. The EMCCD is placed away from the 4F imaging plane so that the object field can propagate and fill the detection area of EMCCD. The hologram recording distance, i.e., the distance between the SHG image formed by the 4F system and the EMCCD, is 20 cm. A plane wave at doubled frequency generated by a separate β-barium borate

(BBO) crystal served as the reference beam. The intensity ratio between the signal maximum and the reference beam is set to be 1:10. The signal and reference pulses were collinearly overlapping both spatially and temporally on the EMCCD, and therefore an on-axis digital hologram is recorded at the SHG wavelength.

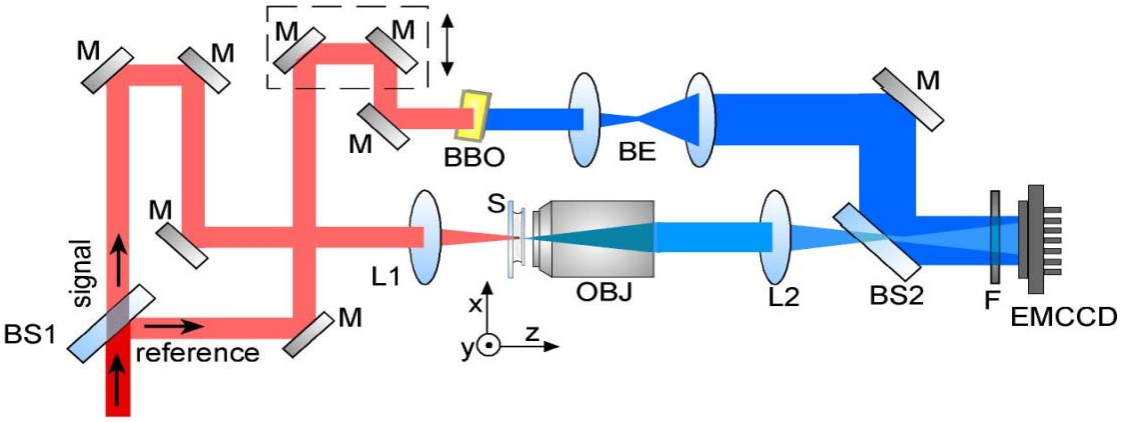

Fig. 4-6 H^2 microscope experimental setup. BS1 and BS2, beam splitters; M, mirror; L1 and L2, lens; S, sample; OBJ, microscope objective; BE, beam expander; F, band-pass filter centered at 400 nm. BS1 splits the laser into signal and reference beams. In the signal arm, L1 slightly focuses the excitation beam into the sample with nanoparticles. OBJ and L2 form a 4F imaging system to collect and optically magnify the SHG image. The EMCCD is placed away from the 4F imaging plane. Bandpass filters are placed in front of the EMCCD to remove the excitation from the SHG signal. The reference beam goes through a motorized delay stage and a BBO crystal so that the coherent reference SHG laser pulses are generated and can be temporally and spatially overlapped with the signal on the EMCCD. The signal and reference beams are combined collinearly by BS2 and therefore an on-axis digital hologram is recorded on the EMCCD.

4.4.2 Point spread function of the H^2 microscope

We prepared a sample of $BaTiO_3$ nanoparticles on a glass substrate for imaging. The nanoparticles were first deposited randomly on a glass slide. Then, the nanoparticles were embedded in index oil, sealed between a cover glass and the glass slide. We imaged an isolated $BaTiO_3$ nanoparticle with the H^2 microscope. The microscope objective in this measurement was a 1.4-NA oil immersion objective. Since the particle size is smaller than the optical diffraction limit at the SHG wavelength, the image of a single particle reflects the spatial resolution of the H^2 microscope.

Following the recording and reconstruction of the holographic imaging described in the previous sections, we recorded an on-axis digital hologram of the SHG field radiated from the nanoparticles and reconstructed the complex SHG field. By reconstructing the signal field at different depths from a single hologram, we obtained successive optical section images, which become a 3D data cube for 3D visualization, as shown in Fig. 4-7.

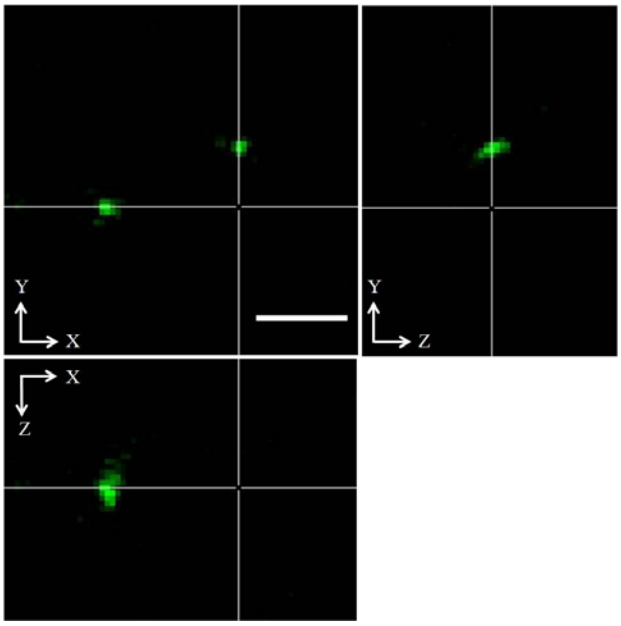

Fig. 4-7 Section and cross-section SHG images of two isolated $BaTiO_3$ nanoparticles, reconstructed from a single on-axis digital hologram. Sub-micron 3D localization of the SHG nanoparticle is achieved. The bar in the image is 1 μm.

In Fig. 4-7, we plot the section and cross-section images of the 3D data cube where two isolated single nanoparticles were within this volume of interest. The 3D localizations of the nanoparticles can be clearly seen, and the result is comparable to that of a SHG scanning microscope. The 3D image of the nanoparticle can be seen as the point spread function of the H^2 microscope. The lateral and axial resolutions of the H^2 microscope are measured as 355 nm and 472 nm, respectively, which agree reasonably with the theoretical values of 348 nm and 408 nm. We also plot the successive section images at different depths of one nanoparticle in Fig. 4-8.

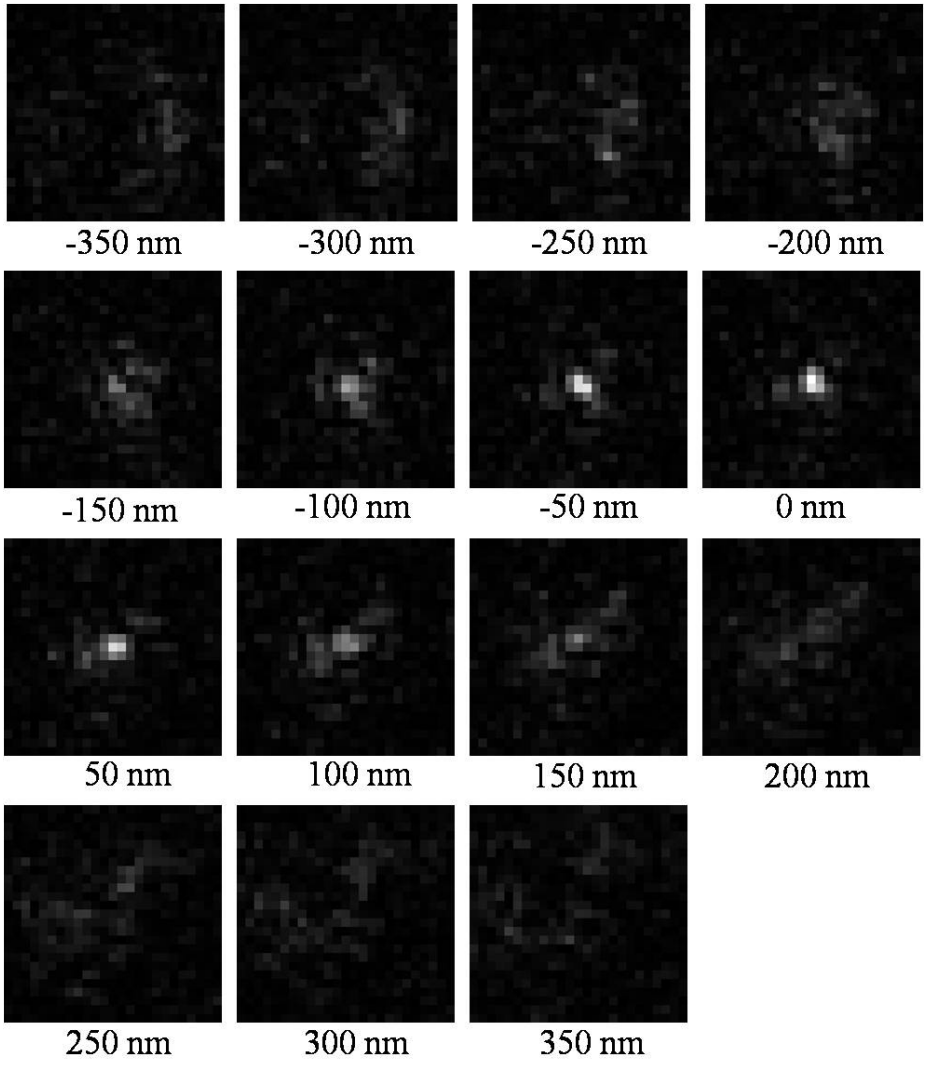

Fig. 4-8 Optical successive section images of an isolated $BaTiO_3$ nanoparticle at different depths (indicated in the figures), reconstructed from a single on-axis digital hologram. The size of the images is $1.5 \times 1.5\ \mu m^2$.

4.4.3 Scan-free 3D imaging of SHG nanoparticles

The 3D imaging capability of the H^2 microscope for SHG nanoparticles was further evaluated by imaging an artificial 3D sample. We prepared a 3D distribution of nanoparticles by randomly embedding 30 nm $BaTiO_3$ nanoparticles in a ~ 100-μm-thick polydimethylsiloxane (PDMS) film. The nanoparticles were immobilized inside the film when the PDMS was cured. Fig. 4-9 (a)–(d) show the conventional SHG microscope images of four sub-micron isolated $BaTiO_3$ nanoparticles on four different planes. These four groups of nanoparticles were then imaged by the H^2 microscope. The results are shown in Fig. 4-9 (e)–(h). We changed the focus by digitally reconstructing the images at different planes. The relative depths of the reconstructed planes were 0, 9.4, 17.2, and 20.3 μm, respectively. The reconstructed images in Fig. 4-9 (e)–(h) agree well with the SHG images in Fig. 4-9 (a)–(d), suggesting that 3D distributions of nanoparticles can be reliably recorded and interpreted from a single digital hologram without scanning. It is worth noting that the H^2 microscopy would have difficulty imaging a high density of nanoparticles [120]. This difficulty results from the intrinsic speckle noise and it is a fundamental limit of storing 3D information with a 2D image. However, when the density of nanoparticles is low, the H^2 microscopy with SHG nanoprobes makes scan-free 3D imaging possible.

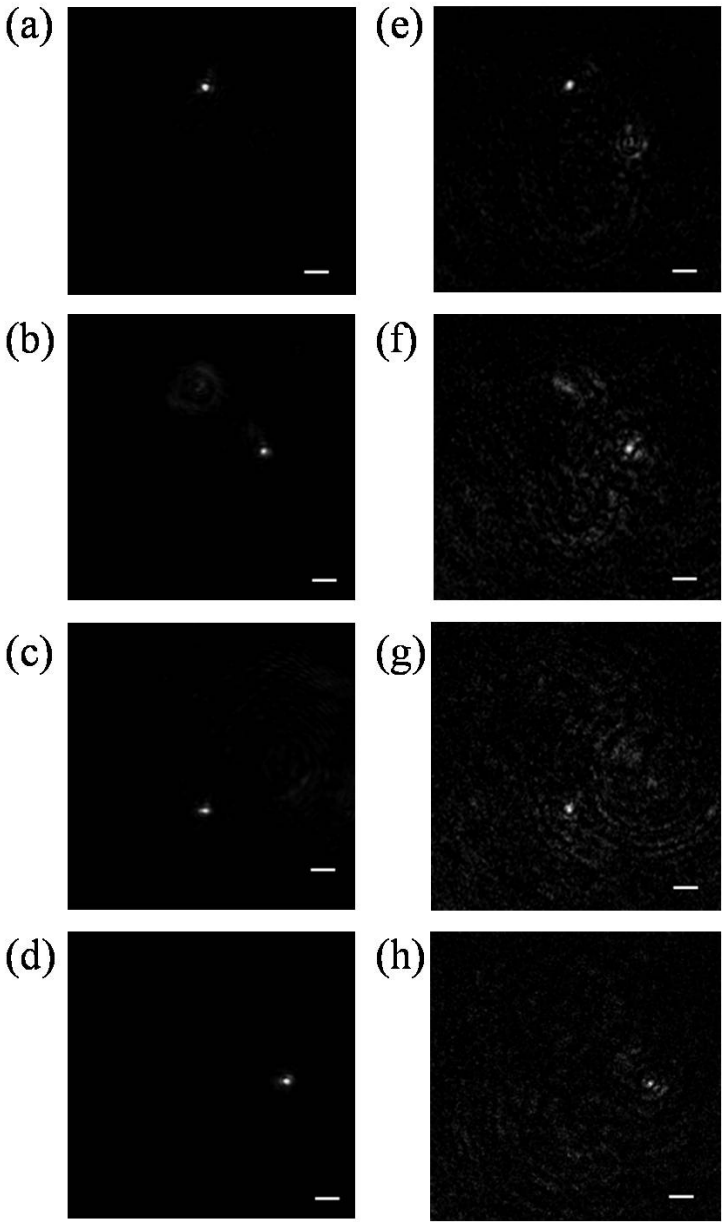

Fig. 4-9 Images of SHG nanoparticles embedded in PDMS. (a)–(d): SHG images of the nanoparticles on four different planes, focusing by moving the optics with a conventional microscope. (e)–(h): Holographic reconstructed images of the corresponding nanoparticles, focusing by digital reconstruction. The relative depths of these four planes are 0, 9.4, 17.2, and 20.3 μm, respectively. Scale bars are 2 μm.

SHG nanoprobes make scan-free 3D bio-imaging possible when they are labeled on the targets of interest and imaged with the H^2 microscope. Here, we demonstrate the 3D bio-imaging capability of the H^2 microscopy. The sample under analysis was mammalian (HeLa) cells non-specifically labeled with SHRIMPs. HeLa cells were

incubated for 24 hours at 37^{o}C with 30 nm $BaTiO_3$ particles that were stabilized with aminomethylphosphonic acid. During the incubation, the cells uptook the nanoparticles through endocytosis [107]. The nanoparticles were engulfed non-specifically into vesicles and packed as clusters randomly by the cells. In this way a 3D distribution of nanoparticles was formed inside the cells. We washed away the unbound nanoparticles with buffer solution (phosphate buffered saline, PBS) and fixed the cells with 3.7% parafolmaldehyde.

The sample was imaged by the H^2 microscope. Fig. 4-10 (a) shows the superposition of the bright field transmission image of a cell and the SHG image from nanoparticles taken by a conventional microscope. In Fig. 4-10 (a), we observed that some nanoparticles appeared as bright spots because they were in focus, while the others were not visible because they were out of focus. We assign six groups of the nanoparticles in Fig. 4-10 (a) with unique numbers for ease of discussion. We imaged the same area with the H^2 microscope. By digital reconstruction, we observed that several nanoparticles appeared on different planes. Fig. 4-10 (b)–(d) shows the reconstructed images on three different depths of the cell (0, 3.12, and 6.24 μm) where different nanoparticles came into focus, respectively. Since the cells uptook the nanoparticles randomly, the size of the nanoparticle clusters, and therefore the SHG intensity, varied in a wide range (about a factor of 10). We see strong signal from the cluster number 4 both on the depths of 0 and 3.12 μm because it is a big cluster. Fig. 4-10 (e) shows the normalized line intensity profiles of the six groups of the nanoparticles when they are on focus through digital reconstruction. All of them show a high signal-to-noise ratio. The cluster number 3 has a weak signal, and in its line intensity profile we can see the defocused signal from the cluster number 4. The acquisition time of the digital hologram was 1 minute, limited by the integration time

for detectable signal. The acquisition time can be further optimized by increasing the excitation power and also the sensitivity of the detection. The peak intensity used in the experiment was 100 times weaker than the critical intensity affecting the cellular metabolism [119], so there is a room to further increase the pump intensity, and, as a result, the SHG signal intensity. The collection efficiency of the SHG signal was ~ 1%, which could also be significantly improved by adapting the optics for the SHG frequency. Moreover, the reference beam in holography can serve as a coherent local oscillator, leading to a gain in signal-to-noise ratio and a shot noise-limited performance of detection even at fast read-out [69]. As a pulsed holographic technique, the H^2 microscopy could reach a temporal resolution limited by the laser pulse width [121].

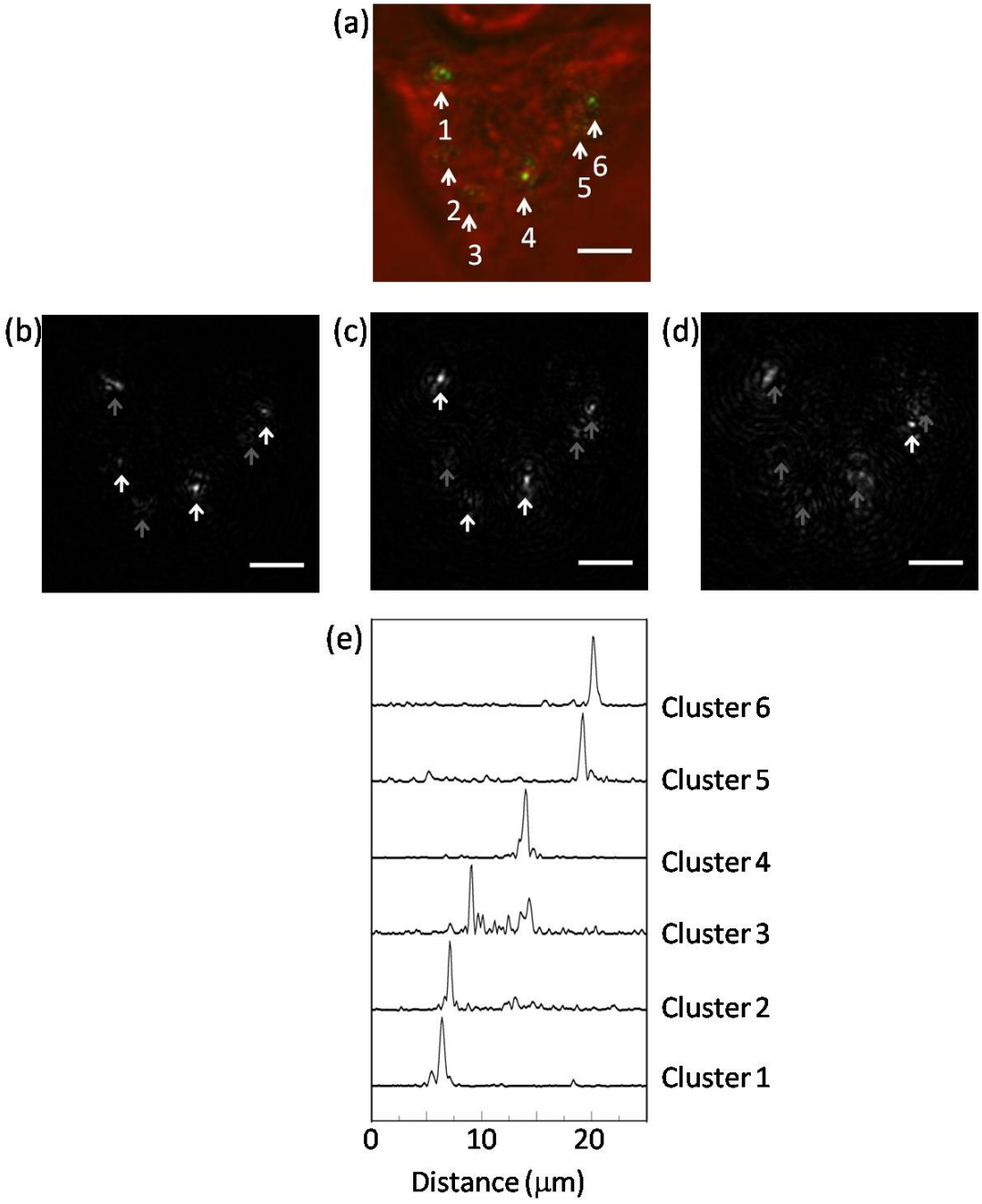

Fig. 4-10 Images of nanoparticles non-specifically labeling HeLa cells. (a) Superposition of the bright field transmission image of a HeLa cell (in red) and the SHG image of nanoparticles (in green) taken by a conventional microscope. Six groups of nanoparticles assigned with numbers were under analysis. Some of them cannot be seen clearly because they are out of focus. (b)–(d) H^2 reconstructed images at three different planes with relative depths of 0 μm, 3.12 μm, and 6.24 μm, respectively. The white arrows show the nanoparticles that are in focus, while the gray arrows show the nanoparticles that are out of focus. The group labeled with number 4 is a big cluster so that it is bright both in (b) and (c). (e) Normalized intensity line profiles of the six nanoparticles when they are on focus through digital reconstruction. The scale bars are 5 μm.

Chapter 5 Imaging through scattering media by digital phase conjugation

Imaging through turbid media has been a highly desirable capability but its implementation remains challenging. The random inhomogeneous optical properties in the turbid medium distort the optical wavefront and cause the loss of resolution. Optical scattering of biological tissues has limited the efficiency of optical power delivery inside biological tissues for phototherapy. Scattering also impedes imaging objects behind a diffusive screen. In this chapter, we demonstrate SHG nanoparticles as light beacons for focusing light on the nanoparticles inside a scattering medium. This is achieved by performing digital optical phase conjugation of the SHG field originated from the nanoparticles. We also demonstrate a scanning phase-conjugate microscope which allows us to image through a thin diffusive screen by scanning the phase-conjugated focus in the vicinity of the nanoparticle.

5.1 Overview of imaging through scattering media

The general idea of imaging through scattering media is to suppress scattering by tailoring the wavefront of the incident light. When the optimized wavefront is illuminated onto the scattering medium, it compensates for the scattering and a desired optical pattern, such as an image or a focus, forms at the output scattered field. The key is therefore how to find the optimized wavefront for the illumination. It is not trivial to find the optimized wavefront because of the complexity of the scattering.

Adaptive optics and wavefront optimization aim to suppress the scattering effect by measuring and then correcting for the inhomogeneities [122–130]. The schematic

diagram of wavefront optimization is shown in Fig. 5-1. It is based on a feedback loop between the active wavefront modulator, usually a spatial light modulator (SLM), at the input beam and the detection of the scattered field at the output. Through optimization algorithms, it has been demonstrated that the optimal wavefront is able to cancel out the scattering and forms an optimal focus at the output [122, 123, 125, 126, 129, 130]. A deeper approach is to measure the transmission matrix of the scattering medium [127, 128]. With the knowledge of the transmission matrix, one can calculate the tailored wavefront at once by solving the inverse problem for projecting an arbitrary image through the scattering medium. This is a very powerful capability. The main challenge of wavefront optimization is the speed of searching for the optimized wavefront. Due to the sequential nature of the measurement, it generally takes a few minutes, limited by the speed of the wavefront modulator (i.e., the reconfiguration speed of the SLM). The scattering medium is required to be stationary during the characterization. Therefore, it can be difficult to image through a time-varying scattering medium. Very recently, a novel method of searching the optimized wavefront has been demonstrated, using a pair of fast scanning mirrors to visit different spatial frequencies of the input beam, and the searching time has been shortened to be less than 1 second [129].

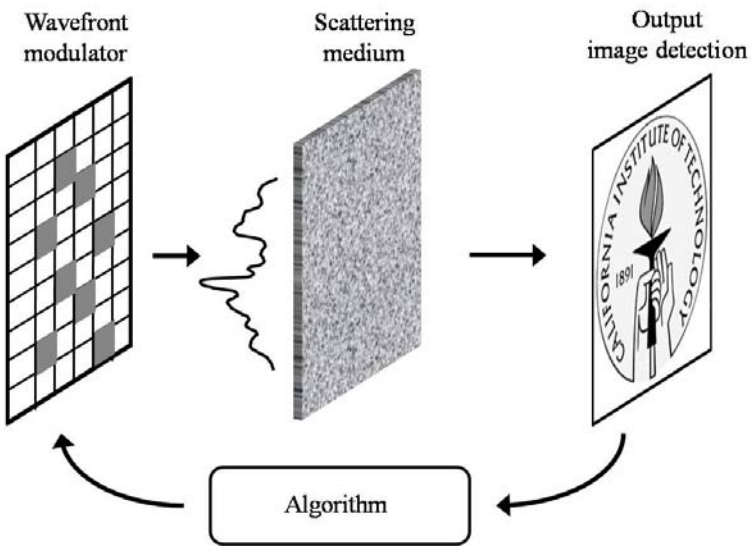

Fig. 5-1 Schematic diagram of projecting an image through a scattering medium by wavefront optimization

Holography has also been demonstrated as a promising approach for imaging through inhomogeneous media since the 1960s [131–135]. The basic idea is to record the phase disturbance due to the scattering medium in a hologram before imaging and use the recorded hologram to compensate for the scattering during imaging so that a clear image can be obtained. One of the holographic approaches for imaging through turbidity is optical phase conjugation [67, 68, 132, 134, 136–139]. Holography allows us to generate a back-propagating phase-conjugated scattered field that readily cancels the scattering of the medium. Besides holography, a phase-conjugated field can also be generated through a nonlinear process, using four-wave mixing in a nonlinear medium [140, 141].

The schematic diagram of imaging through scattering media by optical phase conjugation is shown in Fig. 5-2. In optical phase conjugation, an image is placed behind a scattering sample and the scattered field is recorded from the outside of the sample by holography. The phase-conjugated scattered field is then generated from the recorded hologram and sent back to the sample. The turbid medium will undo the

initial scattering and the original image will form behind the scattering medium. Projecting an image through a biological tissue by phase conjugation was demonstrated by using a photorefractive crystal [136, 137]. Recently it has been reported that the optical phase conjugation can be done all-digitally [67, 138, 142]: the scattered field is recorded by digital holography and the phase-conjugated beam is generated by using a SLM. The digital optical phase conjugation has greatly increased the speed and efficiency of the optical phase conjugation. The holographic recording time is determined by the integration time of the digital camera and the reconfiguration speed is limited by the speed of the wavefront modulator. Both of them are now readily available on the order a few tens of milliseconds. Moreover, digital phase conjugation provides quantitative complex field information of the scattered field, which offers more control and flexibility for further signal processing and analysis. In digital phase conjugation, the phase-conjugated beam is adapted to the holographic recorded scattered field, so there is no need to sequentially search for the optimized wavefront. As a result, digital phase conjugation has the potential to be a fast and efficient technique for scattering suppression.

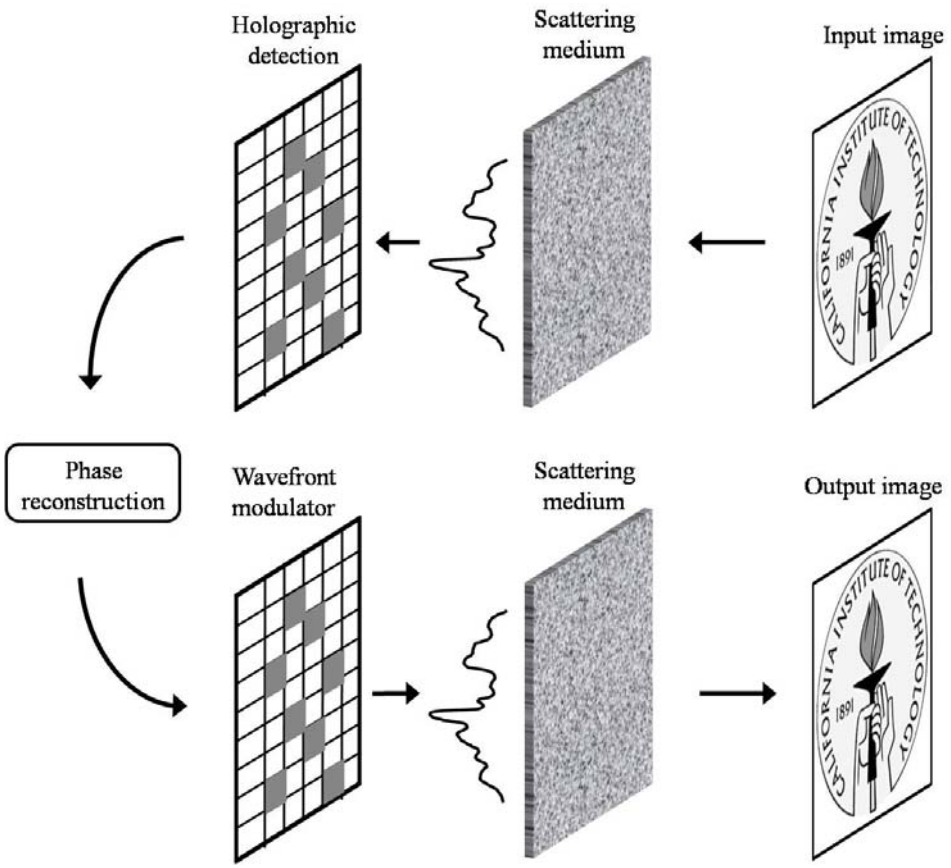

Fig. 5-2 Schematic diagram of projecting an image through a scattering medium by phase conjugation

A common shortcoming of wavefront optimization and phase conjugation is the necessary access at both sides of the scattering medium, which is often a severe disadvantage, especially when it is not tolerable in the applications. Specifically, if one wishes to focus light behind a scattering medium by wavefront optimization, local feedback detection behind the scattering medium is needed for creating the focus. For the measurement of transmission matrix of the scattering medium, it is essential to have complete control and detection of the complex field before and after the scattering. In the case of optical phase conjugation, since the phase-conjugated image falls on the same side of the scattering medium as the original object, a coherent point source behind the scattering medium is required for creating the phase-conjugated focus. The access behind the scattering medium can be avoided by using acoustic

beacons [139] or beacon nanoparticles [67, 143]. The beacon nanoparticles are fluorescent or SHG nanoprobes. When the beacon nanoparticles are introduced behind the scattering medium, they act as local point sources under excitation. The beacon nanoparticles facilitate the local feedback detection in wavefront optimization [143] and also the coherent point sources in optical phase conjugation [67].

5.2 Concentrating light on nanoparticles behind scattering layers

In this section, focusing light through scattering media by digital phase conjugation using SHG nanoparticles will be demonstrated. SHG nanoparticles fit this application perfectly because they provide a coherent and strong contrast at SHG wavelength in a generally unstructured or isotropic turbid environment. When a SHG nanoparticle inside a turbid sample is excited at the fundamental frequency, it emits coherent SHG signal at the SHG frequency like a point source. Therefore, a coherent point source at the SHG frequency for optical phase conjugation can be obtained without any prior knowledge of the turbid sample. The role of the nanoparticle in this approach can be seen as a beacon of the focusing light: the nanoparticle helps us find the tailored wave front for focusing light around it. The SHG scattered field from the nanoparticle is recorded by digital holography where the complex scattered field is captured in a single shot. The phase-conjugated SHG field is calculated and generated by using a phase-only SLM. The phase-conjugated field is then sent back to the sample, and it forms a nearly ideal focus spot on the nanoparticle behind a turbid sample.

5.2.1 Sample preparation and experimental setup

We used 300 nm (in diameter) $BaTiO_3$ nanoparticles as the SHG beacon nanoparticles. The $BaTiO_3$ nanoparticles were deposited on a microscope cover slip (~ 145 μm in thickness). The turbid medium is composed of two layers of Parafilm M laboratory film (~ 130 μm in thickness each) attached on a cover slip by two layers of double-sided tape (~ 80 μm in thickness each, Scotch, 3M). Assuming the absorption of the turbid medium at 400 nm wavelength is negligible, we measured the quantity of $\mu_s l$ (μ_s, effective scattering coefficient, l, thickness of the sample) of the turbid medium at 400 nm wavelength by measuring the transmitted ballistic light. Experimentally, a collimated 1-mm-diameter pulse laser beam centered at 400 nm wavelength was obtained by frequency doubling a Ti:sapphire oscillator (150 fs laser pulses at 80 MHz centered at 800 nm) with a BBO crystal. The laser beam illuminated the scattering medium, and the transmitted light was estimated by measuring the portion of light transmitted through a 1-mm-diameter iris placed 3 meters away from the turbid medium. The $\mu_s l$ of the turbid medium was measured to be ~ 8.5. With the effective thickness of the scattering medium as ~ 420 μm (two layers of the Parafilm and two layers of the double-sided tape), the effective scattering coefficient is estimated to be ~ 200 cm^{-1}. For the demonstration of the concept, we placed the nanoparticles and scattering medium on two independent sample holders which are 1 mm apart from each other, as shown in Fig. 5-3.

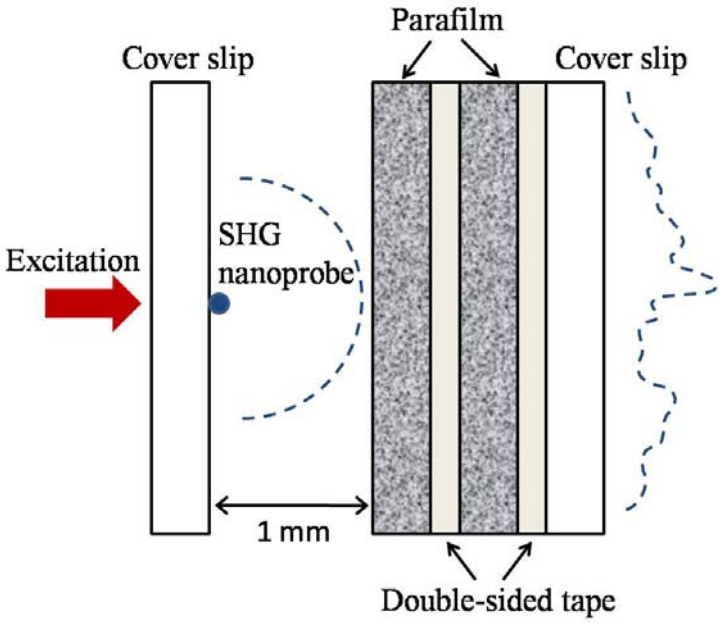

Fig. 5-3 The schematic diagram of the sample structure

The experimental setup is shown in Fig. 5-4. The excitation light source is a Ti:sapphire oscillator generating 150 fs laser pulses at 80 MHz centered at 800 nm. The excitation is focused by a 10x microscope objective (NA 0.25, OBJ1 in Fig. 5-4) onto the SHG nanoparticle through clear media. The average excitation power is approximately 50 mW. The SHG signal from the particle emits in both forward and backward directions. The epi-SHG signal is collected by the same microscope objective (OBJ1), reflected by a dichroic mirror, and then imaged on a CCD camera (Scion, CFW-1312M, CCD1 in Fig. 5-4) with a lens of 20 cm focal length (L1).

The forward SHG signal is scattered by the turbid medium after propagating in air by 1 mm. The scattered SHG field is recorded by an off-axis H^2 microscope as described in Chapter 4. Briefly, the H^2 microscope can be understood as a 4F imaging system followed by a holographic recording system. The scattered SHG field from the nanoparticle is collected and optically magnified by a 4F system consisting of a 10x microscope objective (NA 0.25, OBJ2 in Fig. 5-4) and a lens of 20 cm focal length

(L2). The detector of the H^2 microscope is an EMCCD camera (Andor iXonEM+ 885, CCD2 in Fig. 5-4). We put the CCD2 away from the 4F imaging plane so that the scattered field could propagate and fill the detection area of EMCCD. The hologram recording distance, i.e., the distance between the SHG image formed by the 4F system and the EMCCD, is 20 cm. A plane wave at the SHG frequency generated by a separate BBO crystal served as the reference beam. By overlapping the scattered field and reference beam both spatially and temporally on the CCD2, we record an off-axis digital hologram of the scattered SHG field. The angle between the signal and reference arms is ~ 1 degree. The complex scattered SHG field is then extracted from the recorded off-axis digital hologram.

We digitally conjugate the phase of the measured scattered field and project it on to a phase-only reflective SLM (PLUTO-VIS, HOLOEYE). The pixel size of the SLM is $8 \times 8\ \mu m^2$, which matches with the pixel size of the CCD2. A plane wave at the SHG frequency is incident on the SLM and picks up the conjugated phase pattern after the reflection. The phase-conjugated beam is delivered back to the turbid medium through the 4F system. When the optical system is well aligned (i.e., the CCD2 and the SLM are aligned pixel by pixel), the turbid medium will undo the scattering and the phase-conjugated beam is expected to form a focus on the nanoparticle. We evaluate the phase-conjugated focus with the imaging system placed in the epi-geometry (i.e., OBJ1, L1, and CCD1).

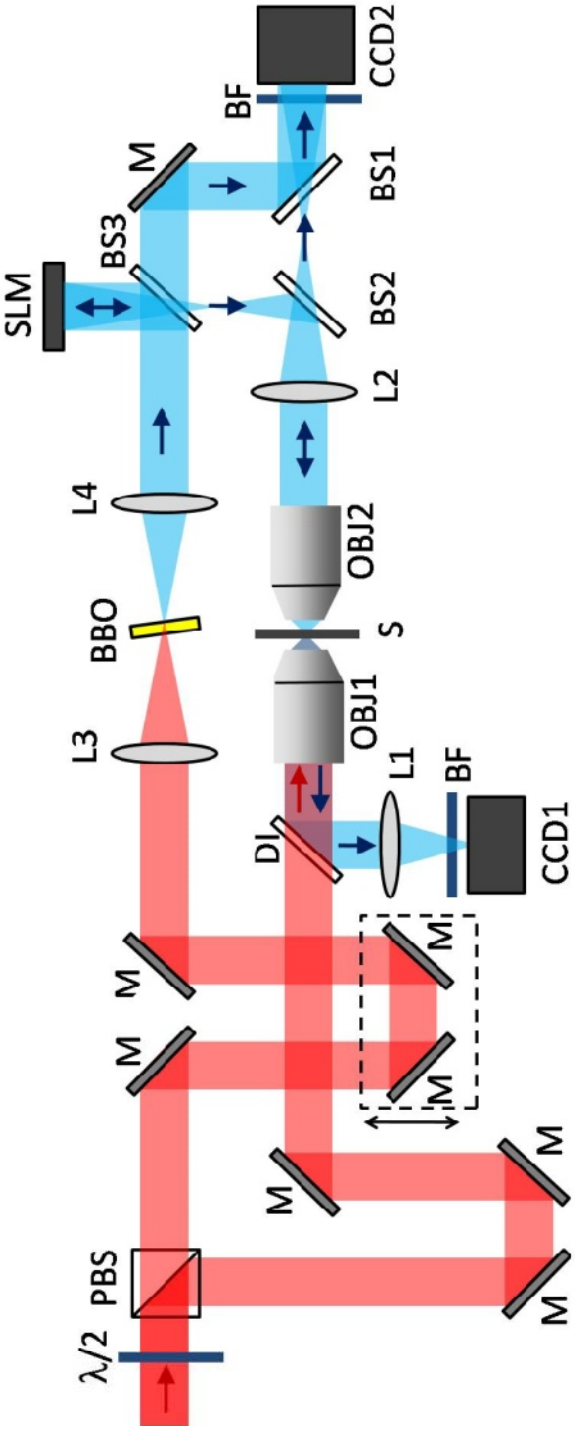

Fig. 5-4 Digital phase conjugation experimental setup. λ/2, half wave plate; PBS, polarization beam splitter; M, mirror; DI, dichroic mirror; L1–L4, lens; OBJ1 and OBJ2, microscope objectives; S, sample; BS1–BS3, non-polarizing beam splitters; BF, band-pass filter centered at 400 nm. The laser power for excitation and phase conjugation can be controlled by the λ/2 and the PBS. A translation stage was used to overlap the signal and the reference pulses temporally for the H^2 microscopy. Band-pass filters are placed in front of the CCD cameras to remove the excitation from the SHG signal.

5.2.2 Results and discussion

We started the measurement without scattering media. An isolated SHG nanoparticle was excited and the epi-SHG image was observed on the CCD1, which is shown in Fig. 5-5 (a). The FWHM of the spot is measured to be 1.95 μm, which is the diffraction limit. The nanoparticle acts as a point source at SHG frequency and the emitted SHG field is similar to a spherical wave in the far field. Therefore, the phase of the SHG field recorded by the H^2 microscope is a spherical wave-front. The conjugation of the measured phase is a Fresnel zone plate as shown in Fig. 5-5 (b). The Fresnel zone plate was projected on to the SLM, and the phase-conjugated beam formed a focus on the nanoparticle after passing through the 4F system. We blocked the excitation and used the epi-imaging system (i.e., OBJ1, L1, and CCD1) to monitor the phase-conjugated focus. When the optical system is well aligned, the focus is exactly located on the nanoparticle. The presence of the nanoparticle at the phase-conjugated focus disturbs the phase-conjugated focus due to the linear scattering of the nanoparticle. Therefore, we removed the nanoparticle from the focus to evaluate the quality of the phase conjugation. The phase-conjugated focus is shown in Fig. 5-5 (c). The FWHM of the phase-conjugated focus is 1.95 μm, showing a good quality of the phase conjugation through a clear medium.

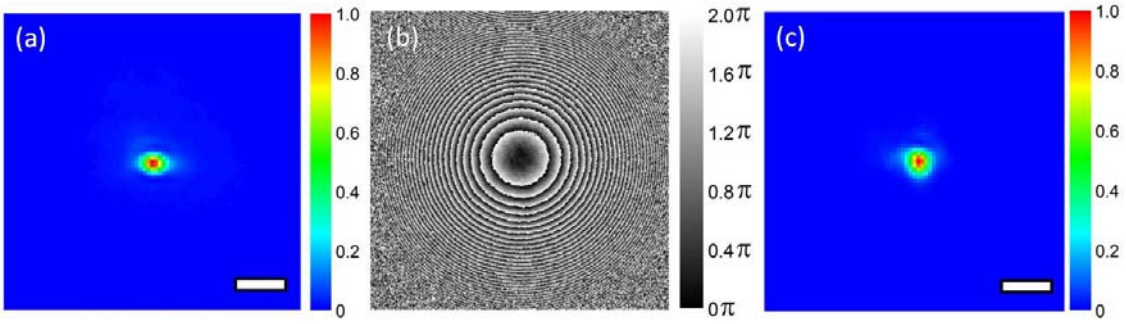

Fig. 5-5 Digital phase conjugation through a clear medium. (a) The epi-SHG image of the nanoparticle under excitation. (b) The conjugated phase pattern of the recorded SHG field emitted from the nanoparticle, showing a Fresnel zone plate. (c) The phase-conjugated focus formed at the sample by using the Fresnel zone plate shown in (b). The FWHM of the bright spots in (a) and (c) is 1.95 μm. The scale bars in the figures are 5 μm.

We then placed the turbid medium 1 mm away from the sample of nanoparticles as shown in Fig. 5-3 and repeated the measurement. The SHG field from the nanoparticle under excitation was scattered and recorded by the H^2 microscope. The acquisition time of the digital hologram is approximately 1 second. The conjugation of the measured phase is shown in Fig. 5-6 (a). The random phase information implies the phase of the SHG field has been severely disturbed by the scattering media. When the phase pattern in Fig. 5-6 (a) was projected on the SLM, the phase-conjugated beam was able to form a focus at the position where the nanoparticle was located, as shown in Fig. 5-6 (b). The FWHM of the conjugated focus in Fig. 5-6 (b) is 2.3 μm, which is close to the diffraction limit of the system. When we used the Fresnel zone plate pattern (as shown in Fig. 5-5 (b)) on the SLM, no focus could be formed through the turbid medium due to the scattering. A speckle pattern was observed as shown in Fig. 5-6 (c). Comparing Fig. 5-6 (b) and (c), it is clear that much more optical power is delivered to the focus spot when the phase conjugation is performed with the measured phase pattern. The ratio between the total power within the phase-conjugated bright spot (within the FWHM area) and the average power of the speckle

pattern within the same size of area is measured to be 30. In Fig. 5-7, we plot and compare the intensity profiles of the diffraction-limited focus (as shown in Fig. 5-5 (c)) and the phase-conjugated focus through the turbid medium (as shown in Fig. 5-6 (b)). Nearly ideal focus was obtained by the digital phase conjugation through the turbid medium.

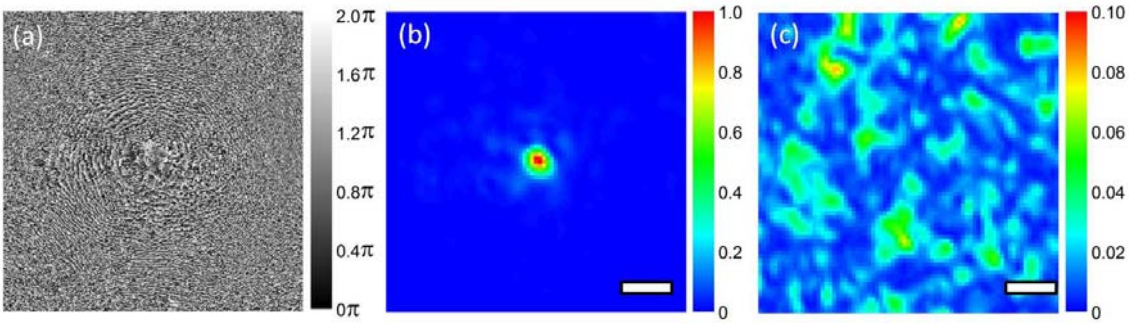

Fig. 5-6 Digital phase conjugation through a turbid medium. (a) The conjugated phase pattern of the scattered SHG field. (b) The normalized intensity image of the phase-conjugated focus through a turbid medium by using the phase pattern shown in (a). The FWHM of the spot is 2.3 μm. (c) The normalized intensity image of the distorted focus without phase conjugation. No focus is observed. Note that (b) and (c) are measured with the same power of the phase-conjugated beams and they are normalized by the same factor in the image processing. The scale bars in the figures are 5 μm.

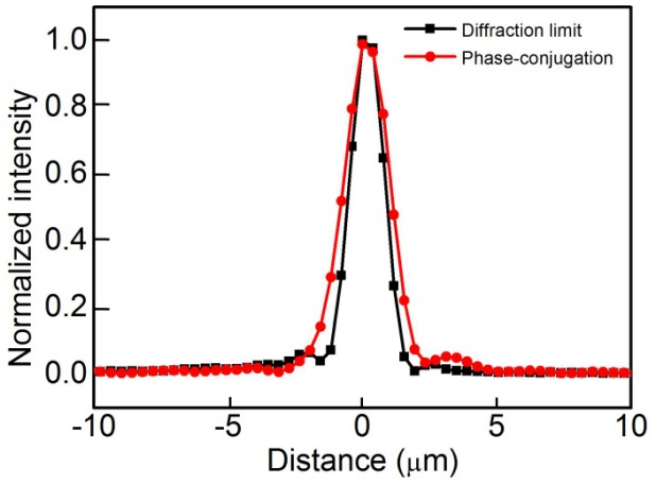

Fig. 5-7 Comparison of the measured diffraction limited focus and the phase-conjugated focus. Black: the normalized intensity profile of the diffraction limited focus; red: the normalized intensity profile of the phase-conjugated focus. The FWHMs of the diffraction limited focus and the phase-conjugated focus are 1.95 μm and 2.3 μm, respectively.

The phase-conjugated focusing we observed was remarkable considering that we captured only a portion of the scattered field. The SHG signal emitted from the nanoparticle under excitation is a femtosecond laser pulse. When it is incident on the turbid medium, the pulse will spread temporally into a ballistic component and a diffuse component due to the scattering [144]. In our digital holographic recording, the coherence length of the reference beam is ~ 150 fs (determined by the laser pulse width) which is only able to capture part of the diffused scattered field. We adjusted the time of the reference pulse arriving at the CCD camera so that the strongest contrast of the hologram was observed. The holography faithfully recorded part of the scattered field within the coherence length of the reference pulse. In our phase conjugation setup, a plane wave of ~ 150 fs pulse width was used to carry the conjugated phase pattern. As a result, it can be understood that the phase conjugation was performed only for the holographic-recorded portion of the scattered field. The phase-conjugated focusing can be improved if the temporal diffused light is considered. It has been reported that the local complex field with temporal information can be measured by using SHG-active nanoparticles [145]. We expect an optimal spatio-temporal focusing can be achieved by combining optical phase conjugation and proper pulse shaping.

It is worth noting the role of polarization in our experiment. The laser at the fundamental frequency was divided into s- and p-polarizations by a polarization beam splitter (PBS in Fig. 5-4). The s-polarization was used to excite the nanoparticle. The p-polarization was frequency doubled by a BBO crystal through type I phase matching, so the polarization of the reference beam and the phase-conjugated beam at the SHG frequency were s-polarized. The nanoparticle under s-polarized excitation emits the SHG signal in all polarizations through the second-order nonlinear

susceptibility tensor [56]. The nanoparticle signal is then being scattered by the turbid medium, which further depolarizes the signal. When using an s-polarized reference beam, we only capture the s-polarized component of the scattered SHG field of the nanoparticle. The information contained in the p-polarized scattered field is discarded. Therefore, the digital phase conjugation is only performed for an s-polarized scattered field. We expect a better quality of the phase-conjugated focus if both of the polarizations are considered.

It is also critical to consider the resolution of our optical system compared to the size of the speckles in the scattered field. When the turbid medium is highly scattering, the scattered field at the output surface of the turbid media can have a speckle size approaching the diffraction limit of light (~ 0.24 μm FWHM at 400 nm wavelength). This is because the turbid medium scatters light in all the directions randomly so that a broad angular distribution of the scattered light can be formed, which leads to a small speckle size. In our experiment, the resolution of the optical system is ~ 0.98 μm, limited by the NA 0.25 microscope objective. A scattered field of higher spatial frequency would not be captured in the hologram, and therefore, is not considered in the phase conjugation. Besides, the scattered field is recorded by off-axis holography which inevitably degrades the resolution of the optical system. To minimize this effect, we experimentally remove the non-interferometric part (i.e., the signal and reference) from the digital hologram by subtracting a background of the two pulses not being temporally overlapped. As a result, the spatial resolution is controlled and decreased by a factor of 2 in only one transversal direction. The resolution of the optical system can be increased by using a higher NA microscope objective, and thus a tighter phase-conjugated focus is achievable.

5.3 Imaging through scattering layers by using SHG beacon nanoparticles

Wavefront correction allows us to form a nearly optimal focus inside a turbid sample, but a loftier goal is to image an object that is behind the scattering medium. When the turbid medium is sufficiently scattering, two points in the scattered field become completely uncorrelated when the distance between the two points are beyond the diffraction limit [146]. As a result, the wavefront correction is site-specific and must be modified for every focus point on the sample. Scanning the focus on the sample to form an image would be expected to be very time-consuming and not practical. Recently, it has been shown that when the turbid medium is thin and at a distance away from the imaging plane, it is possible to scan the focus on the sample through a turbid medium with only one tailored wavefront [147]. In this section, we demonstrate the use of digital phase conjugation rather than wave front optimization to achieve this goal. The main benefit of digital phase conjugation is its speed of finding the tailored wave front since no iterative optimization calculations are necessary. With sufficiently bright SHG nanoparticles, the speed is determined by the response time of the SLM, which needs to be reconfigured only once with digital phase conjugation. On the contrary, wavefront optimization requires a large number of sequential modulations of the SLM to find the optimal wave front. Therefore, digital phase conjugation has an inherent advantage in speed.

5.3.1 Concepts

The method we used for imaging through turbid media consists of two steps: (1) measuring the local response of the turbid sample by holographically recording the complex scattered field emitted from a coherent point source, and (2) scanning the

phase-conjugated focus on the sample and measuring the transmitted field to form an image. The first step is depicted in Fig. 5-8 (a). A nanoparticle at $z = 0$ emits SHG field as a coherent dipole point source under excitation. The SHG emission is close to a spherical wave in the far field. The SHG emission propagates in free space and is then scattered by the turbid medium placed at a distance $z = D$. The scattered field is recorded by digital hologram where the complex field information is captured. This information can be seen as the local response of the turbid medium corresponding to the input of a spherical wave.

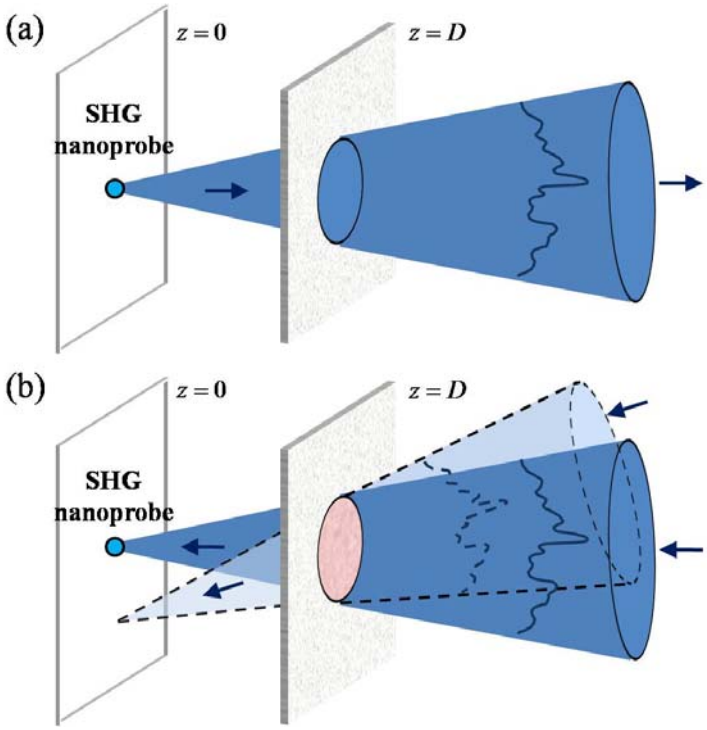

Fig. 5-8 Two steps of imaging through turbid media in a phase conjugate scanning microscopy. (a) Recording the scattered SHG field radiated from a nanoparticle by digital holography. (b) Scanning the phase-conjugated focus on the imaging plane by illuminating the same region of the turbid medium (shown as the red circular region) with the phase-conjugated beam at different angles

In the second step, the phase-conjugated field is recreated from the recorded hologram using a phase-only SLM. The phase-conjugated scattered field is then sent back to the sample as shown in Fig. 5-8 (b). The turbid medium undoes the initial

scattering, and a phase-conjugated focus forms at the position where the nanoparticle is initially placed. To achieve imaging with the phase-conjugated focus, it is critical to have the capability of moving the focus away from its initial position. Consider the situation in Fig. 5-8 (b) where the phase-conjugated beam is tilted and illuminates the same region where the local response has been characterized (shown as the red circular region). When the tilt angle is small and the turbid medium is thin, the phase-conjugated beam passes through almost identical (i.e., highly correlated) portions of the perturbing medium [133, 147]. As a result, the turbid medium cancels the wavefront distortion, and a tilted converging beam can be obtained right behind the turbid medium. This phenomenon was known as optical memory effect and it was first studied in the 1980s [148]. More quantitative results of phase conjugation based on optical memory effect will be presented in the following sections. We found that the best results were obtained by ensuring that the phase-conjugated beam passes through the same region on the scattering medium while scanning. This requires that the illuminating beam is swept and simultaneously shifted so the light beam pivots around the same illumination region on the turbid medium.

5.3.2 Experimental details

In this experiment, the turbid medium is a commercial ground glass diffuser (Edmund Optics, NT43-723) with characterized surface roughness. We prepared an object consisting of gold thin film patterns (130 nm thick) on a transparent glass substrate (150 μm thick) by standard photolithography. We used 300 nm (in diameter) $BaTiO_3$ nanoparticles as the SHG nanoprobes. The crystal structure of the $BaTiO_3$ nanoparticles is tetragonal which is non-centrosymmetric and allows for efficient SHG. The nanoparticles were deposited randomly on the image target.

The experimental setup is shown in Fig. 5-9, which is similar to the one shown in Fig. 5-4 with some modifications. The major difference in the setup is that the position of the SLM is now controlled by motorized actuators, so the scanning of the phase-conjugated focus can be achieved by tilting and shifting the SLM simultaneously.

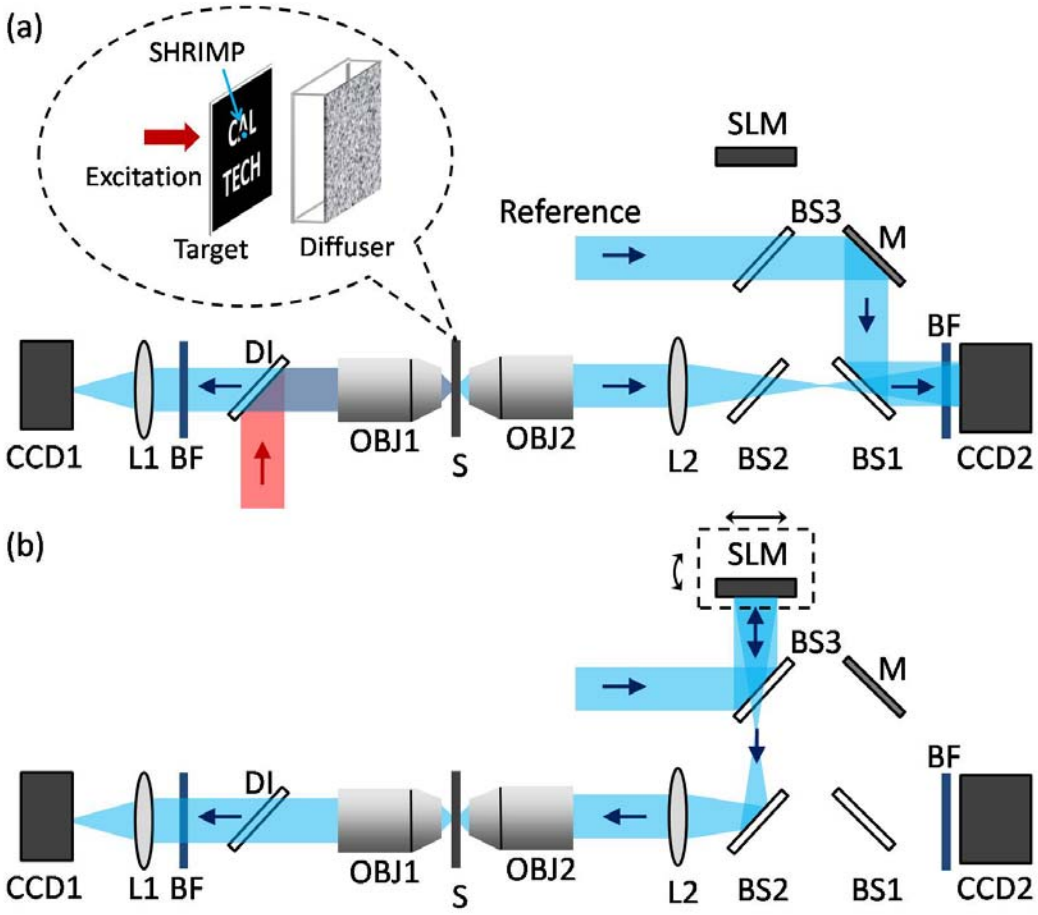

Fig. 5-9 (a) The experimental setup of the harmonic holographic microscopy for recording the complex scattered SHG field. Inset: The illustrative diagram of the sample structure. (b) The experimental setup of the phase conjugate scanning microscope. Note that (a) and (b) show the same setup with different light illuminations for different steps of the experiment. The light not in use is blocked in the experiment and is not shown in the figures. DI, dichroic mirror; L1–L4, lens; OBJ1 and OBJ2, microscope objectives; S, sample; BS1–BS3, non-polarizing beam splitters; BF, band-pass filter centered at 400 nm; M, mirror

The SLM position has six degrees of freedom in space, including three translational directions (two are in-plane lateral and one is axial), two tilt directions (vertical and horizontal), and one in-plane rotation. In our demonstration, the two lateral shift adjustments of the SLM are controlled by two motorized stages, and the two tilt adjustments are controlled by two motorized actuators assembled on a tilt platform. Scanning the phase-conjugated focus can be achieved by rotating the beam around the same region of the turbid medium as a pivot (as shown in Fig. 5-8 (b)), which generally requires a coordination between the tilt and the shift of the SLM. The optical path between the SLM and the lens L2 (20 cm focal length) is 40 cm. This distance is identical to the distance between the CCD2 and the lens L2. As a result, the image of the SLM forms between the focal plane and the OBJ2 as shown in Fig. 5-10 (a). When the SLM is tilted, this SLM image will tilt accordingly (with an optical magnification due to the 4F system) as shown in Fig. 5-10 (b). In Fig. 5-10 (b), it is clear that, after the tilt, the phase-conjugated beam traverses different regions (shown as dashed circles) from the original path (shown as solid circles). In general, the turbid medium is not placed at the SLM image plane and therefore it is necessary to shift the SLM image correspondingly so that the tilted beam passes through the same region of the turbid medium. It is worth noting that our approach achieves a true pivoting beam, while a conventional two-axis raster scanner results in a pivoting-like beam because the two-axis scanning is done by two separate mirrors. It is also interesting to note that the mechanical tilt and shift of the SLM are equivalent to electronically modulating the phase pattern on the SLM. One would need to calculate a new phase pattern for each specific tilt and shift. The motionless digital scanning may have advantages in some applications where mechanical scan is not allowed.

In order to form the image, we raster scanned the phase-conjugated focus on the image plane. For the detection of the signal, we replaced the CCD1 in Fig. 5-9 (b) by a point detector, a photomultiplier tube (PMT), and the transmission signal was measured pixel-by-pixel. When the phase-conjugated focus falls at a transparent area of the target, the signal obtained from the scanning beam is bright. To increase the sensitivity of the measurement, we modulated the phase-conjugated beam by an optical chopper at 300 Hz, and the signal was demodulated and read out with a lock-in amplifier.

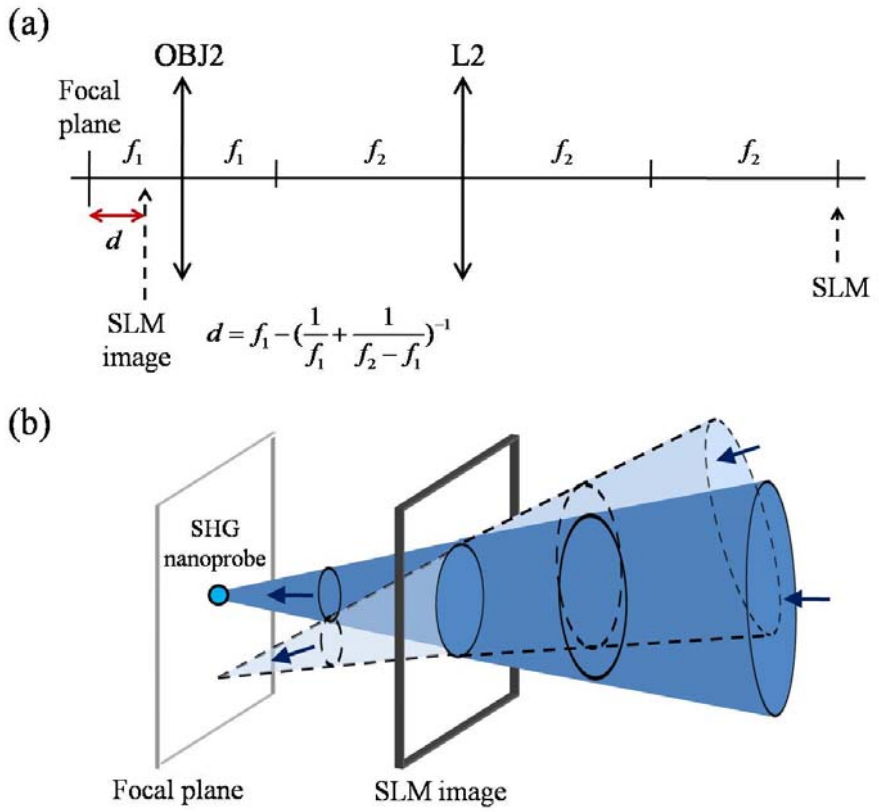

Fig. 5-10 Illustration of the tilt of the phase-conjugated beam as the SLM tilts. (a) The optical diagram of the SLM projection through the 4F imaging system consisting of L2 and OBJ2. Note that the SLM is not placed at the imaging plane of the 4F system, and therefore the SLM image is between the focal plane and OBJ2. Here f1 and f2 are the focal length of the OBJ2 and L2; d is the distance between the focal plane and the SLM image plane. (b) The illustrative diagram showing how the phase-conjugated beam tilts while the SLM tilts. Details of the coordination between the tilt and the shift of the SLM for the scanning are in the main text.

5.3.3 Results and discussion

We verified that the diffuser was sufficiently scattering by placing it at the output aperture of the objective and focusing directly through it without phase conjugation. The speckle pattern obtained on the image plane is shown in Fig. 5-11 (a). To focus through the turbid medium, we performed the phase-conjugation of the scattered SHG field emitted from the nanoparticle. The time for digital holographic recording of the scattered SHG field was 1 second, limited primarily by the CCD integration time. This can be reduced by at least an order of magnitude if more efficient nanoparticles are used [47, 63]. For the purpose of characterization of the optical system, the nanoparticles were randomly deposited on a glass substrate instead of a target. The conjugated random phase pattern (as shown in Fig. 5-11 (b)) is projected on the SLM for generating a phase-conjugated beam. When the phase-conjugated beam illuminated the turbid medium, a sharp focus was observed as shown in Fig. 5-11 (c). The FWHM of the phase-conjugated focus is 2 μm which is the diffraction limit of the optical system. The average intensity within the FWHM of the phase-conjugated focus is approximately 400 times greater than the average diffusive background in Fig. 5-11 (a). Note that Fig. 5-11 (a) and (c) share the same grayscale except the signal intensity in Fig. 5-11 (a) is artificially increased by 100 times for better visualization. Notice that the contrast of the phase-conjugated focus achieved here is more than 10 times higher than that in Section 5.2. This is mainly due to the different optical properties of the turbid media used in these two experiments. Here the turbid medium is a ground glass diffuser where the scattering is due to the surface roughness. As a result, the temporal diffusion of light due to the scattering is very little, allowing the pulsed reference pulse to capture most of the scattered light within the coherence length.

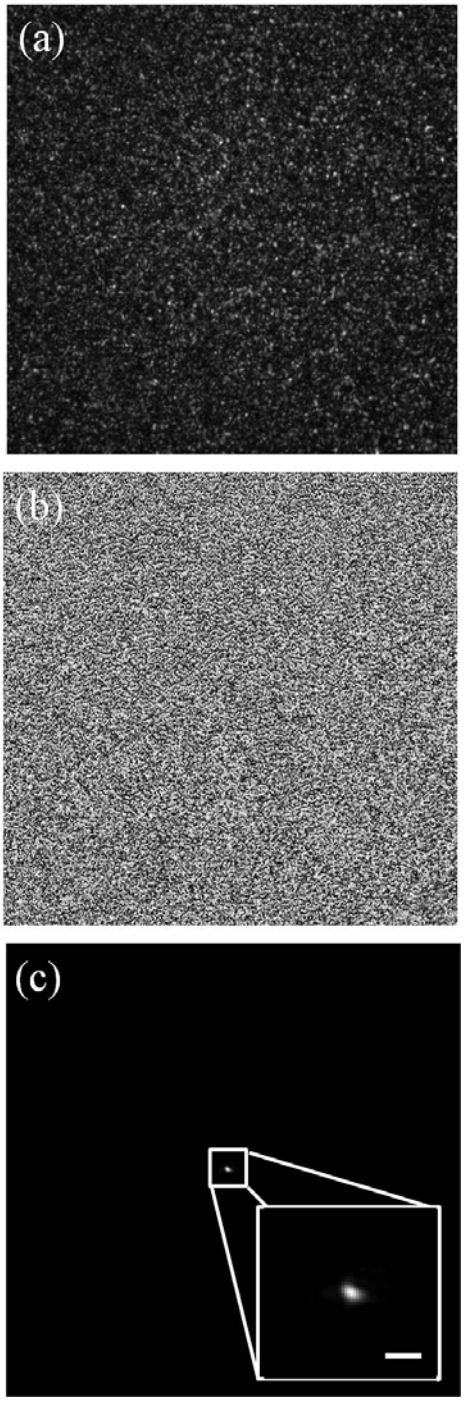

Fig. 5-11 Focusing through the turbid medium without and with phase conjugation. (a) The speckle pattern on the image plane when focusing directly through the turbid medium by the objective without phase conjugation. (b) The conjugated phase pattern projected on the SLM for phase conjugation. The grayscale from black to white represents the phase modulation from 0 to 2π. (c) The phase-conjugated focus on the image plane. The inset shows the magnified image of the focus. The scale bar in the inset is 5 μm. The size of the images in (a) and (c) is 195×195 μm^2.

We then scanned the focus across on the sample by illuminating the phase-conjugated beam on the same region of the turbid medium at different angles via tilting and shifting the SLM accordingly. In our demonstration, the correspondence between the tilt and the shift of the SLM was typically 270 μm shift per 1 mrad tilt. Note that the tilt of the optical beam is double the tilt of the SLM due to the reflection, and the tilt/shift of the phase-conjugated beam at the sample position is increased/reduced by the 4F imaging system by a factor of the optical magnification. While this coordination is maintained, the phase-conjugated focus can be scanned across the sample. To examine the scanning field of view, we tracked and measured the intensity of the phase-conjugated focus as it scanned across the sample by monitoring it on CCD1 in Fig. 5-9. The result is shown in Fig. 5-12. The intensity of the focus remains almost unchanged at small tilt angle, and it decreases by half at a large tilt angle of approximately 55 mrad.

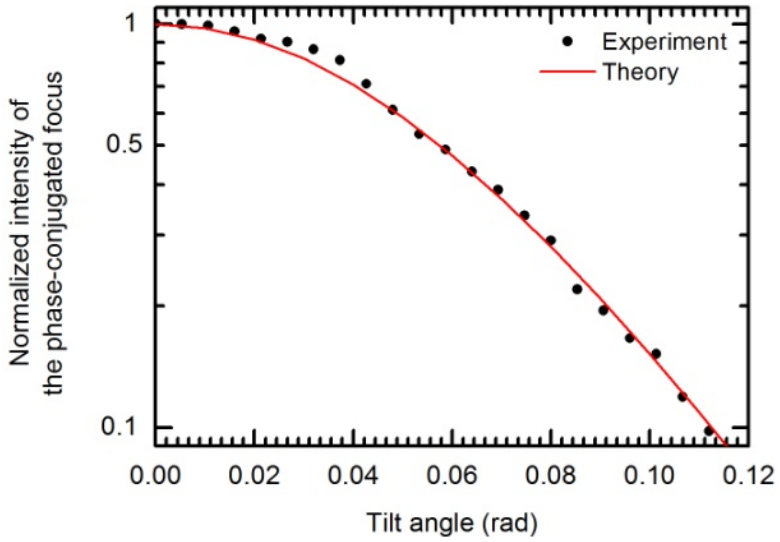

Fig. 5-12 Angular response of the tilted phase-conjugated focus. Note that the tilt angle in this figure is the tilt angle at the sample position. The experimental data is shown as black dots and the fitting based on the theory of optical memory effect is shown as the red line.

The reason that the phase-conjugated focus can be displaced from its initial position is based on the fact that the scattering behavior of a thin turbid medium is highly correlated when the incident beam is tilted at a small angle. This phenomenon has been referred to as the “optical memory effect” and it was studied for different thicknesses of the turbid media [148]. The scattering of the diffuser in our case is due to surface roughness. Therefore the turbid medium is effectively very thin. As a result, the angular range for high correlation in the scattering behavior is large, which allows us to have a large field of view for phase conjugate scanning microscopy. The diffuser we used in the experiment was a 120-grit ground glass, and it has been reported that the root-mean-square surface roughness of a 120-grit ground glass is 3.1 μm, with in-plane characteristic length as 45 μm [149].

Based on the theory of the memory effect, the correlation function $C(qL)$, which is equivalent to the normalized intensity of the phase-conjugated focus, has the form of $C(qL) = [qL/\sinh(qL)]^2$ where $q = 2\pi\delta\theta/\lambda$, $\delta\theta$ is the tilt angle, λ is the optical wavelength, and L is the thickness of the turbid medium [150]. We fit the experimental data in Fig. 5-12 with the theory (shown as the red line) where the only free fitting parameter is the effective thickness of the turbid medium. The experimental observation agrees with the theory very well with the effective thickness L as 1.65 μm.

It should be mentioned that the field of view is also determined by the distance between the turbid medium and the plane of focus of the conjugate beam. In our case, the distance between the turbid medium to the focal plane is approximately 2 mm, leading to a large field of view of 220-μm diameter FWHM. When the turbid medium is directly on top of the focal plane, the field of view in the phase conjugate scanning microscopy vanishes.

We demonstrate the imaging capability of the phase conjugate scanning microscopy by using a metal pattern on a glass substrate as the target. The wide-field light transmission image of the target is shown in Fig. 5-13 (a) where the letters of CALTECH can be seen. The nanoparticles were randomly deposited on the target, and one nanoparticle located at a transparent area was excited from the back of the sample for phase conjugation. The scanning of the phase-conjugated focus was performed by coordinating the tilt and the shift of the SLM as described previously. We scanned the focus across an area of $140 \times 140\ \mu m^2$ on the sample. The transmission signal was collected by the PMT placed at the position of CCD1 in Fig. 5-9 (b). The integration time for each pixel was 30 ms. The corresponding phase conjugate scanning image is shown in Fig. 5-13 (b) where the target is clearly resolved. For comparison, we performed a control experiment without phase conjugation by simply focusing the initial undisturbed spherical wave through the turbid medium on the sample. As expected, the scanning image is very blurry as shown in Fig. 5-13 (c). The intensity profile along the dashed line in Fig. 5-13 (b) is plotted in Fig. 5-14. The uniformly sharp image demonstrates that the locality of the conjugate spot is maintained as it is scanned. The spatial resolution of the system is 2 μm, determined by the diffraction-limited phase-conjugated focus spot size.

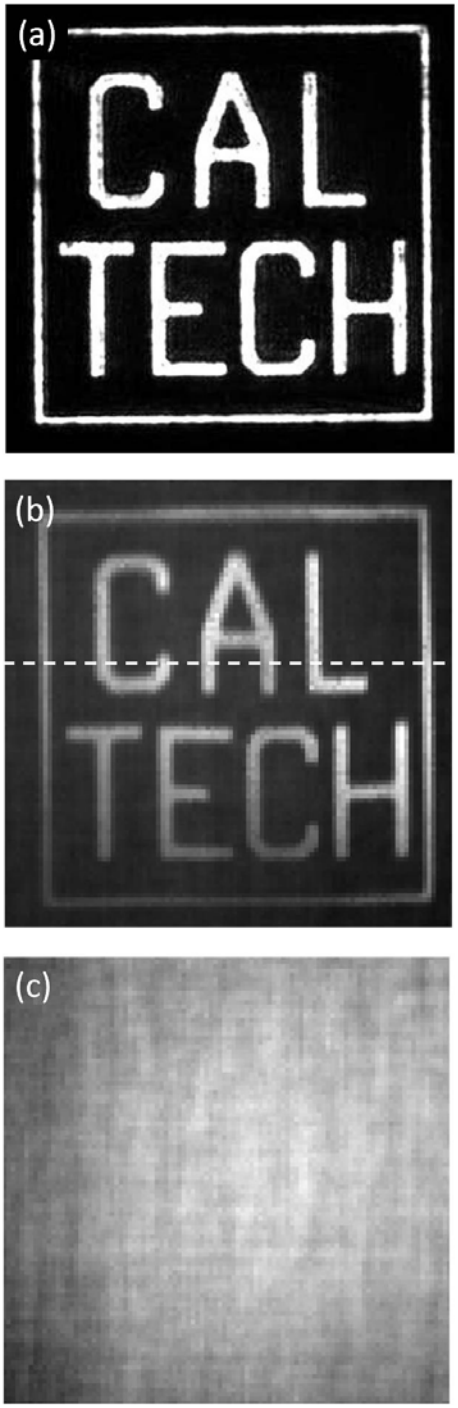

Fig. 5-13 (a) The wide-field transmission image of the target. The target is a 130 nm thick gold pattern on a glass substrate prepared by photolithography. The bright region in this figure indicates the transparent area while the dark region indicates the gold film. (b) The corresponding phase conjugate scanning image of the target. The target is clearly resolved. The intensity profile along the dashed line is plotted in Fig. 5-14. (c) The scanning image of the same target without phase conjugation. Since the focus is severely distorted by the turbid medium, the image is completely blurry. The size of the images are $140 \times 140\ \mu m^2$.

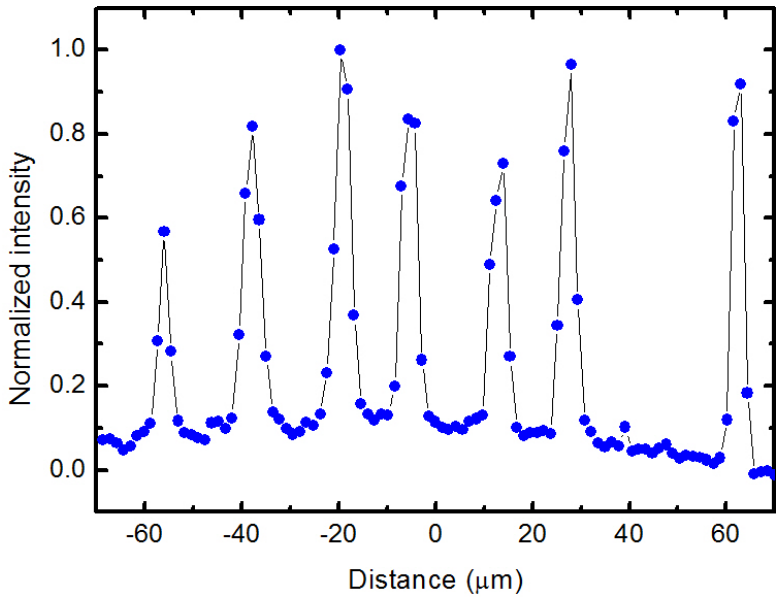

Fig. 5-14 The normalized intensity profile along the dashed line in the phase conjugate scanning image shown in Fig. 5-13. (b) The experimental data points are shown as blue dots.

We would like to mention that the only image processing for Fig. 5-13 (b) is a uniform background subtraction. The typical phase-conjugated focus for scanning was shown previously in Fig. 5-11 (c). The contrast of the focus was high: the peak intensity within the FWHM of the focus was 400 times stronger than the diffusive background. During the scanning, all the light transmitted through the metal pattern was collected by the PMT. Therefore, the total detected power from the diffusive background can be considerable due to the transparent area on the pattern, which contributes a bias background in the scanning image. This background results in a relatively low contrast (~ 0.35) in the raw image. After the uniform background subtraction, the average contrast of Fig. 5-13 (b), defined as $(\bar{I}_{sig} - \bar{I}_{bg})/(\bar{I}_{sig} + \bar{I}_{bg})$, is found to be about 0.7 where $\bar{I}_{sig}$ and $\bar{I}_{bg}$ are the average signal and background intensities. Another important factor is the SNR of the system. To estimate the SNR, we first divided the total imaging area into signal area and background area based on the guide of Fig. 5-13 (a): the bright area in Fig. 5-13 (a) was defined as the signal

area, while the dark area was defined as the background area. The defined signal and background areas were overlaid onto Fig. 5-13 (b). We then calculated the average SNR as the ratio between the average intensity in the signal area in Fig. 5-13 (b) and the standard deviation in the background area in Fig. 5-13 (b). The average SNR was found to be about 25. The SNR was limited by the presence of noise due to the random fluctuation in the diffusive background. Notice that the digital phase conjugation was performed with a phase-only SLM. By using a complex (amplitude and phase) SLM, we expect the intensity of the diffusive background can be further suppressed, and the contrast and SNR of the imaging can be further improved.

Chapter 6 Conclusions and future extensions

In this thesis, we have shown the development of $BaTiO_3$ nanoparticles as SHG nanoprobes for novel imaging applications based on their intrinsic optical properties. The $BaTiO_3$ nanoparticles are efficient in SHG due to the bulk second-order nonlinearity resulting from the noncentrosymmetric crystal structure. The SHG signal from an individual nanoparticle was observed to be stable after the emission of 10^9 photons, allowing us to detect the nanoparticle continuously for 5 hours. Since SHG is a virtual state transition process, we expect the SHG emission remains stable as long as the excitation is not too strong to damage the nanoparticle. We have proposed a theory of the absolute SHG efficiency of nanoparticles. We typically use a near-infrared femtosecond oscillator at 80 MHz repetition rate for the excitation. The average excitation intensity is ~ 10 kW/cm^2 (i.e., peak intensity of ~ 1GW/cm^2), which is only 1% of the biological cell damage threshold. Under such excitation, the SHG average power from a single 100 nm diameter $BaTiO_3$ nanoparticle is ~ 0.5 fW (i.e., ~ 4000 photons/second), corresponding to the SHG cross-section of 2000 GM. The SHG signal is sufficient to be detected by detectors with gain, such as an EMCCD or a PMT.

The SHG signal was found to be polarization dependent due to the tensor nature of the second-order nonlinearity. We observed a good agreement between the theory and the experimental results. Through a polar measurement, we can determine the orientation of the nanoparticle in the far field. With the knowledge of the polarization-dependent SHG signal, we studied the SHG response under linearly and circularly polarized excitation. We found that circularly polarized excitation is usually inferior

in terms of reducing the polarization dependency of the SHG signal. Interestingly, we also found that one could greatly reduce the polar response by using a rotating linearly polarized excitation at a rotation frequency much lower than optical frequency but higher than the integration time of the detection. Meanwhile, tightly focusing the excitation helps reduce the polarization dependency due to the depolarization of a tightly focused beam.

SHG nanoparticles have shown promise as long-term biological imaging probes due to their non-blinking and non-bleaching signal. These SHG nanoparticles can be readily imaged with a standard commercial two-photon confocal microscope. We used a near-infrared femtosecond laser for the excitation of the nanoparticles with excitation intensity tolerable for biological sample. The cytocompatibility of $BaTiO_3$ nanoparticles was verified with biological cells. No measurable toxicity was observed at the nanoparticle concentration of 30 μg/mL. For bio-imaging applications, we developed a biochemical scheme for covalently conjugating antibodies onto the surface of the nanoparticles. The antibody-nanoparticle conjugates were demonstrated for highly specific membrane protein labeling in living cells. Less than 5% nonspecific labeling was observed in a protein microarray.

Taking advantage of the coherent SHG signal, we have demonstrated novel imaging systems using SHG nanoparticles as nanoprobes. We build a H^2 microscope which captures the complex SHG field radiated from the nanoparticles in a digital hologram. As a result, the 3D SHG field, reflecting 3D distribution of the nanoparticles, can be reconstructed from the digital hologram. Sub-micron 3D spatial resolution has been achieved. We demonstrate imaging nanoparticles in biological

cells with the H^2 microscope. The H^2 microscopy shows its capability of fast 3D tracking of SHG nanoparticles, which offers opportunities for biological studies.

By further exploiting the coherence of the SHG radiation of the nanoparticles, we demonstrate light concentration on the nanoparticles behind a scattering medium via digital phase conjugation. This technique has the potential to improve the efficiency of photo-therapy as the biological tissue is generally scattering. Digital phase conjugation is a fast and efficient method to undo the scattering. The phase-conjugated field traces back the scattering trajectory and focuses on the nanoparticle. With a ground glass diffuser as the scattering medium, we have enhanced the light delivery onto the nanoparticle by 400 times. In addition to light concentration in scattering media, we build a phase conjugate scanning microscope which allows us to image the vicinity of the nanoparticle behind a scattering screen. The imaging is achieved by raster scanning the phase-conjugated focus in the area around the nanoparticle and the signal is detected pixel-by-pixel to form a scanning image. This great capability is based on the optical memory effect, which has the best performance when the scattering medium is thin and there is a non-diffusive space between the scattering medium and the imaging target. We used a phase conjugate scanning microscope to obtain a clear image of a target behind a ground glass diffuser by using SHG beacon nanoparticles.

The major challenge of using the SHG nanoparticles as nanoprobes is the relatively low SHG conversion efficiency. As we readily use 100 nm $BaTiO_3$ nanoparticles as imaging probes, smaller SHG nanoparticles are certainly attractive. In biological applications, the target proteins and molecules are usually smaller than 10 nm. Smaller nanoparticles are desirable for minimizing the perturbation of the system when introducing the imaging probes. It has been difficult to observe smaller

$BaTiO_3$ nanoparticles because the SHG power obeys the sixth-power dependency on the diameter of the nanoparticle. It is estimated that a 10 nm $BaTiO_3$ nanoparticle radiates ~ 10^{-3} photon/second under the same excitation intensity (~ 10 kW/cm^2 average intensity), which is extremely weak for detection. The excitation may be increased by an order of magnitude since it is only 1% of the cell damage threshold. This will lead to SHG signal of ~ 0.1 photon/second, which is still very weak. The low SHG conversion efficiency compared to fluorescence is the result of nonresonant SHG process. The nonresonant nature provides us a flexible choice in the excitation wavelength. In our laboratory, it has been demonstrated that the SHG efficiency can be enhanced 500 times by creating a plasmonic resonant nanoshell around the nanoparticle, and an enhancement of 3500 is theoretically possible [63]. Through engineering the plasmonic resonance of the nanoprobes, wavelength multiplexing can be achieved. One can also improve the conversion efficiency by using other materials which have stronger second-order nonlinearity. Recently, SHG from a CdTe/CdS core/shell quantum dot with a diameter of < 15 nm has been observed [47]. For biological applications, the cytocompatibility of these new nonlinear materials should be carefully examined.

To extend the usage of SHG nanoparticles as beacons of light to focus and image through biological tissue applications, the key is to perform the experiment from only one side of the scattering medium, since the other side will be inaccessible (as it is inside biological tissue). In the demonstrations we have shown in Chapter 5, we use the back side of the scattering medium for nanoparticle excitation and also signal detection. The detection from the back side is not essential and can be avoided by detecting reflection or epi-fluorescent signal. The challenge is to excite the nanoparticles through the scattering medium. The excitation intensity becomes much

lower due to the scattering and the SHG signal becomes weak and difficult to detect. In addition to improving the SHG efficiency of the nanoprobes, it is possible to combine the technology of adaptive optics and wavefront optimization for better excitation of the nanoprobes inside a scattering medium [143].

Finally, thanks to the unique optical properties of the SHG nanoprobes, they have provided opportunities for many scientific studies, which are not available with other technologies. Besides the applications that have been shown in this thesis, SHG nanoprobes have been demonstrated as sub-wavelength tunable coherent photon sources [57] and also as nanoprobes for local pulse shape measurement [145, 151]. We believe SHG nanoprobes have great potential in imaging and they will keep opening new avenues for scientific studies.

Bibliography

[1] M. Chalfie, Y. Tu, G. Euskirchen, W. W. Ward, and D. C. Prasher, "Green fluorescent protein as a marker for gene-expression," Science **263**, 802-805 (1994).

[2] S. M. Nie, and R. N. Zare, "Optical detection of single molecules," Annual Review of Biophysics and Biomolecular Structure **26**, 567-596 (1997).

[3] B. N. G. Giepmans, S. R. Adams, M. H. Ellisman, and R. Y. Tsien, "Review - The fluorescent toolbox for assessing protein location and function," Science **312**, 217-224 (2006).

[4] B. A. Griffin, S. R. Adams, and R. Y. Tsien, "Specific covalent labeling of recombinant protein molecules inside live cells," Science **281**, 269-272 (1998).

[5] J. Sheen, S. B. Hwang, Y. Niwa, H. Kobayashi, and D. W. Galbraith, "Green-fluorescent protein as a new vital marker in plant-cells," Plant Journal **8**, 777-784 (1995).

[6] X. Michalet, F. F. Pinaud, L. A. Bentolila, J. M. Tsay, S. Doose, J. J. Li, G. Sundaresan, A. M. Wu, S. S. Gambhir, and S. Weiss, "Quantum dots for live cells, in vivo imaging, and diagnostics," Science **307**, 538-544 (2005).

[7] D. R. Larson, W. R. Zipfel, R. M. Williams, S. W. Clark, M. P. Bruchez, F. W. Wise, and W. W. Webb, "Water-soluble quantum dots for multiphoton fluorescence imaging in vivo," Science **300**, 1434-1436 (2003).

[8] R. E. Campbell, O. Tour, A. E. Palmer, P. A. Steinbach, G. S. Baird, D. A. Zacharias, and R. Y. Tsien, "A monomeric red fluorescent protein," Proc. Natl. Acad. Sci. U. S. A. **99**, 7877-7882 (2002).

[9] M. Albota, D. Beljonne, J. L. Bredas, J. E. Ehrlich, J. Y. Fu, A. A. Heikal, S. E. Hess, T. Kogej, M. D. Levin, S. R. Marder, D. McCord-Maughon, J. W. Perry, H. Rockel, M. Rumi, C. Subramaniam, W. W. Webb, X. L. Wu, and C. Xu, "Design of organic molecules with large two-photon absorption cross sections," Science **281**, 1653-1656 (1998).

[10] C. Xu, and W. W. Webb, "Measurement of two-photon excitation cross sections of molecular fluorophores with data from 690 to 1050 nm," J. Opt. Soc. Am. B-Opt. Phys. **13**, 481-491 (1996).

[11] W. L. Rumsey, J. M. Vanderkooi, and D. F. Wilson, "Imaging of phosphorescence - a novel method for measuring oxygen distribution in perfused tissue," Science **241**, 1649-1651 (1988).

[12] S. A. Vinogradov, L. W. Lo, W. T. Jenkins, S. M. Evans, C. Koch, and D. F. Wilson, "Noninvasive imaging of the distribution in oxygen in tissue in vivo using near-infrared phosphors," Biophys. J. **70**, 1609-1617 (1996).

[13] S. Sivakumar, P. R. Diamente, and F. C. van Veggel, "Silica-coated Ln(3+)-doped LaF3 nanoparticles as robust down- and upconverting biolabels," Chem.-Eur. J. **12**, 5878-5884 (2006).

[14] D. K. Chatteriee, A. J. Rufalhah, and Y. Zhang, "Upconversion fluorescence imaging of cells and small animals using lanthanide doped nanocrystals," Biomaterials **29**, 937-943 (2008).

[15] L. L. Song, E. J. Hennink, I. T. Young, and H. J. Tanke, "Photobleaching kinetics of fluorescein in quantitative fluorescence microscopy," Biophys. J. **68**, 2588-2600 (1995).

[16] C. Eggeling, J. Widengren, R. Rigler, and C. A. M. Seidel, "Photobleaching of fluorescent dyes under conditions used for single-molecule detection: Evidence of two-step photolysis," Anal. Chem. **70**, 2651-2659 (1998).

[17] R. M. Dickson, A. B. Cubitt, R. Y. Tsien, and W. E. Moerner, "On/off blinking and switching behaviour of single molecules of green fluorescent protein," Nature **388**, 355-358 (1997).

[18] K. T. Shimizu, R. G. Neuhauser, C. A. Leatherdale, S. A. Empedocles, W. K. Woo, and M. G. Bawendi, "Blinking statistics in single semiconductor nanocrystal quantum dots," Phys. Rev. B **63**, 5 (2001).

[19] B. Mahler, P. Spinicelli, S. Buil, X. Quelin, J. P. Hermier, and B. Dubertret, "Towards non-blinking colloidal quantum dots," Nature Materials **7**, 659-664 (2008).

[20] X. Y. Wang, X. F. Ren, K. Kahen, M. A. Hahn, M. Rajeswaran, S. Maccagnano-Zacher, J. Silcox, G. E. Cragg, A. L. Efros, and T. D. Krauss, "Non-blinking semiconductor nanocrystals," Nature **459**, 686-689 (2009).

[21] C. C. Fu, H. Y. Lee, K. Chen, T. S. Lim, H. Y. Wu, P. K. Lin, P. K. Wei, P. H. Tsao, H. C. Chang, and W. Fann, "Characterization and application of single fluorescent nanodiamonds as cellular biomarkers," Proc. Natl. Acad. Sci. U. S. A. **104**, 727-732 (2007).

[22] Y. R. Chang, H. Y. Lee, K. Chen, C. C. Chang, D. S. Tsai, C. C. Fu, T. S. Lim, Y. K. Tzeng, C. Y. Fang, C. C. Han, H. C. Chang, and W. Fann, "Mass production and dynamic imaging of fluorescent nanodiamonds," Nat. Nanotechnol. **3**, 284-288 (2008).

[23] R. W. Boyd, *Nonlinear optics* (Academic, New York, 1992), pp. 41-52.

[24] J. N. Gannaway, and C. J. R. Sheppard, "2nd-harmonic imaging in scanning optical microscope," Optical and Quantum Electronics **10**, 435-439 (1978).

[25] R. Hellwart, and P. Christen, "Nonlinear optical microscopic examination of structure in polycrystalline ZnSe," Optics Communications **12**, 318-322 (1974).

[26] W. R. Zipfel, R. M. Williams, R. Christie, A. Y. Nikitin, B. T. Hyman, and W. W. Webb, "Live tissue intrinsic emission microscopy using multiphoton-excited native fluorescence and second harmonic generation," Proc. Natl. Acad. Sci. U. S. A. **100**, 7075-7080 (2003).

[27] A. Zoumi, A. Yeh, and B. J. Tromberg, "Imaging cells and extracellular matrix in vivo by using second-harmonic generation and two-photon excited fluorescence," Proc. Natl. Acad. Sci. U. S. A. **99**, 11014-11019 (2002).

[28] F. Helmchen, and W. Denk, "Deep tissue two-photon microscopy," Nature Methods **2**, 932-940 (2005).

[29] P. T. C. So, C. Y. Dong, B. R. Masters, and K. M. Berland, "Two-photon excitation fluorescence microscopy," Annual Review of Biomedical Engineering **2**, 399-429 (2000).

[30] P. J. Campagnola, A. C. Millard, M. Terasaki, P. E. Hoppe, C. J. Malone, and W. A. Mohler, "Three-dimensional high-resolution second-harmonic generation imaging of endogenous structural proteins in biological tissues," Biophys. J. **82**, 493-508 (2002).

[31] P. J. Campagnola, and L. M. Loew, "Second-harmonic imaging microscopy for visualizing biomolecular arrays in cells, tissues and organisms," Nature Biotechnology **21**, 1356-1360 (2003).

[32] R. M. Williams, W. R. Zipfel, and W. W. Webb, "Interpreting second-harmonic generation images of collagen I fibrils," Biophys. J. **88**, 1377-1386 (2005).

[33] S. V. Plotnikov, A. C. Millard, P. J. Campagnola, and W. A. Mohler, "Characterization of the myosin-based source for second-harmonic generation from muscle sarcomeres," Biophys. J. **90**, 693-703 (2006).

[34] P. Stoller, K. M. Reiser, P. M. Celliers, and A. M. Rubenchik, "Polarization-modulated second harmonic generation in collagen," Biophys. J. **82**, 3330-3342 (2002).

[35] S. W. Chu, S. Y. Chen, G. W. Chern, T. H. Tsai, Y. C. Chen, B. L. Lin, and C. K. Sun, "Studies of x((2))/x((3)) tensors in submicron-scaled bio-tissues by polarization harmonics optical microscopy," Biophys. J. **86**, 3914-3922 (2004).

[36] D. S. Chemla, and J. Zyss, eds. *Nonlinear optical Properties of organic molecules and crystals* (Academic, New York, 1987).

[37] P. N. Prasad, and D. J. Williams, *Introduction to nonlinear optical effects in molecules and polymers* (Wiley, New York, 1991).

[38] V. Alain, S. Redoglia, M. Blanchard-Desce, S. Lebus, K. Lukaszuk, R. Wortmann, U. Gubler, C. Bosshard, and P. Gunter, "Elongated push-pull diphenylpolyenes for nonlinear optics: molecular engineering of quadratic and cubic optical nonlinearities via tuning of intramolecular charge transfer," Chem. Phys. **245**, 51-71 (1999).

[39] L. Moreaux, O. Sandre, and J. Mertz, "Membrane imaging by second-harmonic generation microscopy," J. Opt. Soc. Am. B-Opt. Phys. **17**, 1685-1694 (2000).

[40] O. Bouevitch, A. Lewis, I. Pinevsky, J. P. Wuskell, and L. M. Loew, "Probing membrane-potential with nonlinear optics," Biophys. J. **65**, 672-679 (1993).

[41] D. A. Dombeck, M. Blanchard-Desce, and W. W. Webb, "Optical recording of action potentials with second-harmonic generation microscopy," J. Neurosci. **24**, 999-1003 (2004).

[42] J. I. Dadap, J. Shan, K. B. Eisenthal, and T. F. Heinz, "Second-harmonic Rayleigh scattering from a sphere of centrosymmetric material," Phys. Rev. Lett. **83**, 4045-4048 (1999).

[43] J. I. Dadap, J. Shan, and T. F. Heinz, "Theory of optical second-harmonic generation from a sphere of centrosymmetric material: small-particle limit," J. Opt. Soc. Am. B-Opt. Phys. **21**, 1328-1347 (2004).

[44] J. Nappa, G. Revillod, I. Russier-Antoine, E. Benichou, C. Jonin, and P. F. Brevet, "Electric dipole origin of the second harmonic generation of small metallic particles," Phys. Rev. B **71**, 4 (2005).

[45] J. Butet, J. Duboisset, G. Bachelier, I. Russier-Antoine, E. Benichou, C. Jonin, and P. F. Brevet, "Optical Second Harmonic Generation of Single Metallic Nanoparticles Embedded in a Homogeneous Medium," Nano Lett. **10**, 1717-1721 (2010).

[46] M. Jacobsohn, and U. Banin, "Size dependence of second harmonic generation in CdSe nanocrystal quantum dots," Journal of Physical Chemistry B **104**, 1-5 (2000).

[47] M. Zielinski, D. Oron, D. Chauvat, and J. Zyss, "Second-Harmonic Generation from a Single Core/Shell Quantum Dot," Small **5**, 2835-2840 (2009).

[48] J. C. Johnson, H. Q. Yan, R. D. Schaller, P. B. Petersen, P. D. Yang, and R. J. Saykally, "Near-field imaging of nonlinear optical mixing in single zinc oxide nanowires," Nano Lett. **2**, 279-283 (2002).

[49] S. W. Chan, R. Barille, J. M. Nunzi, K. H. Tam, Y. H. Leung, W. K. Chan, and A. B. Djurisic, "Second harmonic generation in zinc oxide nanorods," Appl. Phys. B-Lasers Opt. **84**, 351-355 (2006).

[50] A. V. Kachynski, A. N. Kuzmin, M. Nyk, I. Roy, and P. N. Prasad, "Zinc oxide nanocrystals for nonresonant nonlinear optical microscopy in biology and medicine," Journal of Physical Chemistry C **112**, 10721-10724 (2008).

[51] T. R. Kuo, C. L. Wu, C. T. Hsu, W. Lo, S. J. Chiang, S. J. Lin, C. Y. Dong, and C. C. Chen, "Chemical enhancer induced changes in the mechanisms of transdermal delivery of zinc oxide nanoparticles," Biomaterials **30**, 3002-3008 (2009).

[52] L. Le Xuan, C. Zhou, A. Slablab, D. Chauvat, C. Tard, S. Perruchas, T. Gacoin, P. Villeval, and J. F. Roch, "Photostable second-harmonic generation from a single KTiOPO4 nanocrystal for nonlinear microscopy," Small **4**, 1332-1336 (2008).

[53] E. M. Rodriguez, A. Speghini, F. Piccinelli, L. Nodari, M. Bettinelli, D. Jaque, and J. G. Sole, "Multicolour second harmonic generation by strontium barium niobate nanoparticles," Journal of Physics D-Applied Physics **42**, 4 (2009).

[54] P. Wnuk, L. Le Xuan, A. Slablab, C. Tard, S. Perruchas, T. Gacoin, J. F. Roch, D. Chauvat, and C. Radzewicz, "Coherent nonlinear emission from a single KTP nanoparticle with broadband femtosecond pulses," Opt. Express **17**, 4652-4658 (2009).

[55] L. Bonacina, Y. Mugnier, F. Courvoisier, R. Le Dantec, J. Extermann, Y. Lambert, V. Boutou, C. Galez, and J. P. Wolf, "Polar Fe(IO3)(3) nanocrystals as local probes for nonlinear microscopy," Appl. Phys. B-Lasers Opt. **87**, 399-403 (2007).

[56] C. L. Hsieh, Y. Pu, R. Grange, and D. Psaltis, "Second harmonic generation from nanocrystals under linearly and circularly polarized excitations," Opt. Express **18**, 11917-11932 (2010).

[57] Y. Nakayama, P. J. Pauzauskie, A. Radenovic, R. M. Onorato, R. J. Saykally, J. Liphardt, and P. D. Yang, "Tunable nanowire nonlinear optical probe," Nature **447**, 1098-U1098 (2007).

[58] Y. Z. Shen, P. Markowicz, J. Winiarz, J. Swiatkiewicz, and P. N. Prasad, "Nanoscopic study of second-harmonic generation in organic crystals with collection-mode near-field scanning optical microscopy," Opt. Lett. **26**, 725-727 (2001).

[59] S. Brasselet, V. Le Floc'h, F. Treussart, J. F. Roch, J. Zyss, E. Botzung-Appert, and A. Ibanez, "In situ diagnostics of the crystalline nature of single organic nanocrystals by nonlinear microscopy," Phys. Rev. Lett. **92**, 4 (2004).

[60] E. Delahaye, N. Tancrez, T. Yi, I. Ledoux, J. Zyss, S. Brasselet, and R. Clement, "Second harmonic generation from individual hybrid MnPS3-based nanoparticles investigated by nonlinear microscopy," Chemical Physics Letters **429**, 533-537 (2006).

[61] C. L. Hsieh, R. Grange, Y. Pu, and D. Psaltis, "Three-dimensional harmonic holographic microcopy using nanoparticles as probes for cell imaging," Opt. Express **17**, 2880-2891 (2009).

[62] C. L. Hsieh, R. Grange, Y. Pu, and D. Psaltis, "Bioconjugation of barium titanate nanocrystals with immunoglobulin G antibody for second harmonic radiation imaging probes," Biomaterials **31**, 2272-2277 (2010).

[63] Y. Pu, R. Grange, C. L. Hsieh, and D. Psaltis, "Nonlinear optical properties of core-shell nanocavities for enhanced second-harmonic generation," Phys. Rev. Lett. **104**, 4 (2010).

[64] L. L. Xuan, S. Brasselet, F. Treussart, J. F. Roch, F. Marquier, D. Chauvat, S. Perruchas, C. Tard, and T. Gacoin, "Balanced homodyne detection of second-harmonic generation from isolated subwavelength emitters," Appl. Phys. Lett. **89**, 121118 (2006).

[65] J. Extermann, L. Bonacina, E. Cuna, C. Kasparian, Y. Mugnier, T. Feurer, and J. P. Wolf, "Nanodoublers as deep imaging markers for multi-photon microscopy," Opt. Express **17**, 15342-15349 (2009).

[66] P. Pantazis, J. Maloney, D. Wu, and S. E. Fraser, "Second harmonic generating (SHG) nanoprobes for in vivo imaging," Proc. Natl. Acad. Sci. U. S. A. **107**, 14535-14540 (2010).

[67] C. L. Hsieh, Y. Pu, R. Grange, and D. Psaltis, "Digital phase conjugation of second harmonic radiation emitted by nanoparticles in turbid media," Opt. Express **18**, 12283-12290 (2010).

[68] C. L. Hsieh, Y. Pu, R. Grange, G. Laporte, and D. Psaltis, "Imaging through turbid layers by scanning the phase conjugated second harmonic radiation from a nanoparticle," Opt. Express **18**, 20723-20731 (2010).

[69] Y. Pu, M. Centurion, and D. Psaltis, "Harmonic holography: a new holographic principle," Appl. Optics **47**, A103-A110 (2008).

[70] E. Shaffer, P. Marquet, and C. Depeursinge, "Real time, nanometric 3D-tracking of nanoparticles made possible by second harmonic generation digital holographic microscopy," Opt. Express **18**, 17392-17403 (2010).

[71] G. Schlegel, J. Bohnenberger, I. Potapova, and A. Mews, "Fluorescence decay time of single semiconductor nanocrystals," Phys. Rev. Lett. **88**, 4 (2002).

[72] M. Chattoraj, B. A. King, G. U. Bublitz, and S. G. Boxer, "Ultra-fast excited state dynamics in green fluorescent protein: Multiple states and proton transfer," Proc. Natl. Acad. Sci. U. S. A. **93**, 8362-8367 (1996).

[73] K. Clays, and A. Persoons, "Hyper-Rayleigh scattering in solution," Phys. Rev. Lett. **66**, 2980-2983 (1991).

[74] L. R. Dalton, A. W. Harper, R. Ghosn, W. H. Steier, M. Ziari, H. Fetterman, Y. Shi, R. V. Mustacich, A. K. Y. Jen, and K. J. Shea, "Synthesis and processing of improved organic 2nd-order nonlinear-optical materials for applications in photonics," Chem. Mat. **7**, 1060-1081 (1995).

[75] N. Sandeau, L. Le Xuan, D. Chauvat, C. Zhou, J. F. Roch, and S. Brasselet, "Defocused imaging of second harmonic generation from a single nanocrystal," Opt. Express **15**, 16051-16060 (2007).

[76] N. K. Balla, P. T. C. So, and C. J. R. Sheppard, "Second harmonic scattering from small particles using Discrete Dipole Approximation," Opt. Express **18**, 21603-21611 (2010).

[77] X. Zhuang, P. B. Miranda, D. Kim, and Y. R. Shen, "Mapping molecular orientation and conformation at interfaces by surface nonlinear optics," Phys. Rev. B **59**, 12632-12640 (1999).

[78] Y. R. Shen, "Surfaces probed by nonlinear optics," Surface Science **299**, 551-562 (1994).

[79] Y. R. Shen, "Surface-properties probed by 2nd-harmonic and sum-frequency generation," Nature **337**, 519-525 (1989).

[80] K. B. Eisenthal, "Liquid interfaces probed by second-harmonic and sum-frequency spectroscopy," Chemical Reviews **96**, 1343-1360 (1996).

[81] J. Butet, G. Bachelier, J. Duboisset, F. Bertorelle, I. Russier-Antoine, C. Jonin, E. Benichou, and P. F. Brevet, "Three-dimensional mapping of single gold nanoparticles embedded in a homogeneous transparent matrix using optical second-harmonic generation," Opt. Express **18**, 22314-22323 (2010).

[82] P. Kim, S. C. Jones, P. J. Hotchkiss, J. N. Haddock, B. Kippelen, S. R. Marder, and J. W. Perry, "Phosphonic acid-modiried barium titanate polymer nanocomposites with high permittivity and dielectric strength," Adv. Mater. **19**, 1001-1005 (2007).

[83] A. A. Heikal, S. T. Hess, and W. W. Webb, "Multiphoton molecular spectroscopy and excited-state dynamics of enhanced green fluorescent protein (EGFP): acid-base specificity," Chem. Phys. **274**, 37-55 (2001).

[84] M. A. Albota, C. Xu, and W. W. Webb, "Two-photon fluorescence excitation cross sections of biomolecular probes from 690 to 960 nm," Appl. Optics **37**, 7352-7356 (1998).

[85] C. F. Bohren, and D. R. Huffman, *Absorption and Scattering of Light by Small Particles* (Wiley, 1998).

[86] J. D. Jackson, in *Classical Electrodynamics* (Wiley, New York, 1998), p. 410.

[87] P. J. Campagnola, M. D. Wei, A. Lewis, and L. M. Loew, "High-resolution nonlinear optical imaging of live cells by second harmonic generation," Biophys. J. **77**, 3341-3349 (1999).

[88] B. Richards, and E. Wolf, "Electromagnetic diffraction in optical systems .2. Structure of the image field in an aplanatic system," Proceedings of the Royal Society of London Series A-Mathematical and Physical Sciences **253**, 358-379 (1959).

[89] A. A. Asatryan, C. J. R. Sheppard, and C. M. de Sterke, "Vector treatment of second-harmonic generation produced by tightly focused vignetted Gaussian beams," J. Opt. Soc. Am. B-Opt. Phys. **21**, 2206-2212 (2004).

[90] E. Y. S. Yew, and C. J. R. Sheppard, "Effects of axial field components on second harmonic generation microscopy," Opt. Express **14**, 1167-1174 (2006).

[91] S. J. Lin, C. Y. Hsiao, Y. Sun, W. Lo, W. C. Lin, G. J. Jan, S. H. Jee, and C. Y. Dong, "Monitoring the thermally induced structural transitions of collagen by use of second-harmonic generation microscopy," Opt. Lett. **30**, 622-624 (2005).

[92] M. Strupler, A. M. Pena, M. Hernest, P. L. Tharaux, J. L. Martin, E. Beaurepaire, and M. C. Schanne-Klein, "Second harmonic imaging and scoring of collagen in fibrotic tissues," Opt. Express **15**, 4054-4065 (2007).

[93] A. C. Kwan, D. A. Dombeck, and W. W. Webb, "Polarized microtubule arrays in apical dendrites and axons," Proc. Natl. Acad. Sci. U. S. A. **105**, 11370-11375 (2008).

[94] C. K. Chou, W. L. Chen, P. T. Fwu, S. J. Lin, H. S. Lee, and C. Y. Dong, "Polarization ellipticity compensation in polarization second-harmonic generation microscopy without specimen rotation," Journal of Biomedical Optics **13**, 7 (2008).

[95] P. Schon, F. Munhoz, A. Gasecka, S. Brustlein, and S. Brasselet, "Polarization distortion effects in polarimetric two-photon microscopy," Opt. Express **16**, 20891-20901 (2008).

[96] A. M. Derfus, W. C. W. Chan, and S. N. Bhatia, "Probing the cytotoxicity of semiconductor quantum dots," Nano Lett. **4**, 11-18 (2004).

[97] C. Kirchner, T. Liedl, S. Kudera, T. Pellegrino, A. M. Javier, H. E. Gaub, S. Stolzle, N. Fertig, and W. J. Parak, "Cytotoxicity of colloidal CdSe and CdSe/ZnS nanoparticles," Nano Lett. **5**, 331-338 (2005).

[98] G. Ciofani, S. Danti, S. Moscato, L. Albertazzi, D. D'Alessandro, D. Dinucci, F. Chiellini, M. Petrini, and A. Menciassi, "Preparation of stable dispersion of barium titanate nanoparticles: Potential applications in biomedicine," Colloids and Surfaces B-Biointerfaces **76**, 535-543 (2010).

[99] G. Ciofani, S. Danti, D. D'Alessandro, S. Moscato, M. Petrini, and A. Menciassi, "Barium titanate nanoparticles: highly cytocompatible dispersions in glycol-chitosan and doxorubicin complexes for cancer therapy," Nanoscale Research Letters **5**, 1093-1101 (2010).

[100] D. H. Yoon, B. I. Lee, P. Badheka, and X. Y. Wang, "Barium ion leaching from barium titanate powder in water," Journal of Materials Science-Materials in Electronics **14**, 165-169 (2003).

[101] R. Helmy, and A. Y. Fadeev, "Self-assembled monolayers supported on TiO2: Comparison of C18H37SiX3 (X = H, Cl, OCH3C18H37Si(CH3)2C1, and C18H37PO(OH)(2)," Langmuir **18**, 8924-8928 (2002).

[102] P. R. Moses, L. M. Wier, J. C. Lennox, H. O. Finklea, J. R. Lenhard, and R. W. Murray, "Chemically modified electrodes. 9. X-ray photoelectron-spectroscopy of alkylamine-silanes bound to metal-oxide electrodes," Anal. Chem. **50**, 576-585 (1978).

[103] S. Mornet, C. Elissalde, V. Hornebecq, O. Bidault, E. Duguet, A. Brisson, and M. Maglione, "Controlled growth of silica shell on Ba0.6Sr0.4TiO3 nanoparticles used as precursors of ferroelectric composites," Chem. Mat. **17**, 4530-4536 (2005).

[104] B. Page, M. Page, and C. Noel, "A new fluorometric assay for cytotoxicity measurements in-vitro," International Journal of Oncology **3**, 473-476 (1993).

[105] J. O'Brien, I. Wilson, T. Orton, and F. Pognan, "Investigation of the Alamar Blue (resazurin) fluorescent dye for the assessment of mammalian cell cytotoxicity," European Journal of Biochemistry **267**, 5421-5426 (2000).

[106] Y. Xing, Q. Chaudry, C. Shen, K. Y. Kong, H. E. Zhau, L. Wchung, J. A. Petros, R. M. O'Regan, M. V. Yezhelyev, J. W. Simons, M. D. Wang, and S. Nie, "Bioconjugated quantum dots for multiplexed and quantitative immunohistochemistry," Nature Protocols **2**, 1152-1165 (2007).

[107] W. Jiang, B. Y. S. Kim, J. T. Rutka, and W. C. W. Chan, "Nanoparticle-mediated cellular response is size-dependent," Nat. Nanotechnol. **3**, 145-150 (2008).

[108] D. Gabor, G. W. Stroke, D. Brumm, A. Funkhous, and A. Labeyrie, "Reconstruction of phase objects by holography," Nature **208**, 1159 (1965).

[109] P. Gunter, "Holography, coherent-light amplification and optical-phase conjugation with photorefractive materials," Phys. Rep.-Rev. Sec. Phys. Lett. **93**, 199-299 (1982).

[110] J. W. Goodman, and R. W. Lawrence, "Digital image formation from electronically detected holograms," Appl. Phys. Lett. **11**, 77-79 (1967).

[111] U. Schnars, and W. Juptner, "Direct recording of holograms by a CCD target and numerical reconstruction," Appl. Optics **33**, 179-181 (1994).
[112] T. Zhang, and I. Yamaguchi, "Three-dimensional microscopy with phase-shifting digital holography," Opt. Lett. **23**, 1221-1223 (1998).
[113] E. Cuche, F. Bevilacqua, and C. Depeursinge, "Digital holography for quantitative phase-contrast imaging," Opt. Lett. **24**, 291-293 (1999).
[114] Q. Xu, K. B. Shi, H. F. Li, K. Choi, R. Horisaki, D. Brady, D. Psaltis, and Z. W. Liu, "Inline holographic coherent anti-Stokes Raman microscopy," Opt. Express **18**, 8213-8219 (2010).
[115] K. B. Shi, H. F. Li, Q. Xu, D. Psaltis, and Z. W. Liu, "Coherent anti-Stokes Raman holography for chemically selective single-shot nonscanning 3D Imaging," Phys. Rev. Lett. **104**, 4 (2010).
[116] E. Shaffer, N. Pavillon, J. Kuhn, and C. Depeursinge, "Digital holographic microscopy investigation of second harmonic generated at a glass/air interface," Opt. Lett. **34**, 2450-2452 (2009).
[117] O. Masihzadeh, P. Schlup, and R. A. Bartels, "Label-free second harmonic generation holographic microscopy of biological specimens," Opt. Express **18**, 9840-9851 (2010).
[118] Y. Pu, C. L. Hsieh, R. Grange, and D. Psaltis, *Harmonic Holography* in *Advances in Imaging and Electron Physics, Vol 160* (Elsevier Academic Press Inc., San Diego, 2010), pp. 75-112.
[119] K. Konig, P. T. C. So, W. W. Mantulin, and E. Gratton, "Cellular response to near-infrared femtosecond laser pulses in two-photon microscopes," Opt. Lett. **22**, 135-136 (1997).
[120] Y. Pu, and H. Meng, "Intrinsic speckle noise in off-axis particle holography," J. Opt. Soc. Am. A-Opt. Image Sci. Vis. **21**, 1221-1230 (2004).
[121] M. Centurion, Y. Pu, and D. Psaltis, "Holographic capture of femtosecond pulse propagation," J. Appl. Phys. **100**, 9 (2006).
[122] I. M. Vellekoop, and A. P. Mosk, "Focusing coherent light through opaque strongly scattering media," Opt. Lett. **32**, 2309-2311 (2007).
[123] I. M. Vellekoop, and A. P. Mosk, "Universal optimal transmission of light through disordered materials," Phys. Rev. Lett. **101**, 4 (2008).
[124] N. Ji, D. E. Milkie, and E. Betzig, "Adaptive optics via pupil segmentation for high-resolution imaging in biological tissues," Nature Methods **7**, 141-U184 (2010).
[125] I. M. Vellekoop, A. Lagendijk, and A. P. Mosk, "Exploiting disorder for perfect focusing," Nat. Photonics **4**, 320-322 (2010).
[126] T. Cizmar, M. Mazilu, and K. Dholakia, "In situ wavefront correction and its application to micromanipulation," Nat. Photonics **4**, 388-394 (2010).
[127] S. M. Popoff, G. Lerosey, R. Carminati, M. Fink, A. C. Boccara, and S. Gigan, "Measuring the transmission matrix in optics: an approach to the study and control of light propagation in disordered media," Phys. Rev. Lett. **104**, 4 (2010).
[128] S. Popoff, G. Lerosey, M. Fink, A. C. Boccara, and S. Gigan, "Image transmission through an opaque material," Nat. Commun. **1**, 5 (2010).
[129] M. Cui, "A high speed wavefront determination method based on spatial frequency modulations for focusing light through random scattering media," Opt. Express **19**, 2989-2995 (2011).

[130] M. Cui, "Parallel wavefront optimization method for focusing light through random scattering media," Opt. Lett. **36**, 870-872 (2011).
[131] E. N. Leith, and J. Upatniek, "Reconstructed wavefronts and communication theory," Journal of the Optical Society of America **52**, 1123-1128 (1962).
[132] E. N. Leith, and J. Upatniek, "Holographic imagery through diffusive media," Journal of the Optical Society of America **56**, 523 (1966).
[133] J. W. Goodman, W. H. Huntley, D. W. Jackson, and M. Lehmann, "Wavefront-reconstruction imaging through random media," Appl. Phys. Lett. **8**, 311-313 (1966).
[134] H. Kogelnik, "Holographic image projection through inhomogeneous media," Bell System Technical Journal **44**, 2451-2455 (1965).
[135] E. Leith, C. Chen, H. Chen, Y. Chen, D. Dilworth, J. Lopez, J. Rudd, P. C. Sun, J. Valdmanis, and G. Vossler, "Imaging through scattering media with holography," J. Opt. Soc. Am. A-Opt. Image Sci. Vis. **9**, 1148-1153 (1992).
[136] Z. Yaqoob, D. Psaltis, M. S. Feld, and C. Yang, "Optical phase conjugation for turbidity suppression in biological samples," Nat. Photonics **2**, 110-115 (2008).
[137] M. Cui, E. J. McDowell, and C. H. Yang, "An in vivo study of turbidity suppression by optical phase conjugation (TSOPC) on rabbit ear," Opt. Express **18**, 25-30 (2010).
[138] M. Cui, and C. H. Yang, "Implementation of a digital optical phase conjugation system and its application to study the robustness of turbidity suppression by phase conjugation," Opt. Express **18**, 3444-3455 (2010).
[139] X. A. Xu, H. L. Liu, and L. V. Wang, "Time-reversed ultrasonically encoded optical focusing into scattering media," Nat. Photonics **5**, 154-157 (2011).
[140] A. Yariv, D. Fekete, and D. M. Pepper, "Compensation for channel dispersion by non-linear optical phase conjugation," Opt. Lett. **4**, 52-54 (1979).
[141] D. M. Pepper, and A. Yariv, "Compensation for phase distortions in non-linear media by phase conjugation," Opt. Lett. **5**, 59-60 (1980).
[142] M. Paurisse, M. Hanna, F. Druon, P. Georges, C. Bellanger, A. Brignon, and J. P. Huignard, "Phase and amplitude control of a multimode LMA fiber beam by use of digital holography," Opt. Express **17**, 13000-13008 (2009).
[143] I. M. Vellekoop, E. G. van Putten, A. Lagendijk, and A. P. Mosk, "Demixing light paths inside disordered metamaterials," Opt. Express **16**, 67-80 (2008).
[144] S. L. Jacques, "Time-resolved reflectance spectroscopy in turbid tissues," IEEE Transactions on Biomedical Engineering **36**, 1155-1161 (1989).
[145] J. Extermann, L. Bonacina, F. Courvoisier, D. Kiselev, Y. Mugnier, R. Le Dantec, C. Galez, and J. P. Wolf, "Nano-FROG: Frequency resolved optical gating by a nanometric object," Opt. Express **16**, 10405-10411 (2008).
[146] J. W. Goodman, *Speckle phenomena in optics* (Roberts & Company 2006).
[147] I. M. Vellekoop, and C. M. Aegerter, "Scattered light fluorescence microscopy: imaging through turbid layers," Opt. Lett. **35**, 1245-1247 (2010).
[148] I. Freund, M. Rosenbluh, and S. Feng, "Memory effects in propagation of optical waves through disordered media," Phys. Rev. Lett. **61**, 2328-2331 (1988).
[149] P. R. Seem, J. D. R. Buchanan, and R. P. Cowburn, "Impact of surface roughness on laser surface authentication signatures under linear and rotational displacements," Opt. Lett. **34**, 3175-3177 (2009).

[150] S. C. Feng, C. Kane, P. A. Lee, and A. D. Stone, "Correlations and fluctuations of coherent wave transmission through disordered media," Phys. Rev. Lett. **61**, 834-837 (1988).

[151] H. F. Li, Z. Zhang, Q. A. Xu, K. B. Shi, Y. S. Jia, B. G. Zhang, Y. Xu, and Z. W. Liu, "Characterizing ultrashort optical pulses using second-order nonlinear nanoprobes," Appl. Phys. Lett. **97**, 261108 (2010).